EVOLUTION AND PERSISTENCE OF CIRCULAR AND LINEAR POLARIZATION IN SCATTERING ENVIRONMENTS

by

John David van der Laan

A Dissertation Submitted to the Faculty of the

COLLEGE OF OPTICAL SCIENCES

In Partial Fulfillment of the Requirements
For the Degree of

DOCTOR OF PHILOSOPHY

In the Graduate College

THE UNIVERSITY OF ARIZONA

2015

THE UNIVERSITY OF ARIZONA
GRADUATE COLLEGE

As members of the Dissertation Committee, we certify that we have read the dissertation prepared by John David van der Laan
entitled EVOLUTION AND PERSISTENCE OF CIRCULAR AND LINEAR POLARIZATION IN SCATTERING ENVIRONMENTS
and recommend that it be accepted as fulfilling the dissertation requirement for the Degree of Doctor of Philosophy.

Eustace L. Dereniak — Date: 17 July 2015

James T. Schwiegerling — Date: 17 July 2015

Shanalyn A. Kemme — Date: 17 July 2015

Date: 17 July 2015

Date: 17 July 2015

Final approval and acceptance of this dissertation is contingent upon the candidate's submission of the final copies of the dissertation to the Graduate College.
I hereby certify that I have read this dissertation prepared under my direction and recommend that it be accepted as fulfilling the dissertation requirement.

Dissertation Director: Eustace L. Dereniak — Date: 17 July 2015

STATEMENT BY AUTHOR

This dissertation has been submitted in partial fulfillment of requirements for an advanced degree at the University of Arizona and is deposited in the University Library to be made available to borrowers under rules of the Library.

SIGNED: John David van der Laan

ACKNOWLEDGEMENTS

This dissertation represents the culmination of a long educational journey. This work and what it represents would not have been possible without the help and support of many people that are very deserving of thanks.

First, I'd like to thank my advisor at the University of Arizona, Dr. Eustace Dereniak. I am very thankful to have had the opportunity to work with Dr. Dereniak. I am grateful to Dr. Dereniak for trusting me with this project and for connecting me with great mentors and optical science industry leaders I have encountered on this journey. This work would not have been possible without Dr. Dereniak's support.

I'd like to thank my mentor, Dr. Shanalyn Kemme, for her support and the opportunity to work with her at Sandia National Laboratories [1]. Her comments and collaboration have been invaluable to the creation and completion of this dissertation. This work's impact was greatly increased by her insistence on quality research and her ability to push me to do my best work.

I'd like to thank my collaborators at Sandia National Laboratories. Many thanks to Dr. David Scrymgeour for hours of phone meetings and other valuable conversations, and for running simulations in Albuquerque while I was in Tucson. This work would not have been completed without his help and I am grateful. I'd also like to thank Tony Carter for his help and guidance in setting up and automating experiments. Lastly, thanks are due to Dr. Jeremy Wright. This work was significantly impacted by his contributions, illuminating conversations, and support.

Thanks are also due to Elizabeth Quinley. She spent many hours reading and reviewing this dissertation, and for that I am very thankful. I am also thankful for her support along the long and often bumpy road.

I'd like to also thank Dr. Christopher Middlebrook at Michigan Technological University. My interest and pursuit of an optical science degree was directly related to his encouragement and teaching.

Finally, I'd like to thank my family: my father Mark, mother Denise, and brother Lucas. Without their support and love this work would not be possible. They all taught me to strive for excellence and to work hard to achieve my goals. My parents inspired me to pursue higher education and instilled in me the joy of learning from an early age. I love my family and am so thankful for their steadfast support.

[1] Sandia National Laboratories is a multi-program laboratory managed and operated by Sandia Corporation, a wholly owned subsidiary of Lockheed Martin Corporation, for the U.S. Department of Energy's National Nuclear Security Administration under contract DE-AC04-94AL85000.

DEDICATION

To my parents,

Mark and Denise,

for their unconditional love, support, and encouragement.

TABLE OF CONTENTS

TABLE OF CONTENTS – *Continued*

TABLE OF CONTENTS – *Continued*

LIST OF FIGURES

LIST OF FIGURES – *Continued*

LIST OF FIGURES – *Continued*

LIST OF TABLES

ABSTRACT

Sensing in scattering environments, such as fog and dust, poses a serious challenge for all optical systems and is important for many critical surveillance applications. The use of polarized light, specifically circularly polarized light, has shown great promise for improving detection range and sensing in highly scattering, real-world environments. While the potential impact to application is significant, the optical science and sensing community lacks data on broad wavelength and environmental parameters where circularly polarized light outperforms linearly polarized light, increasing detection range and signal persistence. In this dissertation I quantify, through simulation and experimental results, the advantage of circularly polarized light in laboratory and real-world scattering environments – focusing on circularly polarized light's superior persistence in these environments. I present new and unique contributions to the study of polarized light in both isotropic (Rayleigh regime) and forward-scattering environments, showing circular polarization's superior persistence increases detection range for real-world environments over broad wavelength and particle size regimes.

Utilizing polarization-tracking Monte Carlo simulations for varying particle size, wavelength, and refractive index, I quantify when circular polarization outperforms linear polarization in maintaining the illuminating polarization state for large optical thicknesses, persisting to longer ranges. I identify many real-world environments with particle sizes of radiation fog, advection fog, and Sahara dust where circular polarization outperforms linear polarization over broad wavelength ranges in the infrared spectrum. This enhancement with circular polarization can be exploited to improve sensing range and target detection in obscurant environments that are important in many critical surveillance applications. Conversely, I also identify a few environmental configurations where linear polarization outperforms circular polarization. However, circular polarization's response is generally larger and over broader wavelength ranges in the infrared regime for real-world scattering environments.

Experiments were conducted for both 1) isotopically-scattering (Rayleigh regime) environments and 2) forward-scattering environments using polystyrene microspheres with well-defined diameters. These measurements demonstrated that in the forward-scattering environments, circular polarization persists through increasing optical thickness better than linear polarization. Variations in persistence were investigated as a function of collection geometry, angular field of view, and collection area. Persistence for both linear and circular polarization was found to be

more susceptible to collection geometry, specifically increased collection area, in the isotropically-scattering (Rayleigh regime) environment. Similarly, linear polarization in the forward-scattering environments is dependent upon changes in collection geometry. Significantly, circular polarization's response is nearly unaffected by variations of both field of view and collection area for the forward-scattering environments. Circular polarization proves to be not only generally better in persistence but also more tolerant of variations in angular collection and collection area compared to linear polarization, making it ideal and flexible for use in optical sensing systems in scattering environments.

Finally, I present simulation results that show the evolution of linear and circularly polarized light as it scatters throughout both isotropic (Rayleigh regime) and forward-scattering environments as a function of scattering event. Circularly polarized light persists through a larger number of scattering events longer than linearly polarized light for all forward-scattering environments; but not for scattering in the Rayleigh regime. Circular polarization's increased persistence occurs for both forward and backscattered light. The evolution of the polarization states as they propagate through the various environments are illustrated on the Poincaré sphere after successive scattering events. This work displays individual scattering events as well as a cumulative, measurable result, in an intuitive manner.

Throughout this dissertation I quantify the polarization persistence and memory of circularly polarized light in real-world scattering environments over broad wavelength, particle size, and collection-geometry parameter spaces; and for the first time, detail the evolution and modification of both circularly and linearly polarized states through isotropic and forward-scattering environments. These results show how circular polarization can extend range and sensing capability in surveillance sensing applications in real-world scattering environments.

CHAPTER 1

Introduction and Historical Background

1.1 Introduction

This dissertation presents simulation and experimental results quantifying the use of circularly polarized light in various laboratory and real-world scattering environments; focusing on where circularly polarized light can increase sensing range and possibly imaging in scattering environments. Light-scattering particles in fog, clouds, or dust change the direction of the ambient or active illuminating radiation, reducing the radiation that reaches and ultimately returns from a target of interest. This results in decreased signal from the target and ultimately a decrease in the ability to distinguish a target from the background. In order to mitigate the effects of scattering, all sensing parameters must be leveraged, including active illuminating wavelength and polarization state.

The objective of this research is to explore the effects of active illuminating circular polarization over a broad band of environmental parameters and wavelengths. As will be detailed in the following sections, most of the publications in this area are focused on discrete particle sizes, singular illuminating wavelengths, and limited scattering environment models. This could be due to experimental constraints or the limited cases where circular polarization is useful. To date, no research has simulated or experimentally shown circular polarization's persistence, or mem-

ory, benefits over broad environmental parameter spaces and wavelength ranges, or shown the evolution of circular and linear polarization states in these environments. Through the use of polarization tracking Monte Carlo simulations and lab based measurements, I quantify circular polarization's increased polarization persistence in scattering environments of polystyrene microspheres in water, radiation fog, advection fog, various laboratory-generated fogs, and small and large-sized Sahara dust. Analysis compares and distinguishes the utility of active linear and active circular polarization's performance across these broad scattering environments. For most modern sensing applications it is impractical to use unpolarized light in an active illumination configuration as unpolarized illumination offers no additional degree of freedom to a sensing system. As a result, the focus throughout this dissertation is on the difference between the scattering of incident linearly and circularly polarized light.

This dissertation is organized as follows: Chapter 1, provides a history of the interest in circular polarization in scattering environments and the investigation of polarized light in scattering environments. This chapter reviews the majority of relevant published work and is divided into sections based on the scattering environments of interest. Chapter 2 provides detailed background information on polarization, polarimetry, scattering theory, and the polarization-tracking Monte Carlo program. The chapter describes the mathematical basis of Mie scattering theory and how it is utilized in the Monte Carlo program to model polarized light interaction with scattering particles. My original research is presented in Chapters 3 through 5. Chapter 3 provides reflection and transmission polarization-tracking

Monte Carlo results comparing linear and circular polarization's persistence in simulated scattering environments of radiation fog, advection fog, small particle Sahara dust, and large particle Sahara dust. Chapter 4 provides experimental and simulation results for a set of underwater scattering environments utilizing polystyrene microspheres as scattering objects. This chapter provides analysis of simulation results compared to physical experiments. Specifically, this chapter presents persistence sensitivity differences for circular and linear polarizations from collection geometry variations. Chapter 5 provides simulation results that show the evolution of linearly and circularly polarized light as it scatters throughout both isotropic (Rayleigh regime) and forward-scattering environments. Lastly, Chapter 6 provides closing remarks and a summary of the work presented in this dissertation as well as introduces proposed follow-on work related to this research. Additionally, there are two appendices which contain the Monte Carlo code used for this work (Appendix A) and polarization persistence measurement results that were performed in a fog chamber at Sandia National Laboratories (Appendix B).

Significant original contributions encompassed in this dissertation are as follows:

- J. D. van der Laan, D. A. Scrymgeour, S. A. Kemme, and E. L. Dereniak, "Range and contrast imaging improvements using circularly polarized light in scattering environments," Proc. SPIE **8706**, 87060R (2013).

- J. D. van der Laan, D. A. Scrymgeour, S. A. Kemme, and E. L. Dereniak, "Increasing detection range and minimizing polarization mixing with circularly polarized light through scattering environments," Proc. SPIE **9099**, 909908 (2014).

- J. D. van der Laan, D. A. Scrymgeour, J. B. Wright, S. A. Kemme, and E. L. Dereniak, "Increasing persistence through scattering environments by using circularly polarized light," Proc. SPIE **9465**, 94650U (2015).
- J. D. van der Laan, D. A. Scrymgeour, S. A. Kemme, and E. L. Dereniak, "Detection range enhancement using circularly polarized light in scattering environments for infrared wavelengths," Appl. Opt. **54**, 2266–74 (2015).
- J. D. van der Laan, J. B. Wright, D. A. Scrymgeour, S. A. Kemme, and E. L. Dereniak, "Evolution of circular and linear polarization in scattering environments," Opt. Express, (In Review).

1.2 Circular Polarization: Motivated by Nature

Nature often surprises scientists with its elegant and unexpected intricacies. Through the ages, people have used their five senses to observe and understand the universe around them. As humans we are often limited by the scope of our senses. Our sense of sight is especially constrained within the broad spectrum of radiation. We are limited to observing a small range of wavelengths, which we identify as colors. We are also limited in the intensities of light, which we identify as brightness, that we can observe. These limitations hindered the observation and therefore discover of one of the fundamental properties of light, that of polarization. It took an inquisitive scientist, Erasmus Bartholin, peering through a piece of Icelandic Spar, a calcite crystal, in 1669 to first write down and observe the effects of polarization [1]. It wasn't until almost two hundred years later that this fundamental property of light was fully understood physically and mathematically [2]. Yet

Figure 1.1: The Mantis Shrimp [3].

fast forward an additional hundred years to the present day and scientists continue to discover and expand our knowledge of the properties and uses of polarized light.

While the human sense of sight is limited to visible wavelengths and is unable to observe polarized light, nature continues to inspire. Of recent surprise to scientists was the discovery of the most diverse optical system found in nature to date. The animal that possesses this amazing optical system is the Mantis Shrimp, a creature of 6 – 12 inches in length which dwells in shallow coastal ocean waters and is shown in Figure 1.1.

The foremost distinguishing feature of the Mantis Shrimp is its sixteen types of photoreceptors [4–8]. Thanks to these photoreceptors, which receive and process light, the shrimp can see wavelengths from the ultra-violet (UV) through the infrared (IR). Humans have merely three photoreceptors and can see only visible wavelengths. The mantis shrimp not only is able to see more wavelengths than humans but can also see polarized light. This fact is not unique to the mantis shrimp. Many types of insects (honey bees, ants, butterflies), as well as some fish have been shown to sense

Figure 1.2: Close up of the Mantis Shrimp's eyes. The eyes are separated into segments which are sensitive to different polarization states and wavelength bands [14, 15].

linearly polarized light and use it for navigation and predatory advantage [9–11]. What places the Mantis shrimp's optical systems above others is its unique ability to sense circularly polarized light [12, 13]. The Mantis shrimp is the only animal in nature currently discovered and experimentally shown to possess an optical system that is capable of observing the complete Stokes parameters. Figure 1.2 shows a close up view of the Mantis shrimps complex eyes.

Since the discovery of circular polarized sensing in the Mantis shrimp in 2008 there has been an increased interest and multiple hypotheses as to why it would evolve to possess circular polarization vision. Pertinent for this dissertation is the hypothesis that circular polarization increases the range of detection of prey as well as the range of optical communication between mantis shrimp in murky and turbid coastal waters. Mantis shrimp live on the bottom of the ocean where sand and other particles are roiled, creating a highly scattering and turbid environment. Evolving an optical system, capable of detecting friend or foe from a larger standoff

range, would be advantageous. This raises interesting questions about the physics of circularly polarized light interactions within scattering environments and is the motivation behind this work.

1.3 Polarization Scattering

The use of polarization in scattering environments is a popular topic in recent scientific literature. Polarization offers an added variable to a sensing system that can be manipulated to better discriminate a target from a scene and sense to greater depths in scattering environments. Previous research often has developed simulations and experiments for underwater scenes. Generally, the research utilizes polystyrene microspheres, milk, or tissue phantoms in water as scattering particles. Many of these underwater environments have similar scattering properties as biological tissue matrixes; therefore, these scattering environments have been of particular interest to the medical research community. This introduction reviews relevant published research which utilizes polarization in scattering media and details how this dissertation differs from previous publications.

Some of the first experiments utilizing polarization to increase imaging range in a scattering environment date back to the 1960's. In 1966 Gilbert and Pernicka performed experiments in underwater scenes utilizing a circularly polarized incoherent source to decrease backscatter and increase contrast and range [16, 17]. The experiments used circularly polarized illumination and a detector with a circular analyzer. Contrast enhancements of up to a factor of 19.5 were observed for highly reflective targets. Gilbert followed this experiment with a set of contrast measurements in

underwater scenes with polystyrene microspheres as scattering particles with the same incoherent illumination [18]. Specifically, he measured contrast from circularly polarized illumination from a tungsten lamp and detection with monodisperse distributions of 0.125, 0.234, 0.357, 0.557, 0.796, and 1.099 microns and polydisperse distributions of 6 – 14, 25 – 55, and 50 – 100 microns. The circular polarization imaging technique increased contrast for the monodisperse distributions smaller than 0.8 microns but was not shown to be effective for the other sizes and distributions. Various groups have since performed similar experiments and simulations investigating transmission, backscatter, contrast, and range improvements in scattering environments of polystyrene microspheres in water.

1.3.1 **Polystyrene Microspheres in Water**

The most common scattering environment investigated in existing research literature is polystyrene microspheres in water. These spheres are readily available in monodisperse and polydisperse distributions with known refractive index ranging from 1.55 to 1.59 at visible wavelengths [19]. A review of existing research utilizing polystyrene microspheres in water as scattering media follows.

Bicout *et al.* showed through simulations and experiments that circular polarization persisted further than linear polarization for 0.48 and 1.05 micron diameter latex spheres in water at a wavelength of 670 nm [20]. Silverman *et al.* showed an increase in contrast by a factor of 2 – 3, using a 544 nm polarization-modulated laser while imaging targets through 1 micron latex spheres in water. They investigated both linear and circular polarization, showing better contrast with circular polariza-

tion [21]. Cameron *et al.* and Rakovic *et al.* presented simulation and experimental two-dimensional backscattered Mueller matrix results for 2.02 micron polystyrene microspheres in water at a wavelength of 632.8 nm [22, 23]. Lewis *et al.* published contrast advantages of a factor of 4 for circular polarization-difference imaging versus linear polarization, and a factor of 20 for circular polarization-difference imaging versus intensity imaging. They used 0.1 micron polystyrene spheres in water with a single active illumination wavelength of 632.8 nm [24]. Sankaran *et al.* experimentally looked at both circular and linear polarization persistence through six different sizes of polystyrene microspheres (0.107, 0.48, 0.99, 1.072, 2.092, and 9.14 microns) in water at varying concentrations, and a tissue phantom with polystyrene spheres ranging from 25 to 675 nm at a wavelength of 632.8 nm [25, 26]. Circular polarization was shown to be better than linear polarization for larger particle sizes, however this did not hold true at high concentrations of microspheres.

Through simulations and experiments Bartel *et al.* investigated the characteristics of 543 nm polarized light backscattered from solutions containing polystyrene microsphere with diameters of 204 nm and 2040 nm, specifically producing full backscattered Mueller matrices for the solutions [27]. Walker *et al.* and Turpin *et al.* showed contrast improvements through simulations of circular and linear cross-polarization difference imaging for size parameters (proportional to the ratio of the particle diameter and wavelength) of 0.01 and 3.0 of polystyrene microspheres in water [28, 29]. Ishimaru *et al.* produced polarization persistence results from simulations for both linear and circular polarization for a size distribution of latex particles ($\sim$ 2 microns) in water with a single illuminating wavelength of 530 nm

[30]. Circular polarization persisted longer than linear polarization at larger optical thicknesses. Similarly, Ketprom *et al.* performed experiments and simulations with the same scattering environment at a wavelength of 632.8 nm investigating the intensity at various scattering angles for co and cross-polarizations [31]. Their results showed the difference between co and cross-polarizations of circular polarization (right and left circular polarization) to be larger than that of linear polarization for simulations at all angles, experimental results were not conclusive. Kim and Moscoso investigated the temporal variations of backscattered 633 nm circularly polarized light from latex spheres with diameters of 0.152, 0.378, and 0.606 microns [32]. Their results showed that for the larger sized particles the backscattered flux maintains the original polarization state over time, exhibiting polarization memory. Kartazayeva *et al.* performed experiments similar to Lewis *et al.*, investigating imaging techniques utilizing circular and linear polarization through large-diameter (10.143 microns) and small-diameter (0.202 microns) polystyrene particles with an active illumination of 632.8 nm, showing increased contrast by a factor of 3 for circular polarization imaging versus linear polarization imaging [33]. Northdurft and Yao performed experiments to look at contrast improvements with linear and circular polarization. Active illumination with a wavelength of 633 nm was used to image targets immersed in solutions of polystyrene microspheres with diameters of 0.356 and 0.989 microns. Contrast measurements were compared for illumination polarizations and co, cross, unpolarized, and difference imaging techniques [34]. Circular cross polarized light provided the best contrast enhancement with reflective targets and smaller background scattering.

Cai *et al.* performed simulations and experiments of temporal variations of backscattered circularly polarized light with four sizes (0.1, 0.213, 0.855, and 8.0 microns) of polystyrene microspheres in water with a wavelength of 610 nm [35]. They showed backscattered light from circular polarized illumination is co-polarized (the same helicity) when the scattering particles are larger than the wavelength, and cross-polarized (opposite helicity) when the scattering particles are smaller than the wavelength. Finally, Shukla *et al.* investigated image contrast improvements using polarization-difference gating techniques with scattering environments of polydisperse polystyrene (mean diameter: 0.11 and 1.08 micron) and silica (mean diameters: 0.16 and 0.97 micron) spheres in water at a wavelength of 632.8 nm. Circular polarized imaging improved the resolution and contrast [36, 37]. The works mentioned represent much of the previously published work utilizing polystyrene microspheres in water as the scattering environment of interest. The existing research is often limited to specific wavelengths and particle sizes.

1.3.2 **Non-Polystyrene Particles in Water**

Similar to the polystyrene microsphere research, there are various groups who have investigated polarized light interaction and imaging through milky and Maalox filled water. Milk particles are generally considered spherical and range from 0.04 to 0.3 microns in diameter for casein molecules and 1 – 20 microns in diameter for fat globules [38]. Light scatters from the entire range of these particles. Maalox's particle distribution is similar to milk but does not contain the large fat globules and therefore consists of particles smaller than 5 microns [39]. Swartz showed an

enhancement in the signal-to-noise ratio for linear polarization discrimination imaging for a scattering environment of Maalox in water with 532 nm illumination [40]. Using linear polarization difference imaging, Rowe *et al.* and Tyo *et al.* showed increased contrast and an increase in imaging distance of 2 – 3 times that found with traditional imaging. They used an incoherent tungsten source and milky water as the scattering medium [41, 42]. Chenault and Pezzaniti showed imaging contrast in milky water solutions improved by a factor of four with the use of linear polarized light at a wavelength of 590 nm [43]. Recently, Dubreuil *et al.* investigated the resulting contrast improvement when using linear and circular polarization methods in varying concentrations of milky water solutions with polarization-maintaining and depolarizing objects; a 632.8 nm laser was used for illumination. The polarization-maintaining objects are highly reflective; scattering highly polarized light from their surface when incident light is highly polarized. Depolarizing objects used in their experiments scatter light in random directions leading to depolarized scattered light from its surface [38]. The research involving milky water and Maalox filled water scattering environments is closely related to the polystyrene microsphere scattering environment research but literature review has revealed to be more limited in number and wavelengths investigated.

1.3.3 **Biological Tissue and Tissue Phantoms**

Polarized light has been used in biological sciences for decades but has been of recent interest due to the possibility of increasing imaging depth into tissue, which acts as highly scattering media. A good review of tissue polarimetry's history and current

uses was written by Ghosh and Vitken [44]. A few representative examples of recent research in this field follows.

Demos and Alfano performed experiments utilizing polarization imaging techniques on human skin [45]. Specifically, they used linear polarization imaging techniques to image the surface and subsurface of the skin. For surface imaging, a linear polarization-difference technique with an illumination at 580 nm increased contrast by a factor of 4.5 compared to traditional intensity imaging. For subsurface imaging, they used a multispectral approach by subtracting orthogonal linearly polarized images with 570 and 600 nm illuminations. Demos *et al.* continued this type of research and performed subsurface spectral and linear polarization-difference imaging of an object embedded 1.5 cm within chicken tissue with illuminating wavelengths of 600, 690, 770, and 970 nm [46].

Sankaran *et al.* looked at both circularly and linearly polarized light's persistence through several biological porcine tissue samples (porcine fat, blood, tendon, heart, and artery tissue) at a wavelength of 632.8 nm. Circular polarization was shown to persist for some but not for all tissue samples and generally performed better on less dense tissues [25, 47]. Jacques *et al.* imaged human skin pathologies with higher contrast using a linear polarization-difference technique with incoherent illumination, enabling the identification of skin cancer for surgical excision [48]. Similarly, Ramella-Roman *et al.* built a handheld imager utilizing the same imaging technique and illumination for imaging melanoma and nevus in human tissue [49].

Shoa *et al.* investigated linear and circular degree of polarization imaging through a fat emulsion at 532 nm illumination, showing circular degree of polar-

ization imaging produced a factor of two increase in contrast versus linear degree of polarization imaging [50]. Nan *et al.* investigated linear polarization-difference imaging techniques with 650 nm illumination on duck heart tissue and human skin pathologies (herpes zoster and tinea pedis) [51]. Using these techniques they were able to better distinguish skin diseases and aid in diagnosis. Lastly, Da Silva *et al.* investigated three different imaging techniques with elliptically and linearly polarized illumination at 623.8 nm. They imaged objects in fat emulsions, chicken breast tissue, and in vivo rat brain tissue. The three techniques were used to image the surface (collinear - crosslinear polarizations), the middle (coelliptical - crosslinear polarization), and the multiply scattered (crosslinear) portions of the tissues. With these techniques they were able to better image the subsurface volumes by decreasing surface and deep volume scattering contaminants [52]. While imaging through biological tissue has proven to be more complicated than imaging through polystyrene microspheres, milk, and Maalox, polarization can improve contrast, resolution and range/depth for some biological scattering environments.

1.3.4 **Fog Environments**

When compared to the amount of published research regarding underwater scattering environments (polystyrene microspheres, milk, and Maalox in water) and biological tissue, there are few published simulations or experiments using polarized light interaction in real-world scattering environments such as fog and dust. Fog and dust are a major challenge to remote sensing. Available publications using real-world scattering environments is reviewed here. These publications provided

an important foundation for this dissertation but are still limited in wavelength, polarization, and environmental parameters.

Deirmendjian numerically calculated the intensity angular scattering phase functions for cloud (mean diameter = 5 microns, max diameter = 12 microns) and haze (mean diameter = 0.1 microns, max diameter = 2 microns) models with linearly polarized incident light [53]. The calculations were performed at limited specific wavelengths. The results were performed for wavelengths of 0.45, 0.7, and 5.3 microns for haze and 0.45, 0.7, 5.3, and 10 microns for clouds. He showed that numerical analysis could match previous experimental observations; as well as showing the use of particle size distributions suppresses resonant behavior seen in Mie theory for monodisperse particle distributions. Ryan and Carswell performed experiments in laboratory-generated fog looking at linearly polarized light's persistence and laser beam broadening (angular spread) at a wavelength of 514 nm [54]. In the central area of the beam core they found the degree of polarization was highly preserved after transmission through a meter of the fog. Various groups connected with Ishimaru have published simulations of degree of polarization and intensities for backscatter and transmission, as well as simulated imaging results for a specific fog model [30, 55–57]. The majority of their work uses a wavelength of 1 micron, but they also performed a set of calculations with wavelengths of 5, 10, and 15 microns. All of these previous fog models are limited to small particle fogs with a mean particle diameter of 1 micron and no particles larger than 8 microns. Recently, Miller *et al.* utilized circular polarization-difference imaging techniques as well as image processing algorithms to increase image contrast in laboratory-generated fog

scenes (mean diameter = 4 microns, maximum diameter produced = 12 microns); however, his work was also limited to a single visible illuminating wavelength (632.8 nm) [58]. Fade *et al.* experimented in outdoor fog conditions of unreported density and particle size, imaging a polarized 3000K halogen incandescent source from a distance of 1.3 km. They utilized only linear polarization for both illumination and polarization-difference detection, but were able to measure a 4 times increase in contrast [59]. These publications add to the previously published work investigating polarized light in scattering environments. Though these results are for near real-world scattering environments they are still limited in their illuminating wavelengths, polarization, and narrow particle size distribution and small mean diameter fog models.

1.4 **Polarization Memory**

All sensing techniques using polarization in scattering environments rely on the polarization persistence of light through propagation, often called polarization memory. Techniques typically utilize the difference between the illuminating polarization that persists to the target and the polarization response of the scattering background [60]. Circular polarization is of increasing interest due to its potentially superior persistence in scattering environments. MacKintosh *et al.* was one of the first to investigate and propose a mechanism as to why circular polarization exhibited a greater polarization memory and persistence than linear polarization [61]. Their work focused on scattering environments of polystyrene microspheres in water smaller and larger than the wavelengths. A wavelength of 488 nm was used with particle sizes

of 0.091 and 0.605 microns. They analytically show that the circular polarization memory for this scattering environment arises due to the wave's helicity being randomized at a slower rate than the wave's direction. A larger number of scattering events are required to remove the helicity of the circularly polarized light; therefore, the helicity is preserved over longer ranges, specifically for the larger particle size. Xu and Alfano have also analytically explored the mechanism behind the persistence of circular polarization [62]. They also hypothesize that the two mechanisms that depolarize circularly polarized light, and therefore affect its persistence, are the randomization of the photon's direction and the randomization of the helicity. They find that circular polarization persists superiorly for large particles with refractive indices close to the air environment (refractive index ~ 1) and for small, high index contrast particles (refractive indices between 1.5 and 2). The range at which circularly polarized light loses its helicity is largest for scattering environments with these types of particles. Macdonald *et al.* recently explored circular polarization memory for polydisperse particle size scattering environments [63]. They specifically investigated narrow polydisperse environments with 10% coefficient of variance around the mean particle size. The polydispersion of the environment removes the resonant behavior found in monodisperse calculations.

1.5 **Significance of this Work**

This chapter has reviewed a number of publications in this field. This dissertation, encompassing the work published in the previously mentioned significant contributions, presents unique additions to this field. In order to visually display this fact,

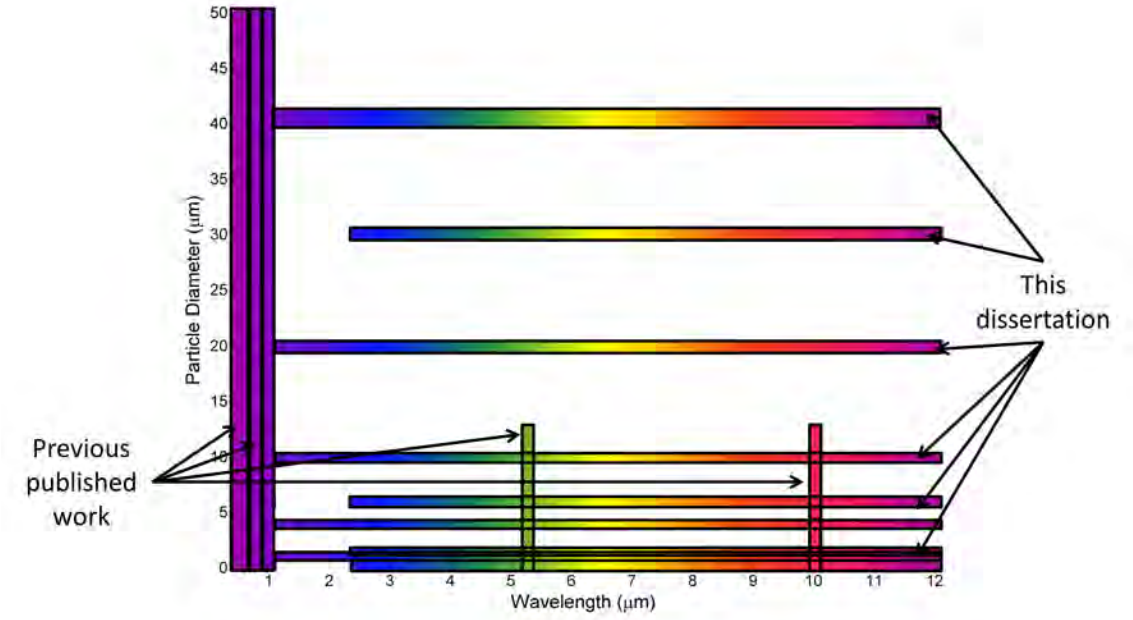

Figure 1.3: Comparison of previous publications and this dissertation's work.

Figure 1.3 was created. Most of the publications reviewed here were performed in the visible spectrum and are encompassed in the left three rectangles. This area is full in the figure but even this area is heavily focused on single wavelength experiments and simulations. There are only a couple previous simulation results for environments at infrared wavelengths. In contrast, this work simulates and experimentally shows circular polarization's persistence, or memory, benefits over broad environmental parameter spaces and wavelength ranges. This work also details the evolution and modification of both circularly and linearly polarized light through these types of scattering environments.

CHAPTER 2

Background Theory

2.1 Polarization and Polarimetry

Light fields have four physical properties: intensity, wavelength, coherence, and polarization. Changes in these properties produce the wide array of light that we interact with every day. Traditionally, optical imaging and sensing systems only measure two of these four properties, intensity and wavelength. The less utilized property of light that is of importance for this dissertation is polarization. Humans do not possess the ability to sense polarization, and can only observe the intensity and wavelength of light within a small range. As a result, it has been hard for humans to fully understand and utilize this valuable property. In 1669 Erasmus Bartholinus first discovered the property of light now known as polarization [1]. Following Bartholinus' discovery, polarization was not fully understood or explained by the scientific community for over one hundred years. It wasn't until the wave theory of light was validated in 1801 by Thomas Young's experiments and observations that the polarization of light could be better understood [64]. In 1808 Etienne-Louis Malus observed the polarization dependence of reflected light from a surface using a calcite crystal. His observations and subsequent memoir were the first to use the term polarization for this property of light [65]. Other scientists continued exploring and attempting to quantitatively measure the polarization of

light producing some of the first experiments in the field of polarimetry. A few of the first notable experiments in the quantitative polarimetry field were performed by Dominique François Jean Arago, Augustin-Jean Fresnel, and Robert A. Millikan. In 1819 Arago and Fresnel investigated the interference of various linear polarizations [66]. In 1824 Arago observed the polarization of light emitted by incandescent metals showing natural light is not always unpolarized [67]. Similarly, Millikan studied the polarization of light from incandesant solid and liquid surfaces [68]. Ultimately, the unification of the complete electromagnetic theory and its corresponding equations by Maxwell led to the full understanding of transverse fields and the vector nature of light.

Polarization defines the oscillation of the electric field in space and time, perpendicular to light's propagation direction [69]. The electric field traces out an ellipse for an arbitrary polarization state. The elliptical state encompasses the most commonly used polarization states which are special cases, linear and circular polarization. Once polarization was beginning to be understood, scientists needed a mathematical representation to define the polarization of observed light. Currently, there are two different mathematical formulations to describe the polarization of light.

2.1.1 **Jones Formalism**

The first formulation is that developed by R. Clark Jones in the 1940's and is thus called Jones Calculus [70–72]. Jones Calculus describes purely polarized light in terms of its amplitude and phase. The Jones formulation is of importance when

phase information is necessary. The electric field is defined by its two transverse components. The two components are complex quantities. The Jones vector is given by Equation 2.1,

$$\mathbf{J} = \begin{bmatrix} E_{\parallel} \\ E_{\perp} \end{bmatrix} = \begin{bmatrix} E_{0\parallel} e^{i\delta_{\parallel}} \\ E_{0\perp} e^{i\delta_{\perp}} \end{bmatrix}, \tag{2.1}$$

where $\parallel$ corresponds to the parallel component, $\perp$ corresponds to the perpendicular component, and the subscript 0 corresponds to the maximum amplitude values.

When light encounters an optical element or a process that changes the polarization state, that process is defined by a Jones matrix. The Jones matrix is a 2x2 matrix which mathematically represents the process changing an input Jones vector into the resulting output Jones vector polarization. The Jones calculus for an arbitrary input polarization and arbitrary Jones matrix is shown in Equation 2.2.

$$\begin{bmatrix} E_{\parallel out} \\ E_{\perp out} \end{bmatrix} = \begin{bmatrix} a & b \\ c & d \end{bmatrix} \begin{bmatrix} E_{\parallel in} \\ E_{\perp in} \end{bmatrix} \tag{2.2}$$

2.1.2 **Stokes Formalism**

The second polarization formulation is that developed by Sir George G. Stokes in 1852 [73]. As opposed to the Jones formulation, Stokes formulation is represented by observable intensity measurements. Due to this, Stokes formulation does not track phase information but can represent unpolarized light, which is not possible in the Jones formulation. Throughout most of this dissertation the Stokes formulation is more appropriate since it can handle the effects of depolarization. Any general

polarization state can be represented by four quantities, called Stokes parameters, which make up what is called the Stokes vector. The general Stokes vector for arbitrarily polarized light is given by,

$$\vec{\mathbf{S}} = \begin{bmatrix} S_0 \\ S_1 \\ S_2 \\ S_3 \end{bmatrix} = \begin{bmatrix} I \\ Q \\ U \\ V \end{bmatrix} = \begin{bmatrix} \langle E_\parallel E_\parallel^* + E_\perp E_\perp^* \rangle \\ \langle E_\parallel E_\parallel^* - E_\perp E_\perp^* \rangle \\ \langle E_\parallel E_\perp^* + E_\perp E_\parallel^* \rangle \\ i\langle E_\parallel E_\parallel^* - E_\perp E_\parallel^* \rangle \end{bmatrix} \propto \begin{bmatrix} I_H + I_V \\ I_H - I_V \\ I_{45^\circ} - I_{135^\circ} \\ I_{RHC} - I_{LHC} \end{bmatrix}, \tag{2.3}$$

where $\parallel$ corresponds to the parallel component, $\perp$ corresponds to the perpendicular component, and $*$ corresponds to the complex conjugate. The Stokes parameters have multiple naming conventions due to historical reasons but also to reduce confusion in subsequent analysis where the term s is also used for scattering functions [74, 75]. The Stokes parameters are proportional to measured flux values for a set of specific polarizer orientations. The S_0 term is the total intensity of the light, S_1 is the difference between linear horizontally polarized and linear vertically polarized flux, S_2 gives the difference between the linear 45° polarized and linear 135° flux, and S_3 gives the difference between right and left circularly polarized flux. As a result, the Stokes parameters must obey the equation $S_0^2 \geq S_1^2 + S_2^2 + S_3^2$.

In nature the transverse components of the electric field are functions of time. The correlation between the two components determines how polarized the light is in time. If the two transverse components are completely uncorrelated the light is considered unpolarized. Most natural light is considered unpolarized although that is not always the case. For unpolarized light, at any given instance in time

the polarization ellipse may trace a specific state, but over a period of time the ellipses will blur together and show no preference toward any polarization. If the two transverse components are completely correlated then the light is considered purely polarized. Finally, if the two components are partially correlated the light is considered partially polarized. A general Stokes vector is made up of a combination of a purely polarized portion and a completely unpolarized portion which together create varying amounts of partial polarization. In order to determine how polarized a measured light is, a mathematical tool is needed. This mathematical tool is called the Degree of Polarization (DoP). The percentage of the total intensity of light that is purely polarized is defined as the DoP. The equation for the DoP is shown in Equation 2.4.

$$DoP = \frac{\sqrt{S_1^2 + S_2^2 + S_3^2}}{S_0} \tag{2.4}$$

The DoP can vary between 0 (completely unpolarized light) to 1 (purely polarized light). Any Stokes vector with a DoP between 0 and 1 is partially polarized and can be separated into its purely polarized and unpolarized Stokes vectors shown in Equation 2.5.

$$\vec{\mathbf{S}} = \vec{\mathbf{S}}_{polarized} + \vec{\mathbf{S}}_{unpolarized} = \begin{bmatrix} \sqrt{S_1^2 + S_2^2 + S_3^2} \\ S_1 \\ S_2 \\ S_3 \end{bmatrix} + \begin{bmatrix} S_0 - \sqrt{S_1^2 + S_2^2 + S_3^2} \\ 0 \\ 0 \\ 0 \end{bmatrix} \tag{2.5}$$

Figure 2.1 shows some examples of the trace of the electric field vector in time for varying DoP. The figures show the difference between the random oscillations of partially polarized light and the structured oscillations of polarized light.

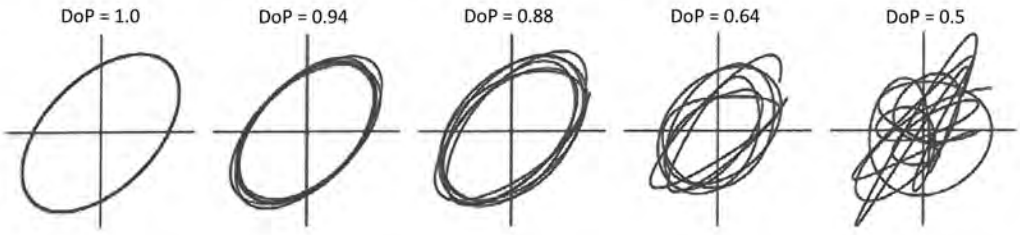

Figure 2.1: Electric field oscillations in time for varying DoP for elliptically polarized light [76].

Along with the DoP there are two related quantities, the Degree of Linear Polarization ($DoLP$) and the Degree of Circular Polarization ($DoCP$). The $DoLP$ is a positive quantity while $DoCP$ can be positive or negative which determines the circular helicity of the polarization. The two quantities are defined in Equation 2.6 and Equation 2.7.

$$DoLP = \frac{\sqrt{S_1^2 + S_2^2}}{S_0} \tag{2.6}$$

$$DoCP = \frac{S_3}{S_0} \tag{2.7}$$

Similar to Jones calculus and the Jones matrix, there is a matrix operation for the Stokes formulation that represents the interaction of polarized light with a process or element that changes the polarization state. The matrices are called Mueller

matrices after their creator, Hans Mueller, who developed them in the 1940's [69]. The Mueller matrix is made up of sixteen elements in a 4x4 matrix. The arbitrary Mueller matrix is shown in Equation 2.8 in a general Mueller calculus operation. The input Stokes vector is on the right and the resulting output Stokes vector is on the left.

$$\begin{bmatrix} S_0 \\ S_1 \\ S_2 \\ S_3 \end{bmatrix}_{out} = \begin{bmatrix} m_{11} & m_{12} & m_{13} & m_{14} \\ m_{21} & m_{22} & m_{23} & m_{24} \\ m_{31} & m_{32} & m_{33} & m_{34} \\ m_{41} & m_{42} & m_{43} & m_{44} \end{bmatrix} \begin{bmatrix} S_0 \\ S_1 \\ S_2 \\ S_3 \end{bmatrix}_{in} \tag{2.8}$$

Once a process or element's Mueller matrix is determined it can easily be used in Mueller calculus to determine any exiting polarization state from any incident polarization state.

2.1.3 **Polarimetry**

Polarimetry is the science of measuring the polarization state of light. In general there are two types of polarimetry, Stokes and Mueller Matrix polarimetry. For Stokes polarimetry only the four Stokes vector parameters are desired. In general, the measurement process can be shown in matrix format as,

$$\mathbf{I} = \mathbf{AS} \tag{2.9}$$

where **S** is the incident Stokes vector to be measured, **A** is the analyzer matrix whose size depends on the number of measurements and whose element values are

dependent on the optical system measuring the polarization, and **I** is a vector of the flux measurements made by the detector. Ultimately, the incident Stokes vector parameters are desired so an inverse equation is used.

$$\mathbf{S} = \mathbf{A}^{-1}\mathbf{I} \tag{2.10}$$

From the set of measurements a set of equations are generated which can be solved through Fourier or non-Fourier methods. The methods used for this dissertation will be explained in more detail in Chapter 4. For Mueller Matrix polarimetry the complete sixteen elements of the 4x4 Mueller matrix are measured. Mueller Matrix polarimetry is generally used for characterization of materials in reflection or transmission. For Mueller Matrix polarimetry the incident Stokes polarization state is known and changed. The resulting reflected or transmitted Stokes vectors are used to determine the elements of the Mueller matrix. In order to measure all sixteen elements of the Mueller matrix, sixteen settings of incident Stokes vectors and analyzer orientations need to be used in order to generate sixteen equations for the sixteen unknowns. The equations are generated similarly to the Stokes polarimetry equations. The matrix representation of the process is defined by,

$$\mathbf{I} = \mathbf{AMS}, \tag{2.11}$$

where **I** is the measured intensity at the detector, **A** is the analyzer matrix, **M** is the Mueller matrix of the material, **S** is the incident Stokes vector which is the result of a polarization state generator that can be changed for each measurement.

The following sections will show how the single scattering Mueller matrix is calculated and used in simulations.

2.2 Scattering Theory

Before delving into the physics of the scattering theory it is important to take a look at the various particle size regimes that exist and the important assumptions made for each, leading to why Mie Theory is the proper regime choice for this dissertation. A general solution to the problem of scattering is nearly impossible due to the vast complexity of nature. As a result, various approximations are made to simplify calculations in order for scientists to gain some insight.

One of the first approximations was done by Lord Rayleigh (John William Strutt) in 1871 as a result of his pursuit to solve the age old question of why the sky is blue. Rayleigh answered this question and his scattering solution was shown to be valid for any small particle where the radius of the particle is less than or equal to 5 percent of the wavelength of light being investigated [77]. Additional approximations followed which looked to fill in gaps which Rayleigh's solution could not cover. The Born approximation, or Rayleigh-Debye scattering, is another solution that is valid when $(\epsilon_r - 1)kD \ll 1$, where ϵ_r, k, D are the relative dielectric constant, wave number, and typical dimension of the particle, respectively. This approximation accounts for larger sized particles if the index of refraction and wavelength satisfy the approximations validity equation. Additionally, the WKB (Wentzel, Kramers, and Brillouin) Interior Wave Number approximation was developed and is valid if $(\epsilon_r - 1)kD \gg 1$ and $(\epsilon_r - 1) < 1$ providing a solution that is not applicable to

the Rayleigh or Born approximations. All of these approximations have limited value due to somewhat complicated validity regimes. The last approximation is the most important for the remaining analysis in this dissertation. At roughly the same time both Ludvig Lorenz and Gustav Mie solved the problem of scattering of plane electromagnetic waves by an isotropic, homogenous spherical particle [78]. In general, the solution has since been attributed to Mie and is thus called Mie Theory. The only approximations used in Mie Theory are that the particle has homogenous index and perfectly spherical shape. The common misconception of Mie Theory is that it only applies to particles larger than the wavelength, which is not the case. As a result, Mie Theory can be used to simulate the scattering properties of a particle of any size and index as long as it is assumed spherical. In nature, rarely are particles perfectly spherical, however Mie Theory provides first-order insight into the scattering properties of natural non-spherical particles. This is of great benefit to the scientific community, which is why it is heavily used to this day.

2.2.1 **Mie Scattering Theory**

To completely solve the scattering effects due to particles, Maxwell's equations must be solved for the various boundary conditions of the particle of interest. Maxwell's equations are the only starting point when investigating rigorous solutions of interactions of radiation and the environment. As has been stated, a specific solution of Maxwell's equations for homogeneous spherical particles of any size and index was developed by Mie and shall be explained in limited detail here. It is assumed that the reader knows and understands Maxwell's equations and the resulting boundary

conditions.

Electromagnetic radiation, which includes light, must obey the wave equation in order to be physically realizable. The wave equation is given below using the electric field as example. The magnetic field also obeys this equation.

$$\nabla^2 \mathbf{E} + k^2 \mathbf{E} = 0 \tag{2.12}$$

The constant k is the wavenumber in the medium defined as,

$$k^2 = \omega^2 \epsilon \mu. \tag{2.13}$$

In order to find solutions to the wave equation we define a set of vector functions $\mathbf{M}$ and $\mathbf{N}$, each made up of a scalar function ψ and a constant vector $\mathbf{c}$.

$$\mathbf{M} = \boldsymbol{\nabla} \times (\boldsymbol{c}\psi) \tag{2.14a}$$

$$\mathbf{N} = \frac{\boldsymbol{\nabla} \times \mathbf{M}}{k} \tag{2.14b}$$

Both M and N satisfy the vector wave equations and it can be shown that,

$$k\mathbf{M} = \boldsymbol{\nabla} \times \mathbf{N}. \tag{2.15}$$

If the function $\mathbf{M}$ adheres to the vector wave equation then ψ must obey the scalar wave equation.

$$\nabla^2 \psi + k^2 \psi = 0 \tag{2.16}$$

Thus, the vector functions **M** and **N** satisfy the necessary qualities of electromagnetic radiation. Utilizing the proper symmetries of a given problem we are able to find the scalar function ψ, and thus solve for the vector field functions **M** and **N** which lead directly to the **E** and **H** fields. Mie's solution to Maxwell's equations assume the scattering particle in the medium of interest is a homogenous sphere with a radius of a. As a result of this single simplification spherical coordinates using symbols r, θ, φ are used to determine the solution. The vector **c** previously used is then replaced with the position vector **r**. Figure 2.2 shows the spherical coordinate system for a spherical particle centered at the origin.

The solution to the scalar wave equation in spherical coordinates is expected to be of the form,

$$\psi(r, \theta, \varphi) = R(r)\Theta(\theta)\Phi(\varphi). \tag{2.17}$$

The solutions to $\Phi(\varphi)$ are given by,

$$\Phi_e = cos(m\varphi) \tag{2.18}$$

$$\Phi_o = sin(m\varphi) \tag{2.19}$$

where the e and o correspond to the even and odd solutions, respectively, and m is an integer.

The solutions to $\Theta(\theta)$ are given by $P_n^m(cos(\theta))$ which are the associated Legendre functions of the first kind of degree n and order m. The integers must satisfy $n \geq m \geq 0$.

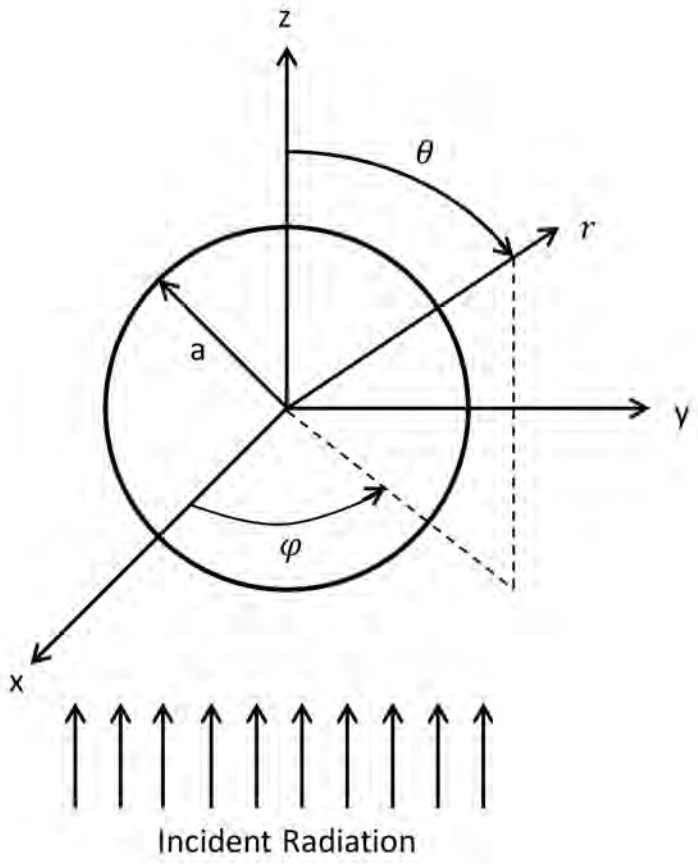

Figure 2.2: Spherical coordinate system for the scattering problem of a sphere of radius a [79].

Lastly, the solutions to $R(r)$ are given by the spherical Bessel functions,

$$j_n(kr) = \sqrt{\frac{\pi}{2kr}} J_{n+1/2}(kr), \tag{2.20}$$

$$y_n(kr) = \sqrt{\frac{\pi}{2kr}} Y_{n+1/2}(kr), \tag{2.21}$$

or any two linearly independent combinations of these equations. Two linear combinations of particular interest are the spherical Hankel functions,

$$h_n^{(1)}(kr) = j_n(kr) + iy_n(kr), \tag{2.22}$$

$$h_n^{(2)}(kr) = j_n(kr) - iy_n(kr). \tag{2.23}$$

Any of these four solutions can be used and thus will all be represented as $z_n(kr)$.

The solution to the scalar wave equation is thus given by,

$$\psi_{emn} = cos(m\varphi) P_n^m(cos(\theta)) z_n(kr), \tag{2.24}$$

$$\psi_{omn} = sin(m\varphi) P_n^m(cos(\theta)) z_n(kr). \tag{2.25}$$

Inserting these into the equations for the vector functions $\mathbf{M}$ and $\mathbf{N}$ give the following solutions,

$$\boldsymbol{M}_{emn} = \frac{-m}{sin(\theta)} sin(m\varphi) P_n^m(cos(\theta)) z_n(kr) \hat{\boldsymbol{\theta}} - cos(m\varphi) \frac{d}{d\theta} [P_n^m(cos(\theta))] z_n(kr) \hat{\boldsymbol{\varphi}} \tag{2.26}$$

$$\boldsymbol{M}_{omn} = \frac{m}{sin(\theta)} cos(m\varphi) P_n^m(cos(\theta)) z_n(kr)\hat{\boldsymbol{\theta}} - sin(m\varphi)\frac{d}{d\theta}[P_n^m(cos(\theta))] z_n(kr)\hat{\boldsymbol{\varphi}} \tag{2.27}$$

$$\begin{aligned}\boldsymbol{N}_{emn} = {} & \frac{z_n(kr)}{kr} cos(m\varphi) n(n+1) P_n^m(cos(\theta))\hat{\boldsymbol{r}} \\ & + cos(m\varphi)\frac{d}{d\theta}[P_n^m(cos(\theta))]\frac{1}{kr}\frac{d}{d(kr)}[krz_n(kr)]\hat{\boldsymbol{\theta}} \\ & - msin(m\varphi)\frac{P_n^m(cos(\theta))}{sin(\theta)}\frac{1}{kr}\frac{d}{d(kr)}[krz_n(kr)]\hat{\boldsymbol{\varphi}}\end{aligned} \tag{2.28}$$

$$\begin{aligned}\boldsymbol{N}_{omn} = {} & \frac{z_n(kr)}{kr} sin(m\varphi) n(n+1) P_n^m(cos(\theta))\hat{\boldsymbol{r}} \\ & + sin(m\varphi)\frac{d}{d\theta}[P_n^m(cos(\theta))]\frac{1}{kr}\frac{d}{d(kr)}[krz_n(kr)]\hat{\boldsymbol{\theta}} \\ & + mcos(m\varphi)\frac{P_n^m(cos(\theta))}{sin(\theta)}\frac{1}{kr}\frac{d}{d(kr)}[krz_n(kr)]\hat{\boldsymbol{\varphi}}\end{aligned} \tag{2.29}$$

These equations are the vector harmonics of the fields. With these equations it is now possible to tackle the problem Mie first solved, scattering of a plane wave by an arbitrary sphere.

Assuming an incident plane wave polarized in the x direction, the incident electric field is,

$$\boldsymbol{E}_i = E_0 e^{ikrcos(\theta)}\hat{\boldsymbol{x}}. \tag{2.30}$$

Where $\hat{\boldsymbol{x}} = sin(\theta)cos(\varphi)\hat{\boldsymbol{r}} + cos(\theta)cos(\varphi)\hat{\boldsymbol{\theta}} - sin(\varphi)\hat{\boldsymbol{\varphi}}$ when defined in spherical coordinates. In order to find the solution for a spherical particle the incident plane wave must be defined in terms of vector spherical harmonics,

$$\boldsymbol{E}_i = \sum_{m=0}^{\infty}\sum_{n=0}^{\infty} B_{emn}\boldsymbol{M}_{emn} + B_{omn}\boldsymbol{M}_{omn} + A_{emn}\boldsymbol{N}_{emn} + A_{omn}\boldsymbol{N}_{omn}. \tag{2.31}$$

The A and B terms are scalar factors. The full derivation and solution of expanding

a plane wave in terms of spherical harmonics is explained in detail in Bohren and Huffman [79]. For the purposes of this dissertation I will skip to the expansion and leave the derivation for the reader to investigate.

The incident x-polarized plane wave's electric and magnetic fields expanded in spherical harmonics are,

$$\boldsymbol{E}_i = E_0 \sum_{n=1}^{\infty} i^n \frac{2n+1}{n(n+1)} (\boldsymbol{M}_{o1n}^{(1)} - i\boldsymbol{N}_{e1n}^{(1)}), \tag{2.32}$$

$$\boldsymbol{H}_i = \frac{-k}{\omega\mu} E_0 \sum_{n=1}^{\infty} i^n \frac{2n+1}{n(n+1)} (\boldsymbol{M}_{e1n}^{(1)} + i\boldsymbol{N}_{o1n}^{(1)}). \tag{2.33}$$

The superscript (1) defines $z_n(kr) = j_n(kr)$, which is the correct choice of the possible functions, as well as $m = 1$, due to satisfaction of a finite field at the origin and orthogonality of the base functions.

With the incident field now defined ($\boldsymbol{E}_i$), the internal field in the spherical particle ($\boldsymbol{E}_I$) and the resulting scattered field ($\boldsymbol{E}_s$) can be found from the boundary conditions. The boundary conditions for a sphere and the surrounding medium are,

$$(\boldsymbol{E}_i + \boldsymbol{E}_s - \boldsymbol{E}_I) \times \hat{\boldsymbol{r}} = (\boldsymbol{H}_i + \boldsymbol{H}_s - \boldsymbol{H}_I) \times \hat{\boldsymbol{r}} = 0. \tag{2.34}$$

The internal field is thus defined as,

$$\boldsymbol{E}_I = E_0 \sum_{n=1}^{\infty} i^n \frac{2n+1}{n(n+1)} (c_n \boldsymbol{M}_{o1n}^{(1)} - i d_n \boldsymbol{N}_{e1n}^{(1)}), \tag{2.35}$$

$$\boldsymbol{H}_I = \frac{-k_1}{\omega\mu_1} E_0 \sum_{n=1}^{\infty} i^n \frac{2n+1}{n(n+1)} (d_n \boldsymbol{M}_{e1n}^{(1)} + i c_n \boldsymbol{N}_{o1n}^{(1)}), \tag{2.36}$$

where k_1 is the wavenumber in the sphere, and μ_1 is the permeability of the sphere.

Similarly, the scattered field is defined as,

$$\boldsymbol{E}_s = E_0 \sum_{n=1}^{\infty} i^n \frac{2n+1}{n(n+1)} (i a_n \boldsymbol{N}_{e1n}^{(3)} - b_n \boldsymbol{M}_{o1n}^{(3)}), \tag{2.37}$$

$$\boldsymbol{H}_s = \frac{k}{\omega\mu} E_0 \sum_{n=1}^{\infty} i^n \frac{2n+1}{n(n+1)} (i b_n \boldsymbol{N}_{o1n}^{(3)} + a_n \boldsymbol{M}_{e1n}^{(3)}), \tag{2.38}$$

where the superscript (3) denotes the use of $z_n(kr) = h_n^{(1)}(kr)$, in order for the scattered fields to correctly consist of a sum of outgoing spherical waves.

Currently, all the information needed to construct the scattered fields is present except the scattering coefficients a_n and b_n. Utilizing the boundary conditions and the correct set of parameters, the results for the scattering coefficients can be determined. First, the size parameter x and the relative refractive index m are defined as follows,

$$x = ka = \frac{2\pi n a}{\lambda}, \tag{2.39}$$

$$m = \frac{k_1}{k} = \frac{n_1}{n}, \tag{2.40}$$

where a is the radius of the sphere, n is the refractive index of the medium, n_1 is the refractive index of the sphere, and λ is the vacuum wavelength.

Second, the Riccati-Bessel functions must be defined to simplify the definitions.

$$\psi_n(\rho) = \rho j_n(\rho) \tag{2.41}$$

$$\xi_n(\rho) = \rho h_n^{(1)}(\rho) \tag{2.42}$$

Thus, the scattering coefficients are defined as,

$$a_n = \frac{m\psi_n(mx)\psi_n'(x) - \psi_n(x)\psi_n'(mx)}{m\psi_n(mx)\xi_n'(x) - \xi_n(x)\psi_n'(mx)}, \tag{2.43}$$

$$b_n = \frac{\psi_n(mx)\psi_n'(x) - m\psi_n(x)\psi_n'(mx)}{\psi_n(mx)\xi_n'(x) - m\xi_n(x)\psi_n'(mx)}. \tag{2.44}$$

With these coefficients all the measurable quantities desired from the processes of scattering and absorption can be determined.

2.3 Polarization in Mie Scattering Theory

The purpose of this dissertation is to investigate the interaction of polarized light and scattering objects in scattering environments, so at this point the notation and connection to Mie Theory for polarization will be described.

The interaction between arbitrarily polarized light and an arbitrary scattering particle is calculated from the amplitude scattering matrix. The relationship between the incident field and the scattering field is,

$$\begin{bmatrix} E_{\parallel s} \\ E_{\perp s} \end{bmatrix} = \frac{e^{ik(r-z)}}{-ikr} \begin{bmatrix} s_2 & s_3 \\ s_4 & s_1 \end{bmatrix} \begin{bmatrix} E_{\parallel i} \\ E_{\perp i} \end{bmatrix}. \tag{2.45}$$

In general, the terms in the amplitude scattering matrix are angularly dependent and also depend on the properties of the particle, medium, and the wavelength of the radiation. From the Jones matrix formulation a similar matrix can be constructed

for the Stokes formulation which uses Mueller calculus.

$$\begin{bmatrix} S_0 \\ S_1 \\ S_2 \\ S_3 \end{bmatrix}_{scat} = \frac{1}{k^2 r^2} \begin{bmatrix} s_{11} & s_{12} & s_{13} & s_{14} \\ s_{21} & s_{22} & s_{23} & s_{24} \\ s_{31} & s_{32} & s_{33} & s_{34} \\ s_{41} & s_{42} & s_{43} & s_{44} \end{bmatrix} \begin{bmatrix} S_0 \\ S_1 \\ S_2 \\ S_3 \end{bmatrix}_{in} \tag{2.46}$$

The various symmetry relations that a spherical particle satisfies allow for a simplification of the general scattering matrix. For spherical particles the matrix is simplified due to $s_3 = s_4 = 0$ [80]. As a result, the amplitude scattering Mueller matrix is simplified to,

$$\begin{bmatrix} s_{11} & s_{12} & 0 & 0 \\ s_{12} & s_{11} & 0 & 0 \\ 0 & 0 & s_{33} & s_{34} \\ 0 & 0 & -s_{34} & s_{33} \end{bmatrix}, \tag{2.47}$$

where $s_{11} = \frac{1}{2}(|s_2|^2 + |s_1|^2), s_{12} = \frac{1}{2}(|s_2|^2 - |s_1|^2), s_{33} = \frac{1}{2}(s_2^* s_1 + s_2 s_1^*), s_{34} = \frac{i}{2}(s_1 s_2^* - s_2 s_1^*)$.

The amplitude scattering functions can be determined from the previously solved Mie Theory solution for the electric field.

$$s_1(\theta) = \sum_n \frac{2n+1}{n(n+1)}(a_n \pi_n(cos(\theta)) + b_n \tau_n(cos(\theta)) \tag{2.48}$$

$$s_2(\theta) = \sum_n \frac{2n+1}{n(n+1)}(a_n \tau_n(cos(\theta)) + b_n \pi_n(cos(\theta)) \tag{2.49}$$

The functions π_n and τ_n are angularly dependent functions defined as,

$$\pi_n(cos(\theta)) = \frac{P_n^1(cos(\theta))}{sin(\theta)}, \tag{2.50}$$

$$\tau_n(cos(\theta)) = \frac{d}{d\theta}[P_n^1(cos(\theta))]. \tag{2.51}$$

Therefore, the amplitude scattering functions are angularly dependent functions as well. From the functions $s_1(\theta)$ and $s_2(\theta)$ the probability of scattering in a given angle can be determined. In general, the amplitude scattering functions are complex. In order to get the correct probability functions the amplitude scattering functions must be converted into flux scattering functions, the magnitude squared of the amplitude. Examples of the angular scattering probability functions are shown in Figure 2.3. The angular scattering probabilities for incident parallel polarized light (dashed blue) and perpendicular polarized light (black) is plotted for both a small isotropically scattering particle and a larger forward-scattering particle. Both the isotropic and forward scattering figures show the parallel and perpendicular plots, but for the forward-scattering particle the parallel and perpendicular plots are nearly the same.

As the analysis has shown, the scattering functions are dependent on the relative refractive index (m) and the size of the particle relative to the wavelength of light (size parameter x). To offer better insight into the variation of the scattering functions for these variables a set of figures will be presented for variations of the real and imaginary relative refractive indices for variations in the size parameters.

Figures 2.4 through Figure 2.8 show the variation of the scattering functions for

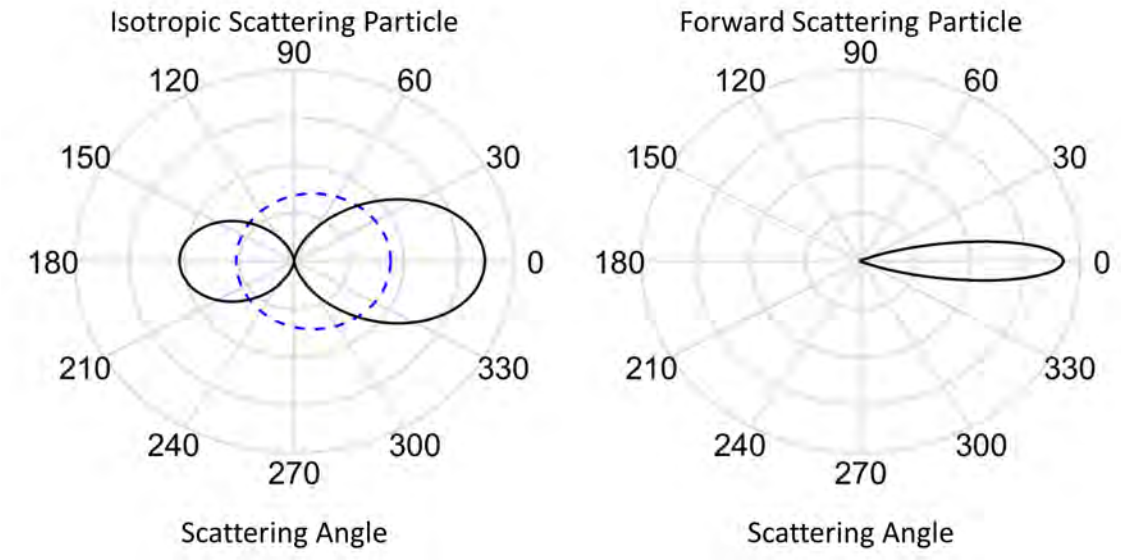

Figure 2.3: Scattering functions for an isotropic and forward-scattering particle. Blue corresponds to scattering probability for incident parallel polarization and black corresponds to incident perpendicular polarization. For the forward-scattering particle, the parallel and perpendicular components are the same.

purely real relative refractive index variation. Each figure shows results for a specific size parameter, ranging from 0.05 to 5, with variations of the real part of the relative refractive index ranging from 0.5 to 3.0. For all of these figures the imaginary index is set to 0. The plots show the transition from an isotropic to a forward-scattering particle.

Figures 2.9 through Figure 2.12 show the variation of the scattering functions for purely imaginary relative refractive index variation. Each figure shows results for a specific size parameter, ranging from 0.5 to 5, with variations of the imaginary part of the relative refractive index ranging from 0.01 to $1i$. For all of these figures the real part of the index is set to 1.0. The plots show the transition from an isotropic to a forward-scattering particle. Overall, the change in the imaginary relative refractive

index does not largely change the structure of the scattering function, but purely imaginary refractive index particles still scatter light.

The amplitude scattering matrix previously mentioned is the same as the single scattering Mueller matrix; the matrix represents the scattering properties of a single spherical scattering particle. With a known incident polarization Stokes vector, particle radius, particle refractive index, external medium index, and wavelength of light, the resulting Stokes vector of the scattered light can be determined for any scattering angle from the single scattering Mueller matrix. This is a powerful operation which is crucial to the use of polarization tracking Monte Carlo simulations.

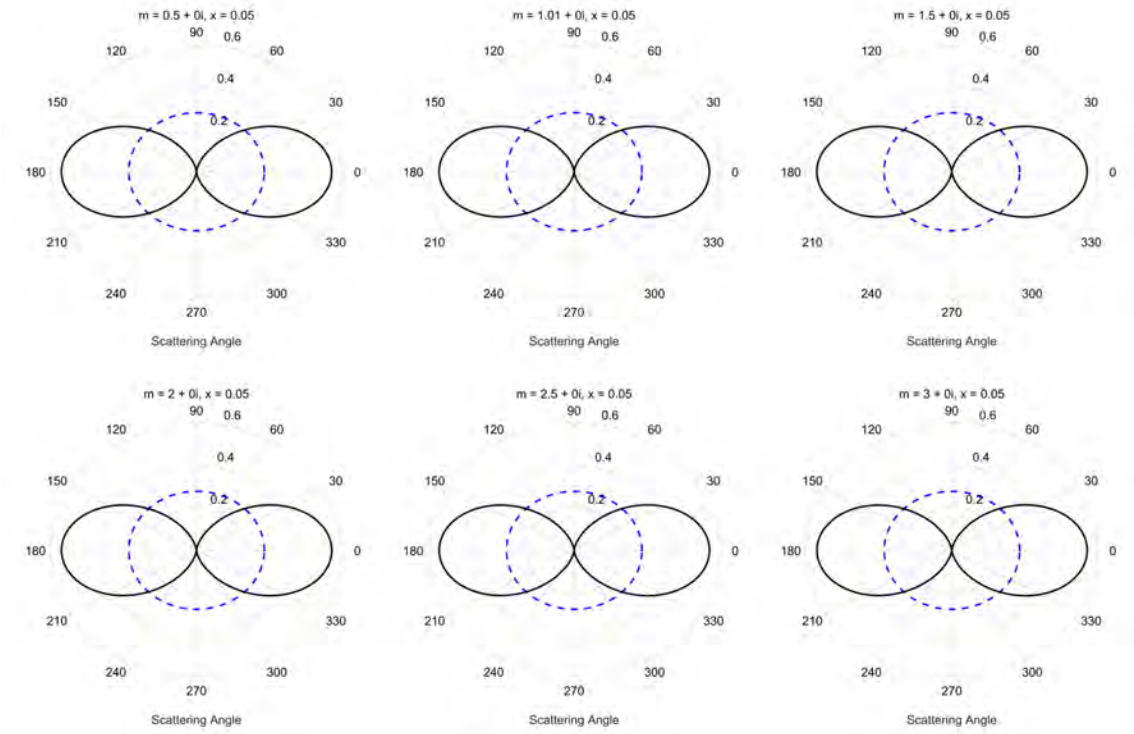

Figure 2.4: Scattering probability plots for a particle with size parameter $x = 0.05$ and varying real relative refractive index, ranging from 0.5 to 3.0. The imaginary index is set to 0 for all plots. The blue dashed line corresponds to the scattering probability for incident parallel polarization and the black solid line corresponds to incident perpendicular polarization.

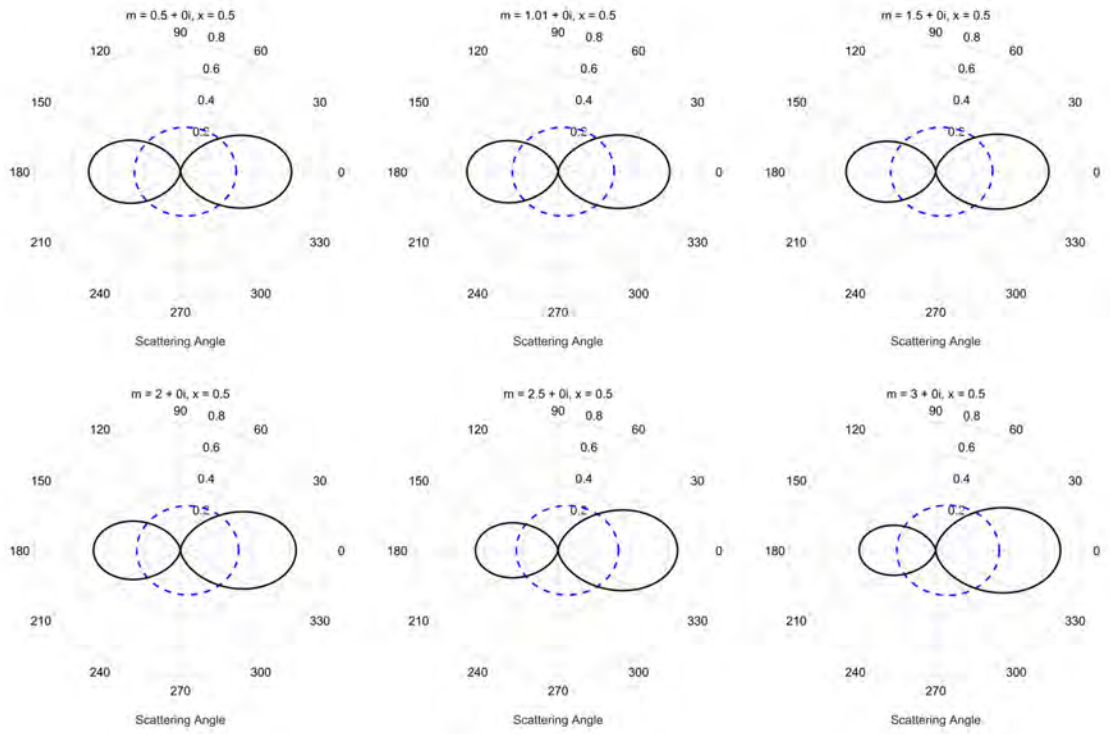

Figure 2.5: Scattering probability plots for a particle with size parameter $x = 0.5$ and varying real relative refractive index, ranging from 0.5 to 3.0. The imaginary index is set to 0 for all plots. The blue dashed line corresponds to the scattering probability for incident parallel polarization and the black solid line corresponds to incident perpendicular polarization.

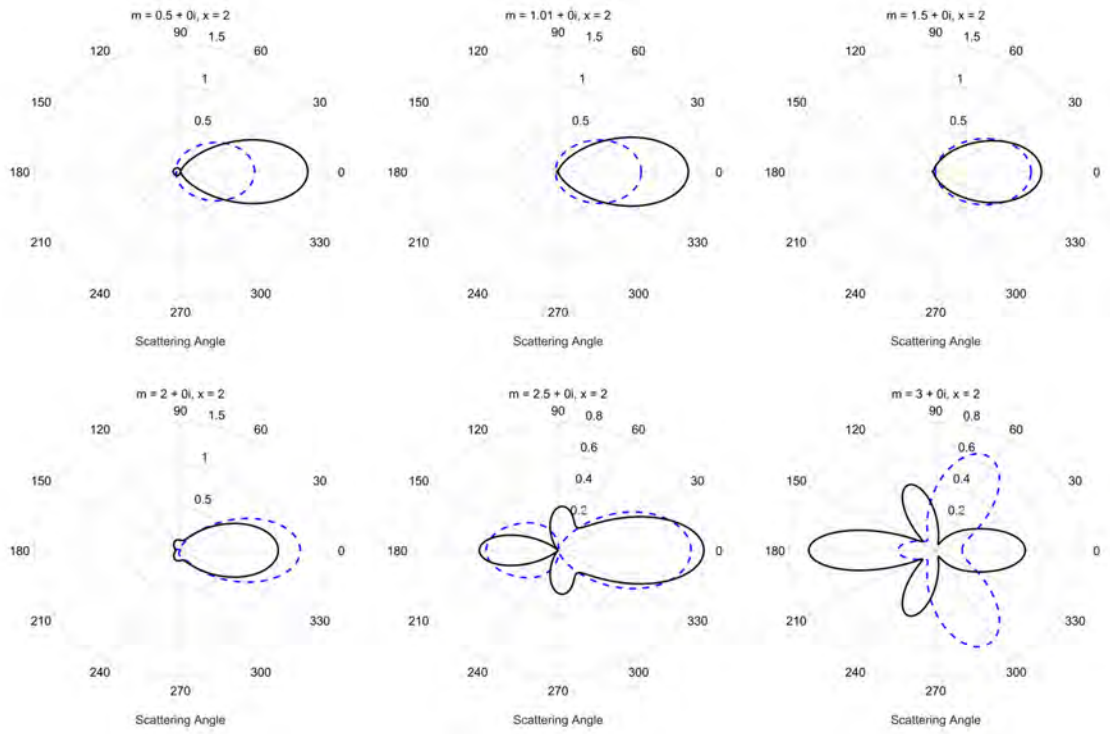

Figure 2.6: Scattering probability plots for a particle with size parameter $x = 2.0$ and varying real relative refractive index, ranging from 0.5 to 3.0. The imaginary index is set to 0 for all plots. The blue dashed line corresponds to the scattering probability for incident parallel polarization and the black solid line corresponds to incident perpendicular polarization.

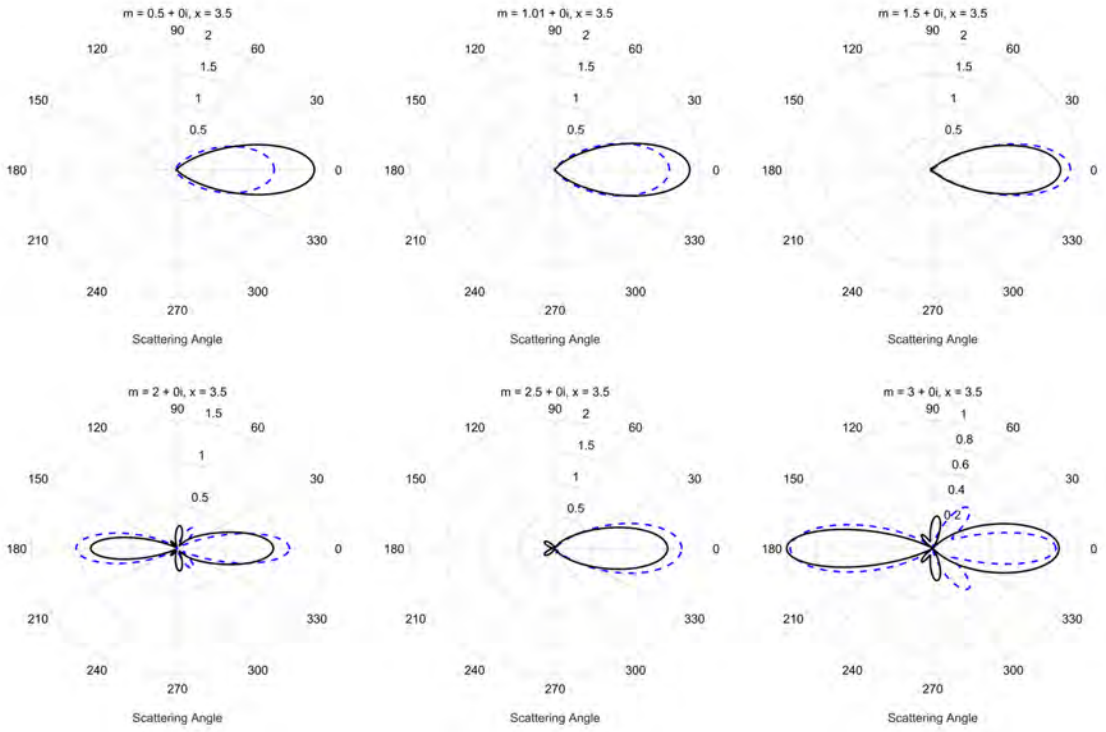

Figure 2.7: Scattering probability plots for a particle with size parameter $x = 3.5$ and varying real relative refractive index, ranging from 0.5 to 3.0. The imaginary index is set to 0 for all plots. The blue dashed line corresponds to the scattering probability for incident parallel polarization and the black solid line corresponds to incident perpendicular polarization.

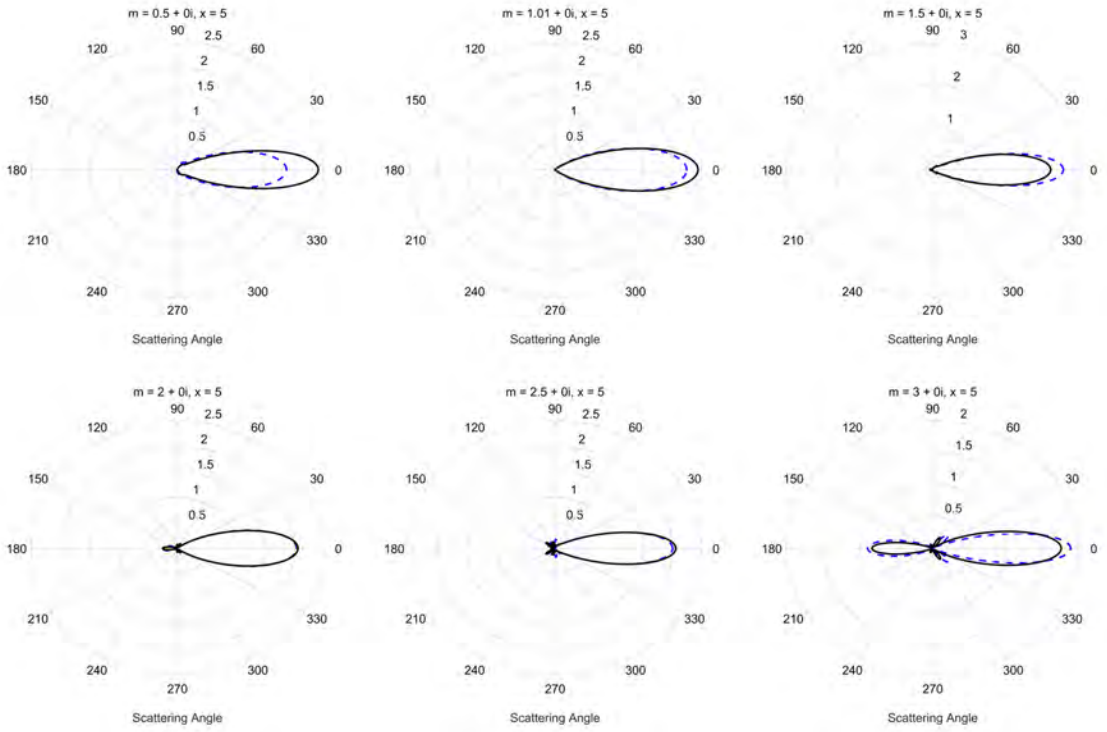

Figure 2.8: Scattering probability plots for a particle with size parameter $x = 5.0$ and varying real relative refractive index, ranging from 0.5 to 3.0. The imaginary index is set to 0 for all plots. The blue dashed line corresponds to the scattering probability for incident parallel polarization and the black solid line corresponds to incident perpendicular polarization.

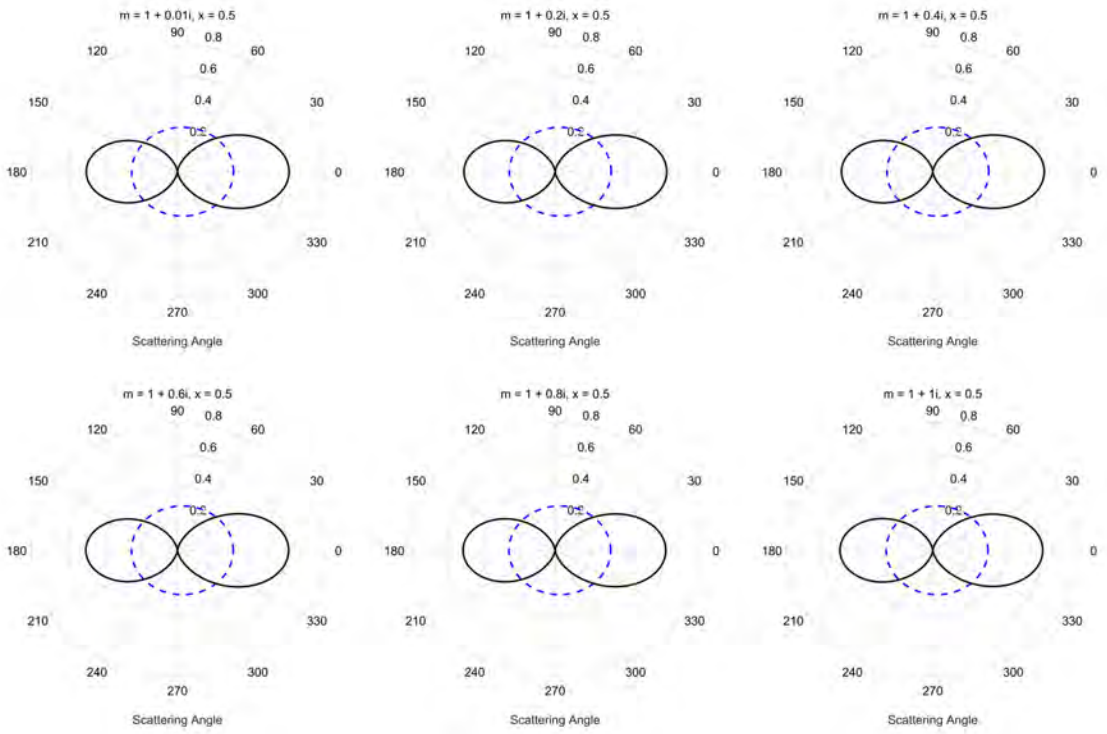

Figure 2.9: Scattering probability plots for a particle with size parameter $x = 0.5$ and varying imaginary relative refractive index, ranging from 0.01 to $1i$. The real index is set to 1.0 for all plots. The blue dashed line corresponds to the scattering probability for incident parallel polarization and the black solid line corresponds to incident perpendicular polarization.

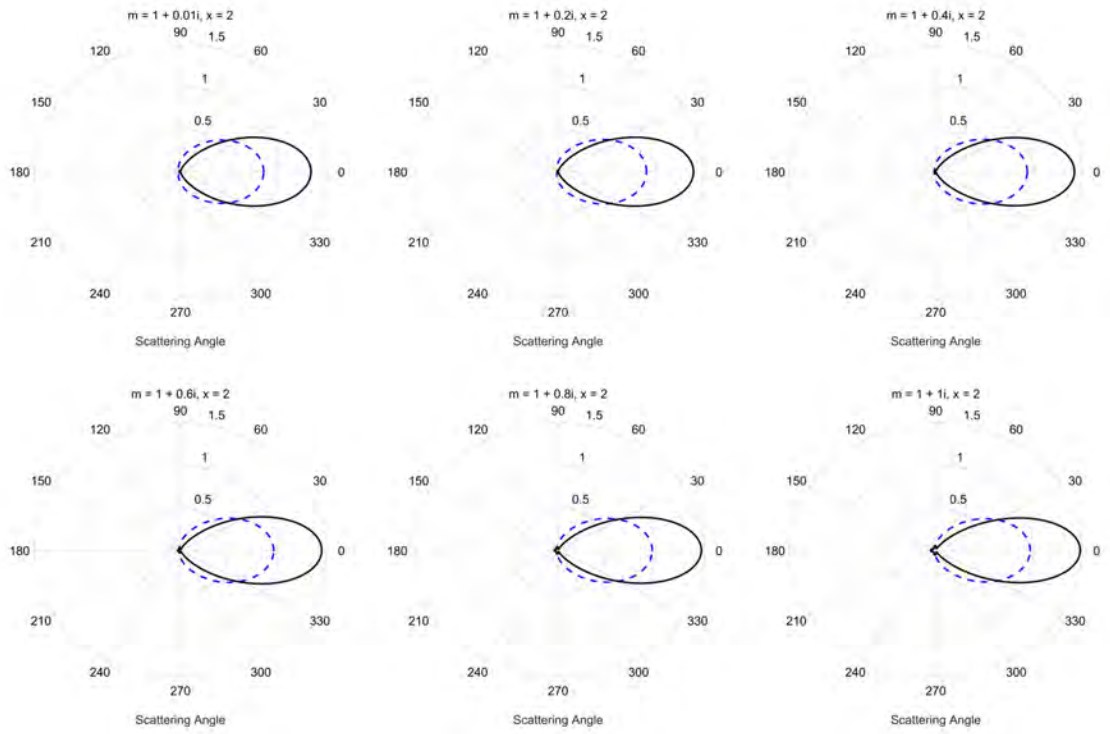

Figure 2.10: Scattering probability plots for a particle with size parameter $x = 2.0$ and varying imaginary relative refractive index, ranging from 0.01 to $1i$. The real index is set to 1.0 for all plots. The blue dashed line corresponds to the scattering probability for incident parallel polarization and the black solid line corresponds to incident perpendicular polarization.

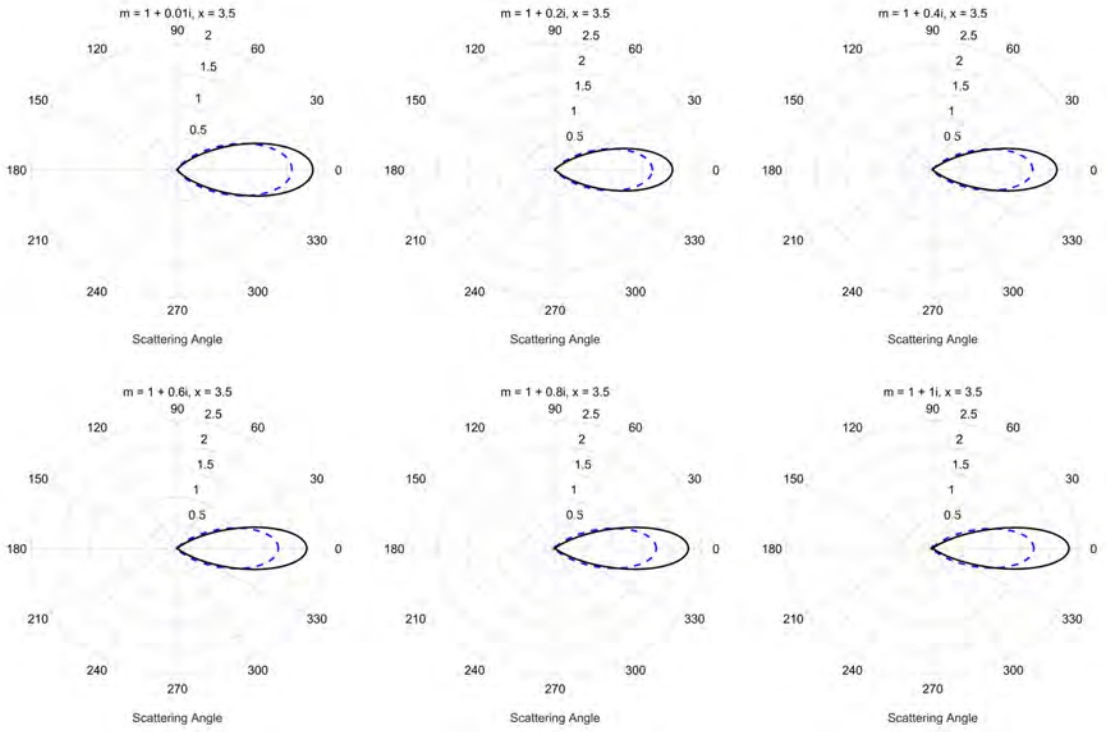

Figure 2.11: Scattering probability plots for a particle with size parameter $x = 3.5$ and varying imaginary relative refractive index, ranging from 0.01 to $1i$. The real index is set to 1.0 for all plots. The blue dashed line corresponds to the scattering probability for incident parallel polarization and the black solid line corresponds to incident perpendicular polarization.

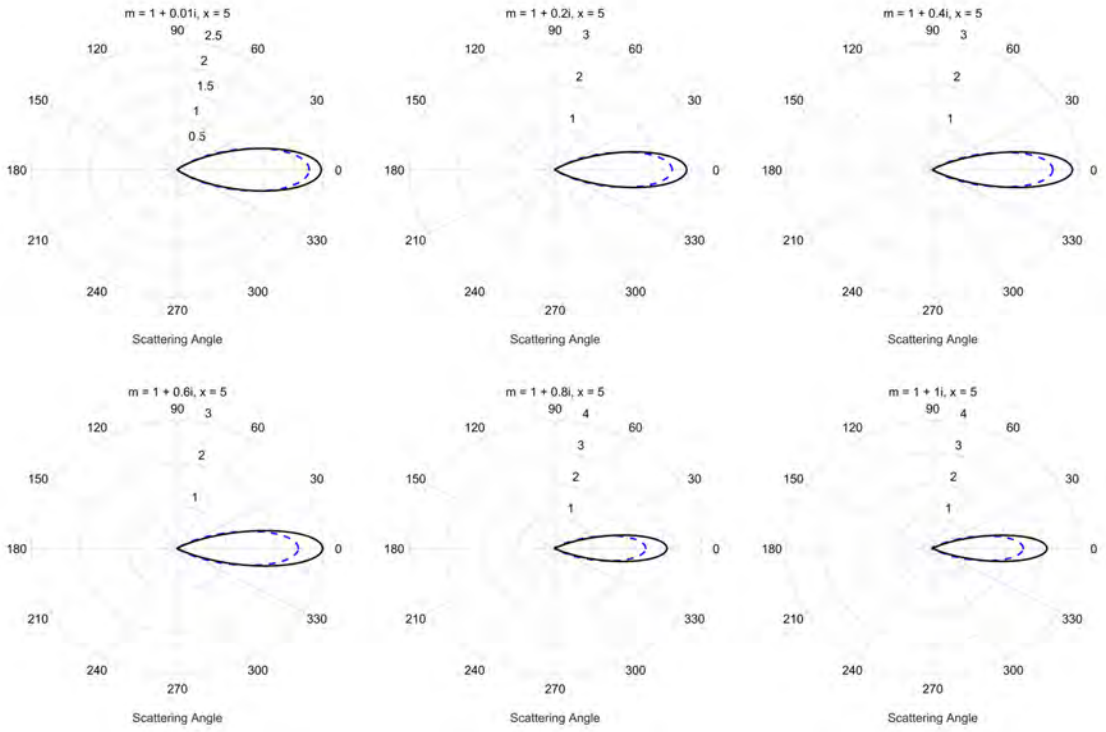

Figure 2.12: Scattering probability plots for a particle with size parameter $x = 5.0$ and varying imaginary relative refractive index, ranging from 0.01 to $1i$. The real index is set to 1.0 for all plots. The blue dashed line corresponds to the scattering probability for incident parallel polarization and the black solid line corresponds to incident perpendicular polarization.

2.4 **Polarization Tracking Monte Carlo**

The Monte Carlo method has been used for decades to simulate physical processes through a statistical method. Work done at Los Alamos National Laboratories by scientists Nicholas Metropolis and Stenislav Ulam led to what they published as the Monte Carlo method [81]. The Monte Carlo method uses statistical probabilities to model physical processes. The method is able to accurately model the physical processes by generating a large number of repeated calculations which statistically build up to a significant and representative output. Monte Carlo simulations have increased in usage as the speed and memory of modern computers has increased. These types of simulations have been used in optics to determine photon transport in media. Traditionally, these simulations only track if the photon makes it through the medium of interest, and where the photon exits the medium spatially. For this dissertation, a Monte Carlo simulation was desired that tracked the polarization state of an incident photon throughout a specified scattering environment. One such program was designed and released for public use by Ramella-Roman *et al.* and the base code is available for download and manipulation [82]. This code was utilized and manipulated for the needs of this research. The following pages will outline the Monte Carlo program's process and follows closely with Ramella-Roman *et al.*'s published explanation. A version of the modified Monte Carlo code is attached in Appendix A.

Before delving into the details of the Monte Carlo program a few simple diagrams can clarify the process. Figure 2.13 shows the typical scattering Monte Carlo program. In the standard model the photon is launched into the medium; moved a

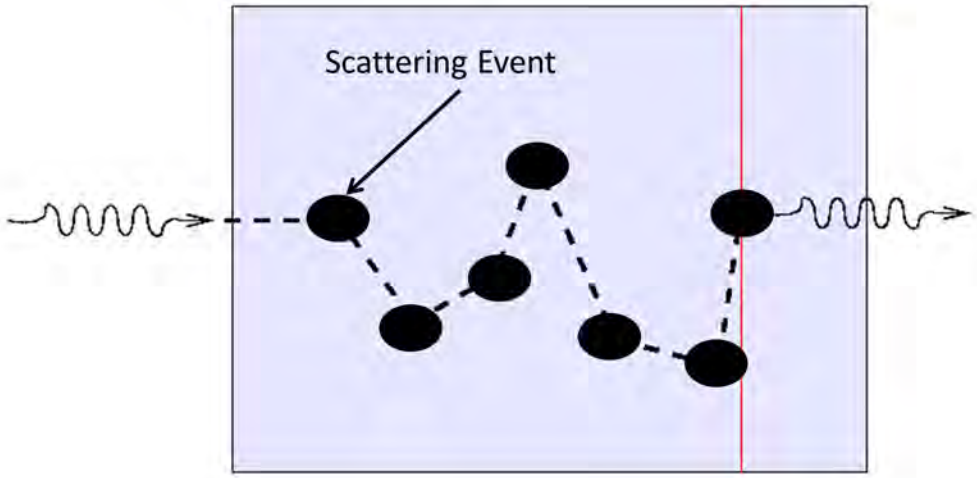

Figure 2.13: Standard Monte Carlo. The exiting photon is not restricted to set angles.

distance determined by the probability of hitting a particle; if the photon exits the front or back face of the medium it is saved to the correct bins; otherwise the photon is absorbed and killed, or scattered and a new angle and distance is determined. This process continues for all the photons that are launched.

Figure 2.14 shows the polarization tracking Monte Carlo's process. The main process of the standard Monte Carlo is used but additional steps are needed to track the polarization. The initial polarization state is defined and a reference plane must be defined. When the photon is moved and a scattering event occurs, the Stokes vector is updated via Mueller calculus with the single scattering Mueller matrix for the scattering particle. This process continues until the photon is absorbed or scattered in or out the front or back face of the medium. The resulting Stokes vector of the reflected or transmitted light is the result of the cascade of the Mueller matrix

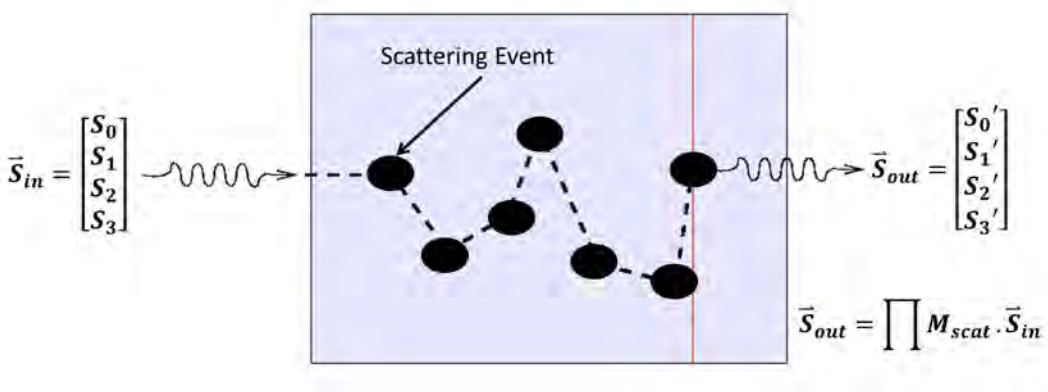

Figure 2.14: Polarization tracking Monte Carlo. The exiting photon is not restricted to set angles.

calculations.

The key to proper polarization tracking in a Monte Carlo program rests with the correct use of a reference plane. Polarized light's electric field oscillations are dependent on the location and direction of the observer, thus it is important to set a reference plane that defines how the polarization is described. There are multiple techniques that can be used to track the reference plane throughout the scattering process; for my analysis the meridian plane method first described by Chandrasekhar is used [83]. The geometry of the problem is shown in Figure 2.15 [82, 83]. The reference plane for this method is determined by the photon's initial direction, defined as a unit vector made up of direction cosines, and the z-axis. The initial and scattered directions are also defined by two angles; θ which is the angle between the photon direction and the z-axis, and ϕ which is the angle between the photon direction and the $x-z$ plane. The initial photon direction is the unit vector I_1 and the scattered photon direction is the unit vector I_2. The initial meridian

plane is defined as the plane COA in the figure. The polarization state of the photon is determined by decomposing the electric field into parallel and perpendicular components with respect to the defined meridian plane. After a scattering event, the photon direction is changed and a new meridian plane is found. The resulting scattered polarization state must then be determined based on the new meridian plane and the new parallel and perpendicular electric field components.

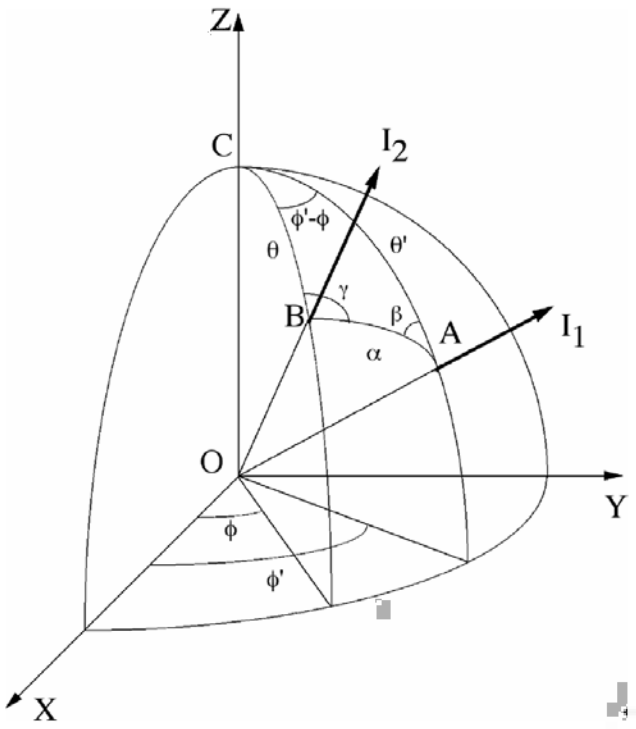

Figure 2.15: Meridian plane geometry first described by Chandrasekhar and used by Ramella-Roman *et al.* [82, 83]. The initial meridian plane is the plane COA. The initial direction is the unit vector I_1 and the scattered direction is the unit vector I_2.

Table 2.1: Monte Carlo Inputs

Input	Symbol	(units)
Particle Diameter	D	(μm)
Vacuum Wavelength	λ_0	(μm)
Particle Refractive Index	$n_p - ik_p$	
External Medium Refractive Index	$n_m - ik_m$	
Relative Refractive Index	$m = \frac{n_p - ik_p}{n_m - ik_m}$	
Particle Density	ρ	$(particles/mm^3)$
Slab Length	L	(cm)

2.4.1 Polarization Tracking Monte Carlo Method

2.4.1.1 Define Scattering Environment

Before the Monte Carlo simulation is performed the scattering environment of interest must be defined. There are various parameters that can be inputted into the simulation. A list of the Monte Carlo inputs is shown in Table 2.1. These inputs are inserted into the Monte Carlo code using a batch file system and a Matlab script.

2.4.1.2 Initialize Photon

The photons initial photon properties are set. The direction is set perpendicular to the scattering slab face. The initial photon direction is defined by the direction cosines, $[u_x, u_y, u_z] = [0, 0, 1]$, meaning the photon is launched along the z-axis. The initial meridian reference plane is defined as the $x-z$ plane. The initial polarization state of the photon is defined by the input Stokes vector. For these simulations, two polarization states where used, vertically linearly polarized ($\boldsymbol{S} = [1, 1, 0, 0]^T$) and right circularly polarized ($\boldsymbol{S} = [1, 0, 0, 1]^T$). Once the initial direction, reference

plane, and polarization state are set, the photon is ready to be launched into the slab of scattering medium.

2.4.1.3 **Launch/Move Photon**

As is used in a standard Monte Carlo program, the photon is moved based off of a pseudo random number. The distance that the photon is moved is defined as,

$$\Delta s = -\frac{ln(\zeta)}{\mu_{ext}}, \tag{2.52}$$

where ζ is a pseudo random number in the interval (0, 1], and μ_{ext}, the extinction coefficient, is equal to $\mu_a + \mu_s$, which is the sum of the absorption coefficient and the scattering coefficient of the medium. The extinction coefficient is defined from Beer's Law, shown in Equation 2.53 and determines how quickly light is absorbed or scattered in a given distance.

$$I = I_0 e^{-\mu_{ext} z} \tag{2.53}$$

The absorption coefficient is determined from the imaginary refractive index of the scattering medium [84].

$$\mu_a = \frac{4\pi k_m}{\lambda} \tag{2.54}$$

The scattering coefficient is defined by the number density of the scattering particles and the scattering cross-section of a single scattering particle. The scattering cross-section is determined from Mie Theory where k is the wave number and a_n

and b_n are described in Equations 2.43 and 2.44.

$$\sigma_{sca} = \frac{2\pi}{k^2} \sum_{n=1}^{\infty} (2n+1)(|a_n|^2 + |b_n|^2) \tag{2.55}$$

The scattering coefficient is thus,

$$\mu_s = \rho \sigma_{sca}. \tag{2.56}$$

The direction of the photon is determined by the unit vector I, made up of direction cosines. Following the process described by Witt [85], $u_x = \boldsymbol{I} \cdot \hat{x}$, $u_y = \boldsymbol{I} \cdot \hat{y}$, $u_z = \boldsymbol{I} \cdot \hat{z}$, where the hatted x, y, and z are the unit vectors in the global reference frame. The new photon position after being moved/launched is defined as x', y', and z'. The new spatial locations are determined from the equations below.

$$x' = x + u_x \Delta s = I_x \Delta s \tag{2.57}$$

$$y' = y + u_y \Delta s = I_y \Delta s \tag{2.58}$$

$$z' = z + u_z \Delta s = I_z \Delta s \tag{2.59}$$

2.4.1.4 **Drop/Absorption of the Photon**

After the photon is moved and it is determined to still be in the slab of medium, it is determined if the photon has been absorbed. A weight factor is assigned to the photon and is tracked with the photon throughout the Monte Carlo simulation. The weight, W, is initially set to a value of 1 and is then updated after each movement

of the photon based on the absorption of the medium. The medium's albedo is used to determine the effect on the weight factor. The *albedo* is the fractional probability of being scattered and therefore $1 - albedo$ is the probability to be absorbed.

$$albedo = \frac{\mu_s}{\mu_s + \mu_a} \tag{2.60}$$

The weight factor is equal to $(albedo)^n$ after n movements through the medium. When the weight factor drops below a threshold value the photon is considered absorbed by the medium and it is killed/dropped from the simulation. The typical threshold value used is 0.001.

2.4.1.5 **Scattering of the Photon**

After the photon is moved and not absorbed, it encounters a scattering event. The process of correctly determining the scattering angle and change in polarization state is a multifaceted problem which will be explained in the following subsections. The initial polarization state is defined by the meridian plane and the parallel and perpendicular components of the electric field.

Rejection Method - Determining the scattering and rotation angles

The scattering angle, α, and the rotation angle to get into the scattering plane, ψ, are determined from the phase function of the scattering particles and a rejection method. The phase function depends on both angles α and ψ, and the incident Stokes vector $\boldsymbol{S}_0 = [I_0, Q_0, U_0, V_0]^T$. The phase function is,

$$P(\alpha, \psi) = s_{11}(\alpha) I_0 + s_{12}(\alpha)[Q_0 cos(2\psi) + U_0 sin(2\psi)], \tag{2.61}$$

where the s terms are from the single scattering Mueller matrix determined by Mie Theory [79]. The rejection method is used to generate random variables which have a specific desired distribution [23, 82]. The two angular values are desired; therefore three random numbers are needed. First, a uniformly distributed random value between 0 and 1 is assigned as a temporary phase function value, P_{rand}. Second, a uniformly distributed random scattering angle between 0 and π is generated, α_{rand}. Lastly, a random rotation angle is generated between 0 and 2π from a uniform distribution, ψ_{rand}. The rejection method checks if $P_{rand} \leq P(\alpha_{rand}, \psi_{rand})$; the random angles are used if true, otherwise they are rejected. If the values are rejected a new set of random variables is generated and the process repeats until the inequality is satisfied. Once satisfied, the angles needed to complete the scattering process are determined.

Rotation to the scattering reference plane

Using the angles α and ψ, the Stokes vector is rotated into the scattering plane. The scattering plane is the plane ABO in Figure 2.15. The plane is made up of the original photon direction location, the origin, and the new scattered direction location. In order to utilize the single scattering Mueller matrix, the polarization must be in this specific reference plane. A rotation matrix is used to rotate the initial Stokes vector into the new reference plane.

$$R(\psi) = \begin{bmatrix} 1 & 0 & 0 & 0 \\ 0 & cos(2\psi) & sin(2\psi) & 0 \\ 0 & -sin(2\psi) & cos(2\psi) & 0 \\ 0 & 0 & 0 & 1 \end{bmatrix} \tag{2.62}$$

Scattering in the scattering plane

The photon is in the scattering reference plane; therefore, the single scattering Mueller matrix can be used to determine the change in the polarization state. Using Mueller calculus, the initial Stokes vector is multiplied with the scattering Mueller matrix for the scattering angle α. The new direction is then determined based off the initial direction cosines and the angles α and ψ. The new direction cosines are notated as $\hat{u}$.

If the photon is traveling along the z-axis and the direction cosines are (0, 0, 1) then the new direction cosines are $(sin(\alpha)cos(\psi), sin(\alpha)sin(2\psi), cos(\psi)u_z)$. Otherwise, the new scattered direction cosines are as follows.

$$\hat{u}_x = \frac{1}{\sqrt{1-u_z^2}} sin(\alpha)[u_x u_y cos(\psi) - u_y sin(\psi)] + u_x cos(\alpha) \tag{2.63}$$

$$\hat{u}_y = \frac{1}{\sqrt{1-u_z^2}} sin(\alpha)[u_x u_z cos(\psi) - u_x sin(\psi)] + u_y cos(\alpha) \tag{2.64}$$

$$\hat{u}_z = \sqrt{1-u_z^2} sin(\alpha)[u_y u_z cos(\psi) - u_x sin(\psi)] + u_z cos(\alpha) \tag{2.65}$$

At this point the new polarization state and direction are determined but one more rotation must take place in order to return the polarization to the correct meridian plane.

Return to Meridian Plane

Finally, the Stokes vector is rotated by another rotation matrix to bring the polarization state into the correct meridian plane. The meridian plane is defined as the COB plane in Figure 2.15. The rotation matrix is the same as the previous rotation matrix but with a different angle of rotation. The rotation angle is calculated based

on the work of Hovenier [86]. The rotation angle, γ, is determined from Equation 2.66, where the positive denominator is used when $\pi < \psi < 2\pi$ and the negative is used when $0 < \psi < \pi$.

$$cos(\gamma) = \frac{-u_z + \hat{u}_z cos(\alpha)}{\pm\sqrt{(1 - cos^2(\alpha))(1 - \hat{u}_z^2)}} \tag{2.66}$$

The resulting Stokes vector after the scattering process can be shown as a multiplication in Mueller calculus.

$$\boldsymbol{S_{scat}} = \boldsymbol{R}(-\gamma)\boldsymbol{M}(\alpha)\boldsymbol{R}(\psi)\boldsymbol{S_{init}} \tag{2.67}$$

2.4.1.6 Exiting the Boundary Surface

After a number of scattering events that will depend on the medium, the photon will exit the front or back face of the slab of medium; unless it has been completely absorbed in which case it was killed before this could occur. If there was absorption in the medium but the photon still exits the medium, the Stokes vector is scaled by the weight factor.

$$\begin{bmatrix} I_{out} \\ Q_{out} \\ U_{out} \\ V_{out} \end{bmatrix} = \begin{bmatrix} I_{exit}W \\ Q_{exit}W \\ U_{exit}W \\ V_{exit}W \end{bmatrix} \tag{2.68}$$

Lastly, the photon must be rotated one last time in order to set the polarization state in the reference plane of a global detector. For backscattered or reflected photons, those photons which exit out the front face of the medium reflecting back toward

the initial propagation location, the rotation is done with a rotation matrix and an angle of,

$$\xi = tan^{-1}(\frac{u_y}{u_x}). \tag{2.69}$$

Otherwise, if the photon is scattered through the back face of the medium, transmitted, then the angle of rotation is,

$$\xi = -tan^{-1}(\frac{u_y}{u_x}). \tag{2.70}$$

Since this is a Monte Carlo simulation, a large number of photons will be simulated in the scattering medium. The resulting Stokes vector for the reflected and transmitted light is given by the summation of all the photons' Stokes vector components once they are all in the correct reference frame. This is shown in the following equations where n is the number of photons collected.

$$\begin{bmatrix} I_{total} \\ Q_{total} \\ U_{total} \\ V_{total} \end{bmatrix} = \begin{bmatrix} \sum_n I_{photon} \\ \sum_n Q_{photon} \\ \sum_n U_{photon} \\ \sum_n V_{photon} \end{bmatrix} = \begin{bmatrix} S_0 \\ S_1 \\ S_2 \\ S_3 \end{bmatrix}_{total} \tag{2.71}$$

A similar calculation is performed for the DoP.

$$DoP_{total} = \frac{\sqrt{(\sum_n Q_{photon})^2 + (\sum_n U_{photon})^2 + (\sum_n V_{photon})^2}}{\sum_n I_{photon}} \tag{2.72}$$

2.4.2 **Polarization Tracking Monte Carlo Outputs**

Once a full simulation is completed there are a number of outputs that are saved and available for analysis. Depending on the simulation setup, the first set of outputs is a collection of information for each photon that exits the back or front face of the slab of medium. A .dat file is created for each polarization state for reflected and transmitted photons. Four .dat files are created for each simulation: CircularReflectionOutput.dat, CircularTransmissionOutput.dat, LinearReflectionOutput.dat, and LinearTransmissionOutput.dat. The .dat file contains the following: the photon number; the x, y, and z position after the photon has exited the slab of medium; the x, y, and z position of the last scattering event before exiting the slab; the radial location of the last scattering event; and the Stokes parameter values of the photon after exiting the medium.

The second output from the simulation is a text file. An example of the text file output is shown below.

```
gcc -lm array.c complex.c mie.c nrutil.c tmp.c -o iquv
Polarized Monte Carlo
dia=0.10000;
mus=0.94163037;
g=0.10321598;
rho=0.91000000;
lambda=0.54350;
n_p=1.597;
k_p=0.000;
n_m=1.333;
k_m=0.000;
slabsize=3.000;
optdepth=2.82489;
Qext=0.01317;
Qsca=0.01317;
Qback=0.01507;
x=0.77051;
```

```
launch V
R= 0.57560600  -0.25433477  0.00063930  -0.00000032
T= 0.42439400  -0.18496608  -0.00029407  -0.00000009
launch R
R= 0.57612000  0.00048124  0.00049068  -0.17486243
T= 0.42388000  -0.00048996  -0.00009551  0.14277213
Elapsed Time = 68.99 seconds
```

Before defining all the outputs from the text file a few parameters need to be defined. The previously described Mie Theory can be utilized to determine the scattering and extinction cross sections of a scattering particle in a medium. The scattering and extinction cross sections are the effective cross sections that radiation sees when it interacts with the particle. The geometrical cross section of a particle is fixed, while that particle's scattering and extinction cross sections vary with the size of the particle and the wavelength of the radiation. The scattering cross section was previously defined. From Mie Theory the extinction cross section is defined as,

$$\sigma_{ext} = \frac{2\pi}{k^2} \sum_{n=1}^{\infty} (2n+1) Re\{a_n + b_n\}. \tag{2.73}$$

Lastly, the absorption cross section is the difference of the extinction cross section and the scattering cross section, $\sigma_{abs} = \sigma_{ext} - \sigma_{sca}$. All of the cross sections have units similar to the geometrical cross section, cm^2 [79].

The following paragraph explains in detail the text file output. The first two rows of the text file lists the files used to run the program and the title. The following fifteen rows identify the parameters of the slab of scattering medium. The term `dia` is the diameter of the scattering particle in the medium. The term `mus` is the scattering coefficient of the scattering medium. The scattering coefficient is defined

as,

$$\mu_s = \sigma_{sca}\rho, \tag{2.74}$$

where ρ is the volume particle density and also corresponds to the term `rho` and is in units of μm^{-3}. Similarly, the absorption coeffecient of the medium is defined as,

$$\mu_a = \sigma_{abs}\rho. \tag{2.75}$$

The units for the scattering and absorption coefficients are cm^{-1}.

The term `g` is called the asymmetry parameter defined as,

$$g = \langle cos(\theta) \rangle = \int_{4\pi} (|s_1(\theta)|^2 + |s_2(\theta)|^2) cos(\theta) d\Omega, \tag{2.76}$$

where $s_1(\theta)$ and $s_2(\theta)$ are the amplitude scattering functions previously described. If the particle scatters light isotropically, or if the scattering is symmetric about the scattering angle of 90 degrees, then $g = 0$. If the particle scatters light in the forward direction ($\theta = 0°$) g is positive; otherwise if the particle scatters light in the backward direction ($\theta = 180°$) then g is negative.

The term `lambda` is the vacuum wavelength in units of microns. The terms `n_p` and `n_m` are the real refractive indices of the particle and the medium. Similarly, the terms `k_p` and `k_m` are the imaginary refractive indices of the particle and medium.

The `slabsize` is the length of the slab of medium in units of cm's. The length is in the z direction and determines at what z location a photon is considered exiting the forward direction. The `optdepth` term is the optical thickness, or depth, of the

slab. The optical thickness is a dimensionless term that allows for evaluation of various scattering and absorption environments with different sized particles. The optical thickness is defined as,

$$\tau = \rho\sigma_{ext}L = (\mu_s + \mu_a)L, \tag{2.77}$$

where L is the `slabsize` and the other terms are those previously defined.

The terms `Qext`, `Qsca`, `Qback` are all efficiencies or efficiency factors for extinction, scattering, and back scattering. The efficiency factors are defined as,

$$Q_{ext} = \frac{\sigma_{ext}}{\pi r^2}, \tag{2.78}$$

$$Q_{sca} = \frac{\sigma_{sca}}{\pi r^2}, \tag{2.79}$$

$$Q_{back} = \frac{\sigma_{back}}{\pi r^2} = \frac{1}{x^2}|\sum_n (2n+1)(-1)^n(a_n - b_n)|^2. \tag{2.80}$$

The last of the terms defining the slab of medium and the scattering particles is `x` which is the size parameter, previously defined. For reference, size parameters for scattering environments of smoke and fog at infrared wavelengths is shown in Table 2.2.

After defining the terms of the scattering environment, the outputs of the full Monte Carlo simulation are shown in the text file. The first set of outputs follow the `Launch V` indicating that the results are for vertically polarized light input. There are two rows with four numerical values. The rows are label `R=` and `T=`, which respectively correspond to the reflected and transmitted photons. The four

numerical values for the two rows are the four Stokes vector parameters in order from S_0 to S_3. Thus, the output is in the format: `R=` S_0 S_1 S_2 S_3, and similarly for `T=`. The outputs for circularly polarized light input are shown in the rows following `Launch R`. Lastly, the total computation time for the Monte Carlo simulation is given in seconds following the `Elapsed Time` term.

The Monte Carlo results presented in this dissertation are all derived from these outputs.

Table 2.2: Size parameters for scattering environments of smoke and fog at infrared wavelengths. Smoke's size parameters correspond to the gray cells, radiation fog size parameters correspond to the light blue cells, similarly advection fog corresponds to the dark blue cells, and the medium blue cells are size parameters that exist for both radiation fog and advection fog.

		Wavelength (μm)									
		SWIR			MWIR			LWIR			
		1	2	3	4	5	8	9	10	11	12
Particle Diameter (μm)	1	3.14	1.57	1.05	0.79	0.63	0.39	0.35	0.31	0.29	0.26
	2	6.28	3.14	2.09	1.57	1.26	0.79	0.70	0.63	0.57	0.52
	3	9.42	4.71	3.14	2.36	1.88	1.18	1.05	0.94	0.86	0.79
	4	12.57	6.28	4.19	3.14	2.51	1.57	1.40	1.26	1.14	1.05
	5	15.71	7.85	5.24	3.93	3.14	1.96	1.75	1.57	1.43	1.31
	6	18.85	9.42	6.28	4.71	3.77	2.36	2.09	1.88	1.71	1.57
	7	21.99	11.00	7.33	5.50	4.40	2.75	2.44	2.20	2.00	1.83
	8	25.13	12.57	8.38	6.28	5.03	3.14	2.79	2.51	2.28	2.09
	9	28.27	14.14	9.42	7.07	5.65	3.53	3.14	2.83	2.57	2.36
	10	31.42	15.71	10.47	7.85	6.28	3.93	3.49	3.14	2.86	2.62
	11	34.56	17.28	11.52	8.64	6.91	4.32	3.84	3.46	3.14	2.88
	12	37.70	18.85	12.57	9.42	7.54	4.71	4.19	3.77	3.43	3.14
	13	40.84	20.42	13.61	10.21	8.17	5.11	4.54	4.08	3.71	3.40
	14	43.98	21.99	14.66	11.00	8.80	5.50	4.89	4.40	4.00	3.67
	15	47.12	23.56	15.71	11.78	9.42	5.89	5.24	4.71	4.28	3.93
	16	50.27	25.13	16.76	12.57	10.05	6.28	5.59	5.03	4.57	4.19
	17	53.41	26.70	17.80	13.35	10.68	6.68	5.93	5.34	4.86	4.45
	18	56.55	28.27	18.85	14.14	11.31	7.07	6.28	5.65	5.14	4.71
	19	59.69	29.85	19.90	14.92	11.94	7.46	6.63	5.97	5.43	4.97
	20	62.83	31.42	20.94	15.71	12.57	7.85	6.98	6.28	5.71	5.24
	21	65.97	32.99	21.99	16.49	13.19	8.25	7.33	6.60	6.00	5.50
	22	69.12	34.56	23.04	17.28	13.82	8.64	7.68	6.91	6.28	5.76
	23	72.26	36.13	24.09	18.06	14.45	9.03	8.03	7.23	6.57	6.02
	24	75.40	37.70	25.13	18.85	15.08	9.42	8.38	7.54	6.85	6.28
	25	78.54	39.27	26.18	19.63	15.71	9.82	8.73	7.85	7.14	6.54
	26	81.68	40.84	27.23	20.42	16.34	10.21	9.08	8.17	7.43	6.81
	27	84.82	42.41	28.27	21.21	16.96	10.60	9.42	8.48	7.71	7.07
	28	87.96	43.98	29.32	21.99	17.59	11.00	9.77	8.80	8.00	7.33
	29	91.11	45.55	30.37	22.78	18.22	11.39	10.12	9.11	8.28	7.59
	30	94.25	47.12	31.42	23.56	18.85	11.78	10.47	9.42	8.57	7.85

CHAPTER 3

Detection Range Enhancement Using Circularly Polarized Light in Scattering Environments for Infrared Wavelengths

3.1 Introduction

This chapter includes original research published in a conference proceedings and a journal article [87, 88]. The focus of this chapter will be on the transmission results presented in the journal article, but reflection results are also shown and are consistent with the transmission results.

Polarized light propagation in scattering environments has been of recent interest, where polarization sensing techniques increase range and contrast in these environments. Polarization offers an added variable to a sensing system that can be manipulated, to better discriminate a target from a scene and to extent range in scattering environments. Previous research often has developed simulations and experiments utilizing polystyrene microspheres, milk, or tissue phantoms in water as the scattering environment of interest. Chapter 1 of this dissertation covers a wide range of the previously published works. Most of these previously published works are limited in wavelength, polarization, and the majority are for underwater scattering environments. In contrast, this simulation research identifies broad wavelength ranges that demonstrate circular polarization's superiority in particle size and refractive index parameter sets that realistically model fog and dust in the

atmosphere. There are also limited experimental and simulation results for laboratory and outdoor fog which were also presented in Chapter 1. These previous works are limited in illuminating wavelengths and particle sizes. The following simulation results remain unique in that they involve broad wavelength ranges and identify circular polarization's role in realistic environments, through particle size and refractive index parameter ranges.

To date, no research has simulated or experimentally shown circular polarization's persistence benefits over broad wavelength ranges and over broad sensing environments. The majority of currently available experimental and simulation results, characterizing circular polarization, is limited to select wavelengths, typically in the visible spectrum, and utilizes underwater scenes with varying concentrations of polystyrene microspheres, milk, or tissue phantoms as scattering objects. This work quantifies a broad wavelength response through infrared wavelength ranges in multiple scattering environments where circular polarization sensing outperforms linear polarization.

Using polarization-tracking Monte Carlo simulations, I model particle sizes and refractive indices representative of fog and dust at infrared wavelengths where circular polarization persists in the intended polarization at larger optical thicknesses than linear polarization. The increased persistence of circularly polarized light versus linear is shown for reflection and transmission through environments of fog and dust. The persistence of circular polarization in scattering environments can be exploited to improve sensing and imaging range in scattering environments, important to many critical applications.

This chapter is organized as follows: Section 3.2 covers the background of this work, including validation of the Monte Carlo simulation's performance against previously published work, Section 3.3 describes the environments of interest and the parameters used for each set of simulations, Section 3.4 presents the transmission and reflection results for each of the environments of interest for wavelengths ranging from 0.9 to 12 microns (encompassing short-wave infrared, SWIR, mid-wave infrared, MWIR, and long-wave infrared, LWIR) for fog and 2.5 to 12 microns (encompassing MWIR and LWIR) for dust, and Section 3.5 concludes showing circular polarization persists better than linear polarization for certain scattering environments in all of earth's atmospheric infrared transmissible regions: SWIR (0.9 – 2.5 microns), MWIR (3 – 5 microns), and LWIR (8 – 12 microns).

3.2 Background

Traditionally, when sensing in scattering environments, the use of longer wavelengths (over visible wavelengths) is preferred due to the decrease of the scattering cross-section of the particles with increased wavelength [79]. The longer wavelengths increase the number of particles that are considered in the Rayleigh scattering regime where scattering is isotropic. As a result, infrared wavelengths are considered superior to visible wavelengths in scattering environments of smaller particle sizes and smaller optical thicknesses. For highly scattering environments with large optical thicknesses all wavelengths are detrimentally affected [89]. In order to accurately sense targets in these challenging environments, all discriminating optical parameters should be utilized. One such optical parameter, beyond the intensity and

wavelength of light, is its polarization.

The physics of polarization are explained in Chapter 2. The key for this chapter is the DoP defined in Equation 2.4. In highly scattering environments, photons are multiply scattered and, as a result, their polarization is modified. Individual photons polarization states are randomized through the scattering process and the resulting transmitted polarization state is subsequently depolarized.

The goal in this work is to investigate where circularly polarized light's persistence in highly scattering environments of real world interest is superior to linearly polarized light. To this end, I use a polarization tracking Monte Carlo program to investigate circularly polarized light's performance. The process of the Monte Carlo program is explained in Chapter 2 Section 2.4. For each simulation, one million photons of each polarization state were propagated into the slab of scattering medium, orthogonal to the back face of the slab. If the photons exit the front face of the slab they are considered transmitted photons, if the photons exits the back face of the slab they are considered reflected or backscattered photons. For each simulation, a set of inputs are selected; the inputs were defined in Chapter 2 in Table 2.1. These inputs also give the overall optical thickness of the slab of scattering particles for each simulation configuration. The equation for the optical thickness is defined in Chapter 2 in Equation 2.77.

I utilized published numbers in order to verify my Monte Carlo simulation's output. Ishimaru *et al.* performed simulations looking at circular and linear polarizations transmitted DoP versus optical thickness for a specific scattering environment [30]. The environment of interest was 1.05 micron diameter latex spheres in

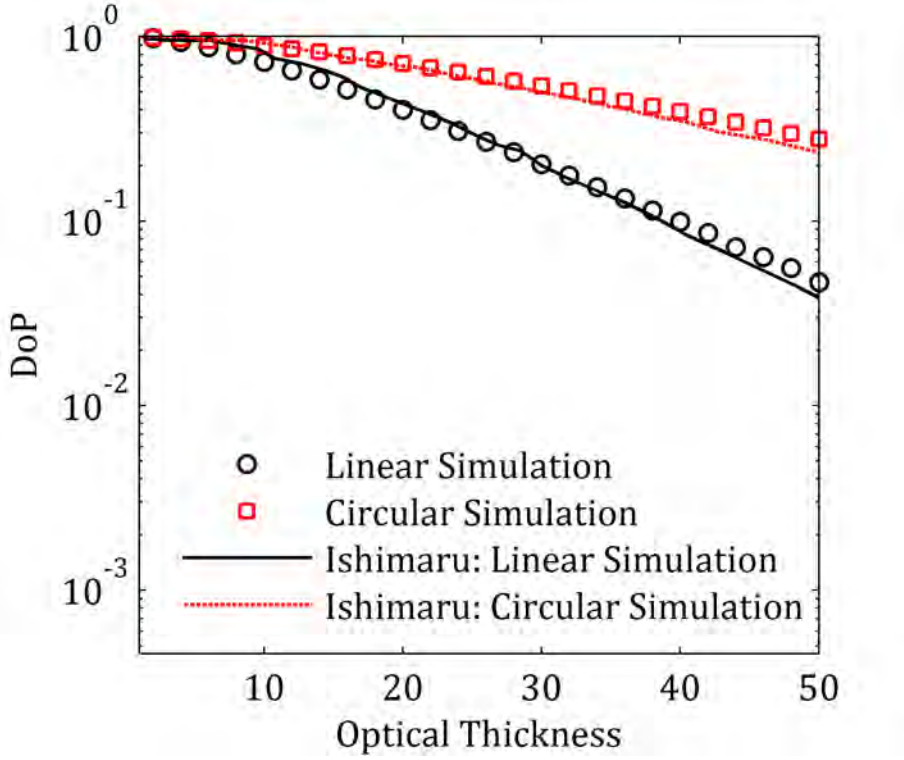

Figure 3.1: Ishimaru's simulated transmission results (solid black curve and dashed red curve) [30] versus my confirming simulated transmission results (black circles and red squares) for 1.05 micron diameter latex spherical particles in water with an illumination wavelength of 0.53 microns.

water with an illumination wavelength of 0.53 microns. I performed similar simulations with my Monte Carlo program and I see confirmation with Ishimaru's results. Figure 3.1 shows Ishimaru's results as a solid curve and a dotted curve with my corresponding simulation results shown with circles and squares.

Before moving on to the environments of interest and my results I must define one more useful quantity. Throughout the analysis I am specifically interested in the performance difference between circular and linear incident polarization states on the slab of scattering medium. To clearly determine where circularly polarized light

outperforms linearly polarized light a difference quantity is defined. The quantity, DoP_{diff}, is defined as the difference between the resulting transmitted or reflected DoP when circularly polarized light is incident versus when linearly polarized light is incident,

$$DoP_{diff} = DoP_{circular} - DoP_{linear}. \tag{3.1}$$

When circularly polarized light transmits or reflects with a higher DoP than linearly polarized light this quantity is positive. This quantity is negative when linearly polarized light transmits or reflects with a larger DoP. I note that the circularly polarized light persistence is generally a larger effect and over broader wavelength ranges than that of linearly polarized input. For this reason, it is of particular interest when the DoP_{diff} is positive and circularly polarized light maintains its DoP better than linearly polarized light, persisting superiorly through transmission or reflection.

3.3 **Environments**

Four realistic scattering environments were simulated: two types of fog (radiation and advection) and two types of Sahara dust (small and large). Three particle diameters were chosen from the particle size range for each environment. The particle sizes were chosen to coincide with small, large, and mean diameter sizes from the environments particle diameter distribution. All simulations were run with monodisperse particle diameters, so this is not varying within a single run, in order to clearly isolate dependencies in performance across a wide wavelength range due to a single particle size. Simulating a size distribution will likely broaden responses

as a function of wavelength, and is reserved for future work. All simulations were performed at an optical thickness (Equation 2.77), $\tau = \rho\sigma_{ext}L$, of 5.

3.3.1 **Radiation Fog**

Radiation fog is the first environment simulated. Radiation fog is typically found near the ground, sometimes called ground fog, and arises when the earth cools thermally after the sun sets. The typical model for radiation fog consist of water particles with diameters smaller than 10 microns [53, 90, 91]. In order to simulate the range of particle sizes, three particle diameters were chosen: 1, 4, and 10 micron diameters.

3.3.2 **Advection Fog**

Advection fog was the second fog simulated. Advection fog is typically found near coastlines and marine environments. When wind moves water-dense air over colder surfaces, such as warm air traveling over cool waters, the air is cooled and advection fog is produced. Typical models of advection fog consist of larger particle sizes compared to radiation fog [91]. For my purposes I model advection fog as three particles diameters, 10, 20, and 40 microns. For both radiation and advection fog the index values for water were taken from data measured and collected by Segelstein [92]. The real and imaginary refractive indices for water from Segelstein are plotted in Figure 3.2.

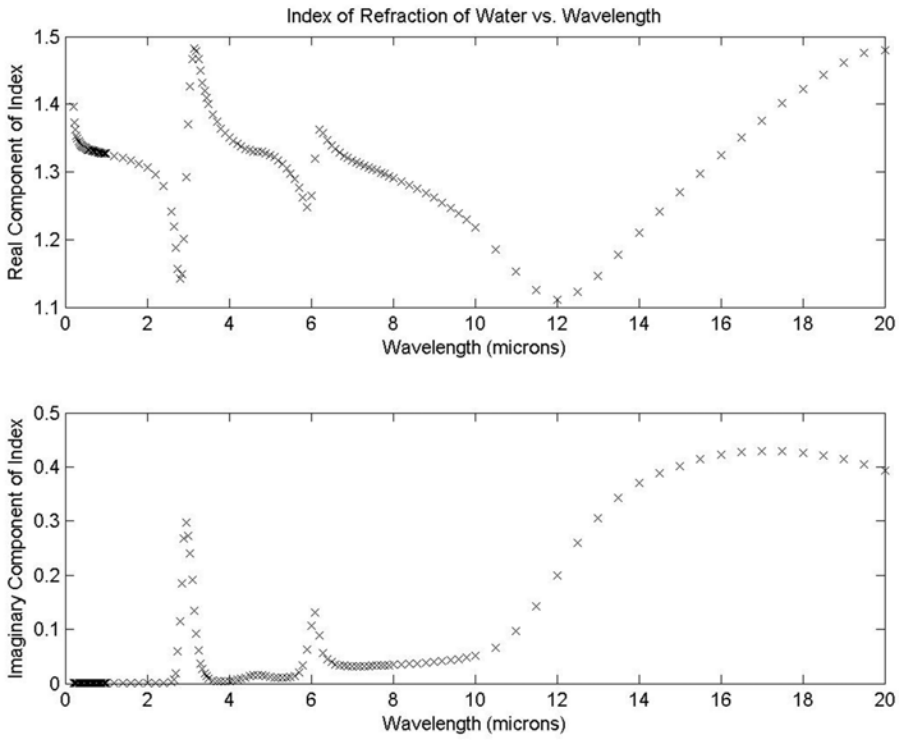

Figure 3.2: Real and imaginary refractive indices for water from Segelstein [92].

3.3.3 **Small Particle Sahara Dust**

The final two environments simulated were Sahara dust. The two different models illustrate small and large particles. The small particle Sahara dust sizes characterize dust that is typically suspended in various altitudes in the atmosphere. These small particle sizes are easily sent airborne and remain in the atmosphere for large distances. The diameters used for the small particle size model were 0.1, 1.5, and 6 microns [93, 94].

3.3.4 **Large Particle Sahara Dust**

The large particle Sahara dust sizes characterize dust found nearer to earth's surface [93, 94]. For the large particle size model, particle diameters of 10, 20, and 30 microns were used. Both the small and large particle models used Sahara dust and sand index information taken from Volz *et al.* [95]. The index data from Volz *et al.* is shown in Figure 3.3.

The simulation results for Sahara dust all involve simulations of homogeneous spherical particles. The author is aware of the fact that typical dust particles can be highly non-spherical which can be relevant for the polarization state of scattered photons.

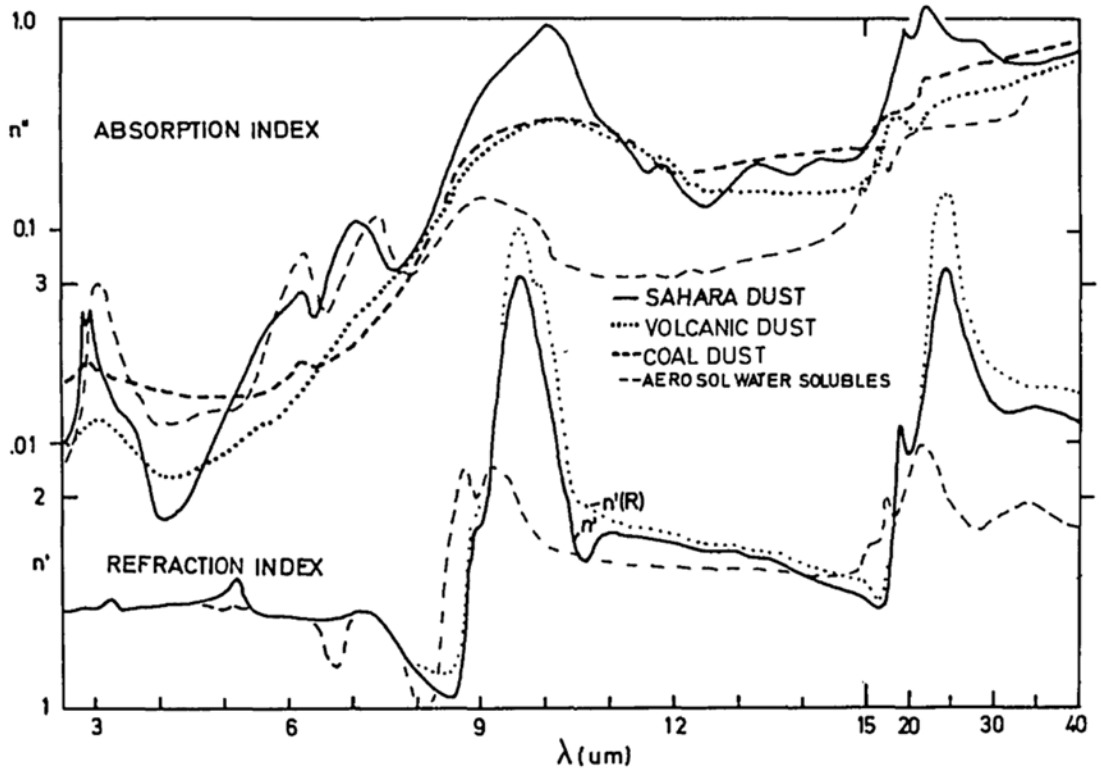

Figure 3.3: Real (n') and imaginary (n") refractive indices for Sahara dust and other particulates from Volz *et al.* [95].

3.4 Results

For each environment, one million photons of both circular and linear polarizations were launched, with normal incidence, into a slab of the specific particles. The resulting transmitted and reflected DoP was calculated and the DoP_{diff} was determined. The following figures show the DoP_{diff} versus wavelength for each environment. In order to better delineate where circularly polarized light outperforms linearly polarized light a line is plotted for a $DoP_{diff} = 0$ in the subsequent figures.

The results presented in this chapter only consider the effects of absorption and scattering due to Mie scattering. The scattering particles are randomly placed in a slab of air (complex refractive index $= 1.0 + i0.0$). The absorption of environmental gases, thermal emission of gases and particulates, as well as solar irradiance is not considered in these simulations although they can contribute significantly. Absorption by atmospheric gases such as CO_2, O_3, CH_4, and N_2O is a critical issue for signal persistence at infrared wavelengths. When these gases are present the absorption through the atmosphere at certain infrared wavelengths can rise to 100% percent even for short path lengths. Researchers that want to consider these absorption effects can simply reduce the transmitted values in each of the DoP calculations by the appropriate path length as a function of wavelength. This should not change the presented DoP_{diff} graphs except when each DoP calculation is reduced to zero.

The following results are shown for wavelengths of 0.9 to 12 microns for fog and 2.5 to 12 microns for dust. Although results are shown for all wavelengths in those ranges, there are wavelengths that are not realistically usable due to atmospheric absorption from these gases [96].

3.4.1 Radiation Fog

3.4.1.1 SWIR Wavelengths

Figures 3.4 and 3.5 show transmission and reflection results for radiation fog at SWIR wavelengths. The figures show circularly polarized light outperforms linearly polarized light for all three particle sizes for SWIR wavelengths. Circular polarization persists superiorly for the 1 micron particle through a wavelength of 1.9 microns. From a wavelength range of 1.9 – 2.5 microns, linear polarization persists superiorly for the 1 micron particle. The results for the 4 micron particle show some oscillation in the smaller wavelengths, but throughout the entire SWIR region circular polarization outperforms linear polarization. The 10 micron particle results show a preference for circular polarization throughout the SWIR region but this particle size shows a large amount of oscillatory behavior. At roughly a wavelength of 1.9 microns circular polarization clearly begins to persist superiorly for the 10 micron particle.

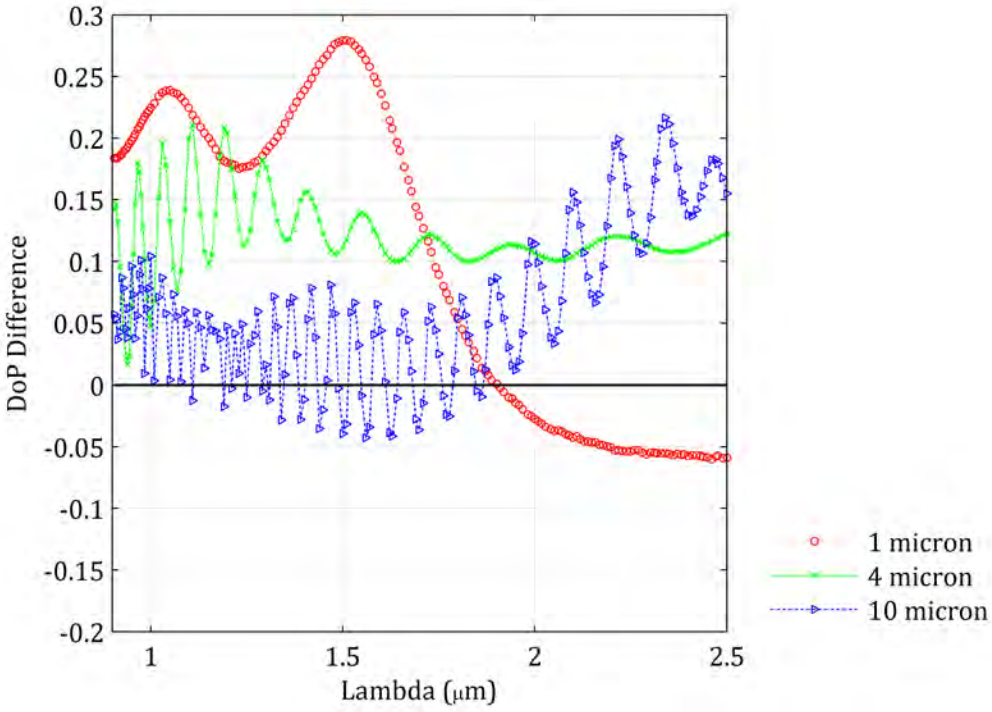

Figure 3.4: Transmission DoP_{diff} results for radiation fog for SWIR wavelengths. 1 micron particle size results shown in red (circles), 4 micron particle size results shown in green (x's), and 10 micron particle size results shown in blue (triangles). A black line for $DoP_{diff} = 0$ delineates where linear polarization performs better (negative values) and where circular polarization performs better (positive values).

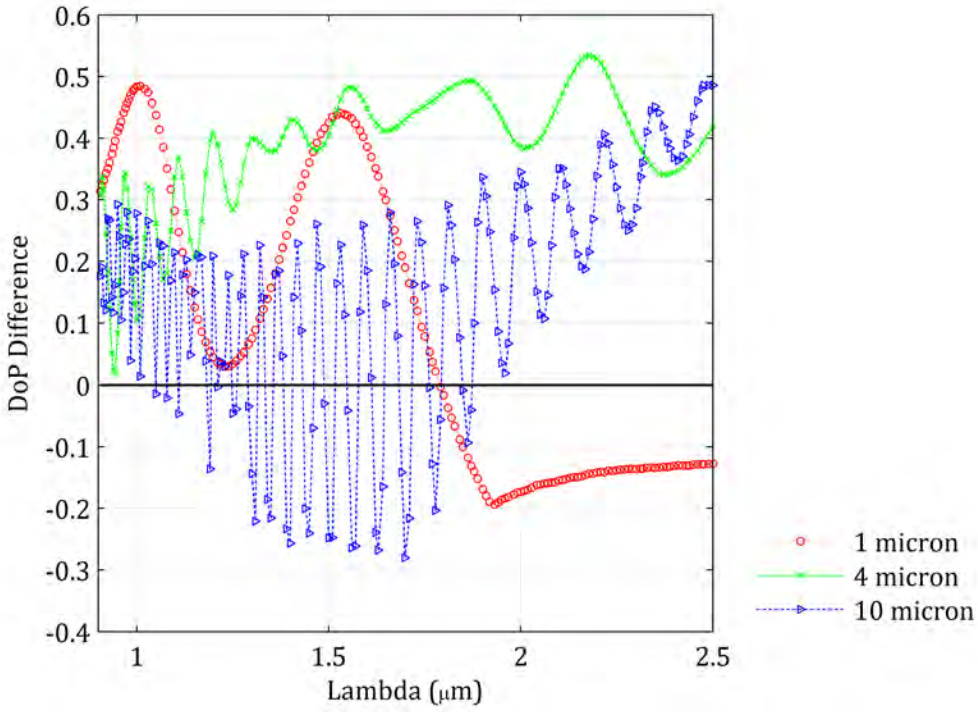

Figure 3.5: Reflection DoP_{diff} results for radiation fog for SWIR wavelengths. 1 micron particle size results shown in red (circles), 4 micron particle size results shown in green (x's), and 10 micron particle size results shown in blue (triangles). A black line for $DoP_{diff} = 0$ delineates where linear polarization performs better (negative values) and where circular polarization performs better (positive values).

3.4.1.2 **MWIR to LWIR Wavelengths**

The radiation fog results for the MWIR through the LWIR are shown in Figure 3.6 for transmission and Figure 3.7 for reflection. For both the MWIR and LWIR wavelengths, the small, 1 micron particle shows preference for linearly polarized light. At a single wavelength of roughly 3 microns all three particle sizes show a preference for linearly polarized light. The two larger particle sizes show circular polarization persisting superiorly in the MWIR. The 4 micron particle has a larger DoP_{diff}, but circular polarization is clearly beneficial in this region. For the LWIR region, only the largest, 10 micron particle size shows a persistence benefit for circularly polarized light. Linear polarization is preferred for both the 1 and 4 micron particles in the LWIR.

The simulation results show clear wavelength ranges, where circular polarization persists longer than linear polarization for radiation fog. The 1 micron particle shows circular polarization persists superiorly in the SWIR up to a wavelength of 1.9 microns. Circular polarization is superior for the 4 micron particle in the SWIR and MWIR regions. The 10 micron particle has a broad wavelength range where circular polarization persists better than linear. There are some oscillations in the lower end of the SWIR region but throughout the SWIR, MWIR, and the LWIR, circular polarization is preferred and superior for the 10 micron particle.

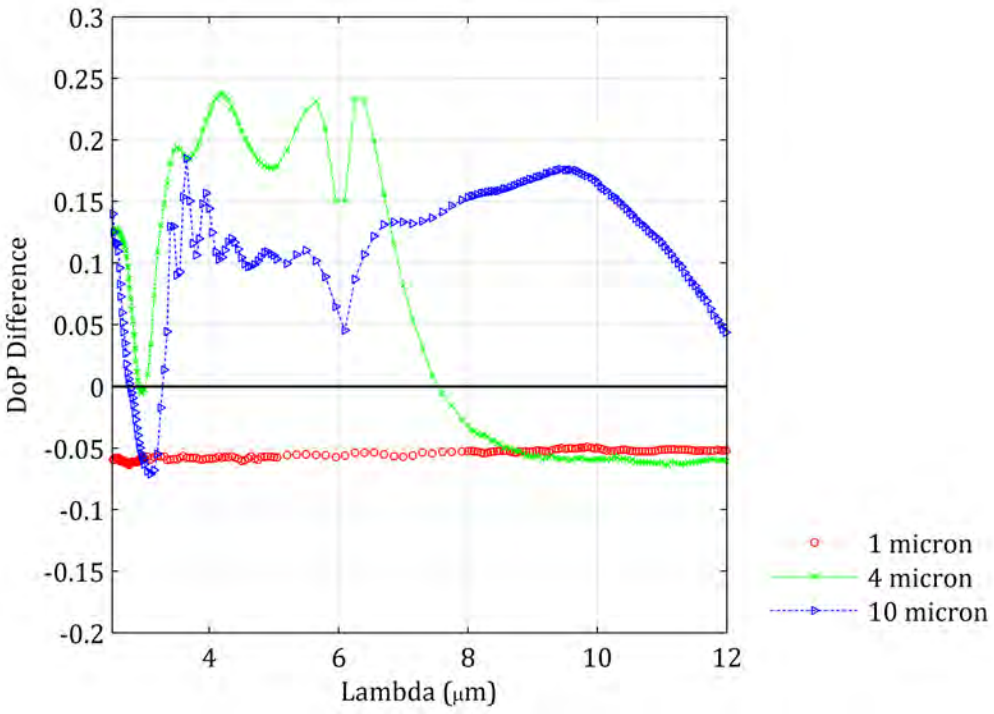

Figure 3.6: Transmission DoP_{diff} results for radiation fog for MWIR to LWIR wavelengths. 1 micron particle size results shown in red (circles), 4 micron particle size results shown in green (x's), and 10 micron particle size results shown in blue (triangles). A black line for $DoP_{diff} = 0$ delineates where linear polarization performs better (negative values) and where circular polarization performs better (positive values).

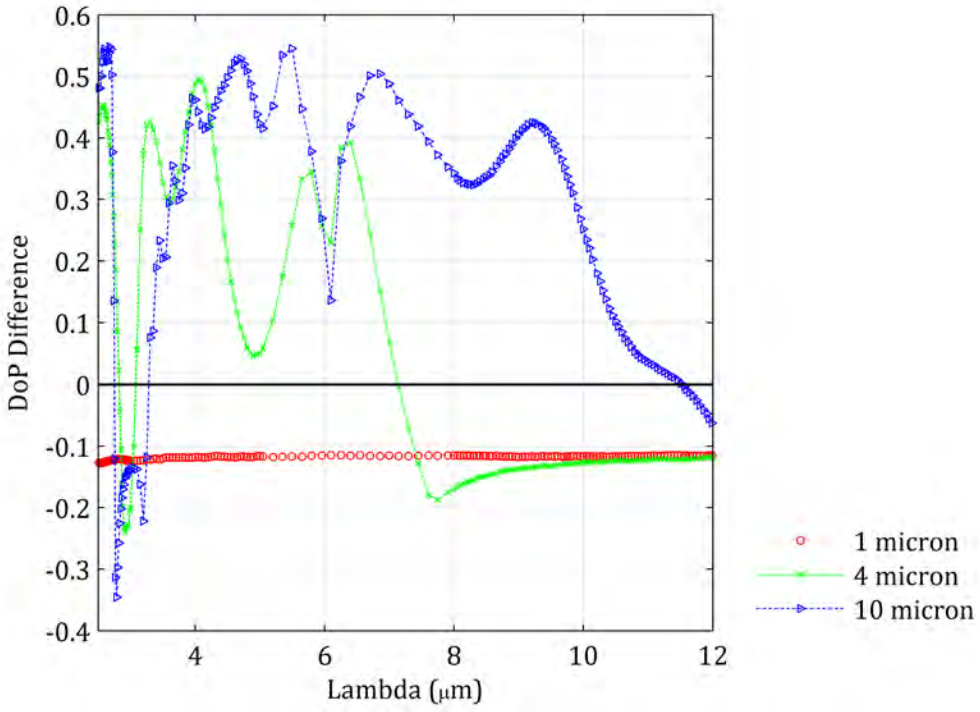

Figure 3.7: Reflection DoP_{diff} results for radiation fog for MWIR to LWIR wavelengths. 1 micron particle size results shown in red (circles), 4 micron particle size results shown in green (x's), and 10 micron particle size results shown in blue (triangles). A black line for $DoP_{diff} = 0$ delineates where linear polarization performs better (negative values) and where circular polarization performs better (positive values).

3.4.2 **Advection Fog**

Results for the advection fog simulations are shown in the following figures. Fewer data points were generated for each particle diameter for the advection results due to increased computation time for the larger particle sizes. For comparison, the 10 micron results for advection fog are the exact same as those for radiation fog, since the index and size is the same. The additional points available in the radiation results are omitted for congruency with the other sets of data in order to maintain the same number of data points and to clarify the plots. The spectral resolution on the advection fog plots are thus lower than the radiation fog plots, but the general patterns can still be observed.

3.4.2.1 **SWIR Wavelengths**

The SWIR results are shown in Figure 3.8 for transmission and Figure 3.9 for reflection. Similar to the radiation fog results, the 10 micron particle shows oscillations in the lower end of SWIR region but is generally positive for circular polarization. The 20 and 40 micron particles show a preference for circular polarization throughout the SWIR region. Due to the lower sample size and spectral resolution, it is difficult to determine with certainty whether the larger particles maintain their circular polarization persistence benefit uniformly or if the oscillations are merely sampled out.

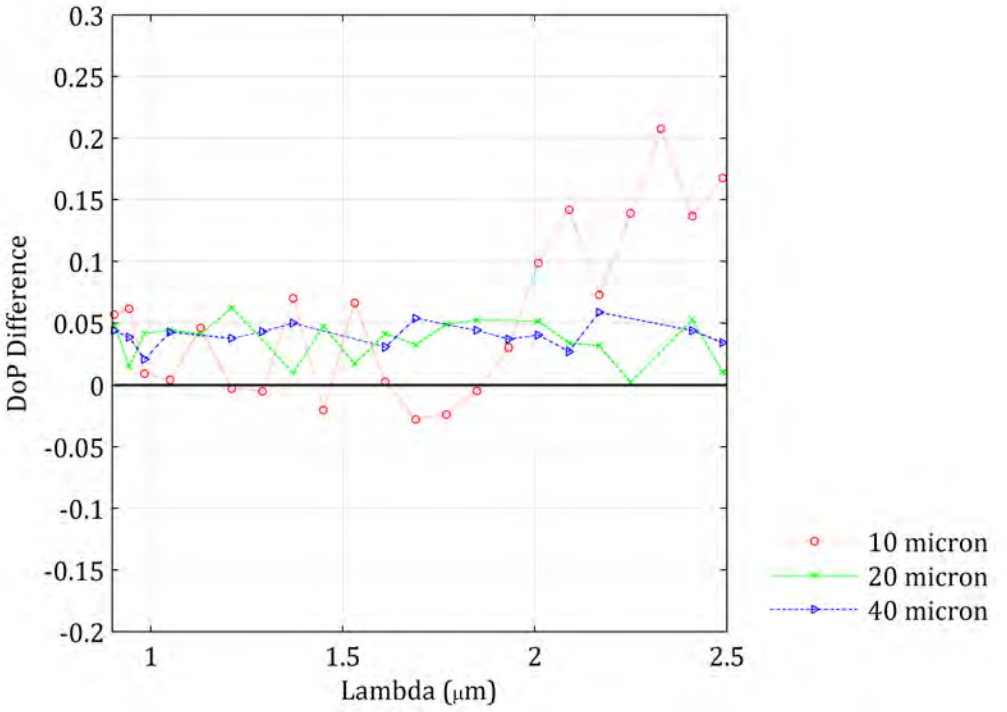

Figure 3.8: Transmission DoP_{diff} results for advection fog for SWIR wavelengths. 10 micron particle size results shown in red (circles), 20 micron particle size results shown in green (x's), and 40 micron particle size results shown in blue (triangles). A black line for $DoP_{diff} = 0$ delineates where linear polarization performs better (negative values) and where circular polarization performs better (positive values).

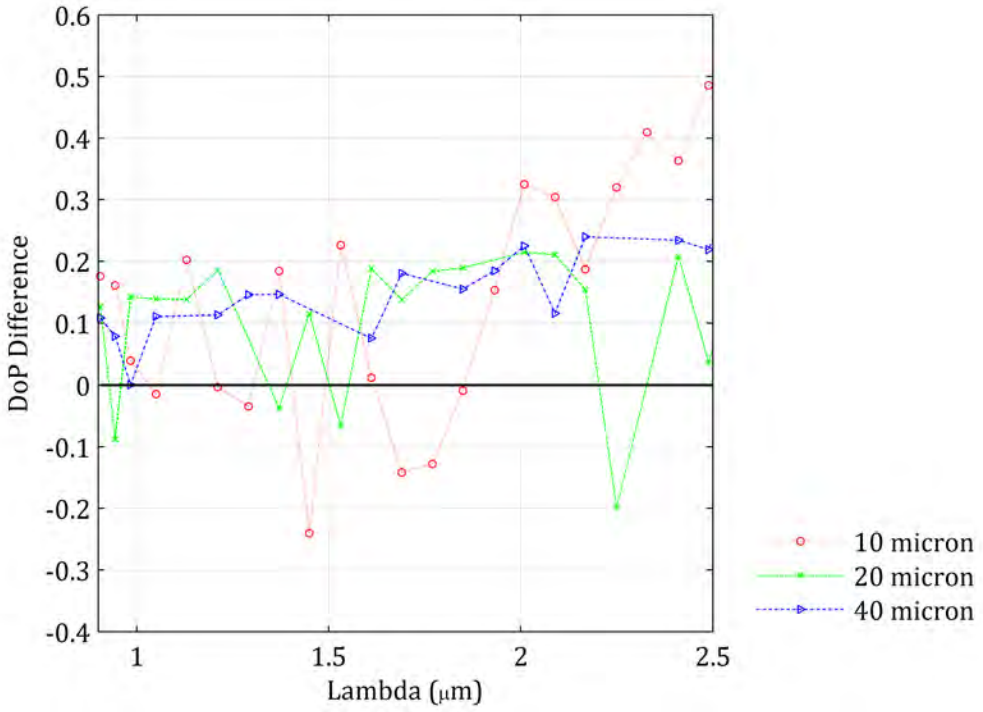

Figure 3.9: Reflection DoP_{diff} results for advection fog for SWIR wavelengths. 10 micron particle size results shown in red (circles), 20 micron particle size results shown in green (x's), and 40 micron particle size results shown in blue (triangles). A black line for $DoP_{diff} = 0$ delineates where linear polarization performs better (negative values) and where circular polarization performs better (positive values).

3.4.2.2 **MWIR to LWIR Wavelengths**

The MWIR and LWIR advection results are shown in Figure 3.10 for transmission and Figure 3.11 for reflection. Similar to the radiation fog results, all three particle sizes show a preference for linear polarization at a single wavelength of 3 microns. As in the radiation fog case, the 10 micron particle clearly shows superior persistence for circular polarization throughout the MWIR and LWIR regions. There is some oscillatory behavior in the 3 – 4 micron wavelength range, but after 4 microns, the 20 micron particle shows a preference for circular polarization through to the end of the LWIR. The 40 micron particle is more limited in wavelengths showing beneficial persistence for circular polarization. There are multiple wavelength ranges in the MWIR. Generally, circular is preferred from 3.5 – 5 microns, with a dip at 4.7 microns, where circular and linear are equal in persistence. Circular polarization has increased persistence for the 40 micron particle through almost all of the LWIR, 7 – 11 microns.

Advection fog shows multiple clear wavelength ranges where circular polarization persists longer than linear polarization. There are some oscillations in the SWIR region, but generally all particle sizes show a preference for circular polarization. The MWIR region is mixed. Circular polarization is preferred for the 10 micron particle through the entire region, the 20 micron particle is positive after a wavelength of 4 microns, and the 40 micron particle oscillates but generally is positive for wavelengths greater than 3.5 microns in the MWIR. Throughout the LWIR regime all particle sizes show superior circular polarization persistence. All the particles show positive DoP_{diff} from 7 – 11 microns. The 40 micron particle is the only

particle that shows any preference for linear polarization in the LWIR, and it is only for wavelengths of 11 – 12 microns. In general, we can expect transmitted circular polarization to persist longer than linear polarization for the LWIR region from 7 to 11 microns with advection fog scattering particles with diameters spanning 10 to 40 microns.

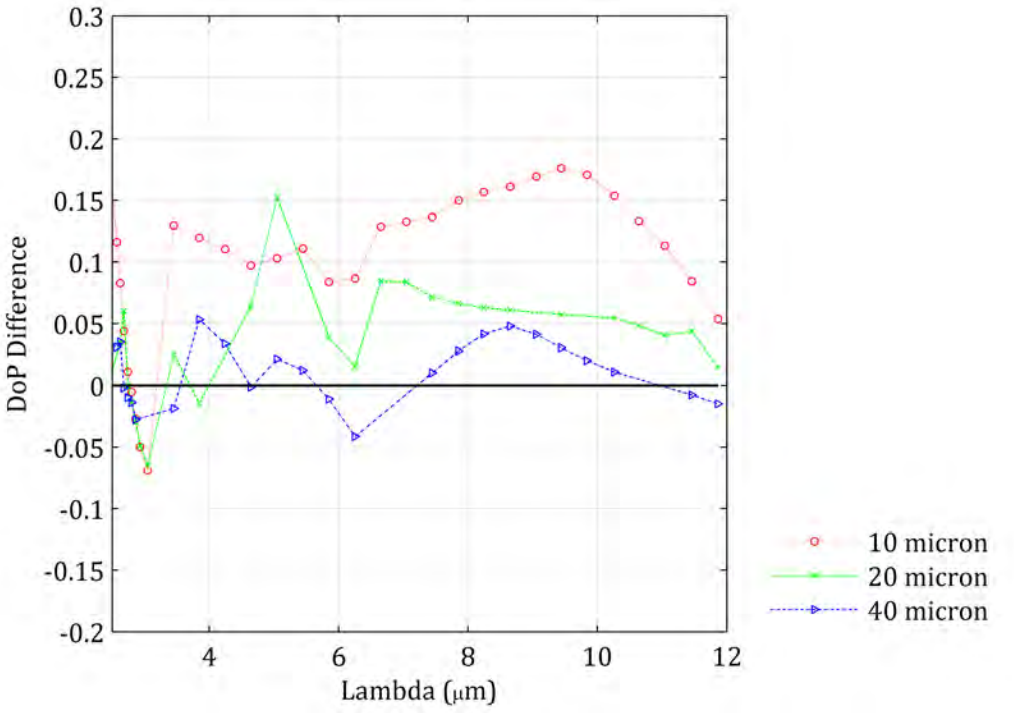

Figure 3.10: Transmission DoP_{diff} results for advection fog for MWIR to LWIR wavelengths. 10 micron particle size results shown in red (circles), 20 micron particle size results shown in green (x's), and 40 micron particle size results shown in blue (triangles). A black line for $DoP_{diff} = 0$ delineates where linear polarization performs better (negative values) and where circular polarization performs better (positive values).

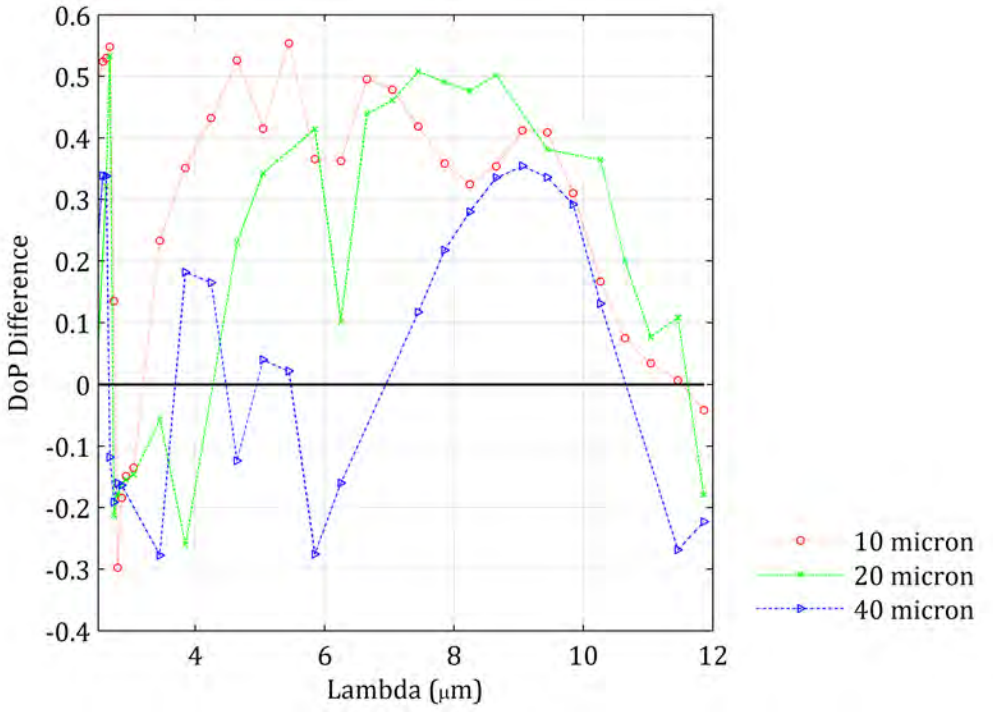

Figure 3.11: Reflection DoP_{diff} results for advection fog for MWIR to LWIR wavelengths. 10 micron particle size results shown in red (circles), 20 micron particle size results shown in green (x's), and 40 micron particle size results shown in blue (triangles). A black line for $DoP_{diff} = 0$ delineates where linear polarization performs better (negative values) and where circular polarization performs better (positive values).

3.4.3 **Small Particle Sahara Dust**

As there is no index data available from Volz *et al.* for SWIR wavelengths, the results for Sahara dust were generated for the MWIR and LWIR regions only, using the available index data [95].

Figure 3.12 and Figure 3.13 shows the results for the small particle Sahara dust model for transmission and reflection. Linear polarization dominates for the very small particle sizes of 0.1 and 1.5 microns. The 1.5 micron particles show possible promise at lower wavelengths. Transmitted circular polarization persists much better for the 1.5 micron particle from 2.5 – 3.25 microns. This performance may be positive in the SWIR region as well, but is left for future investigation. For the larger 6 micron diameter particles, circular polarization persists better than linear throughout the MWIR region as well as the low and high end of the LWIR region. Between a wavelength of 9 and 10.5 microns all three particle sizes show a persistence benefit for linear polarization.

In summary, for small particle Sahara dust, linear polarization persists for the smallest 0.1 micron particle through all wavelengths simulated. Circular polarization persistence dominates for the 1.5 micron particle from 2.5 – 3.25 microns wavelength range, but continues with a smaller linear persistence from the 3.25 – 12 microns wavelength range, similar to the 0.1 microns particle size. Note that all particle sizes, for a wavelength range of 9 – 10.5 microns, maintain a linear polarization persistence. Finally, the 6 micron Sahara dust particles show a large response for two broad wavelength ranges (2.5 – 9 microns and 10.5 – 12 microns) where circular polarization persists longer than linear polarization.

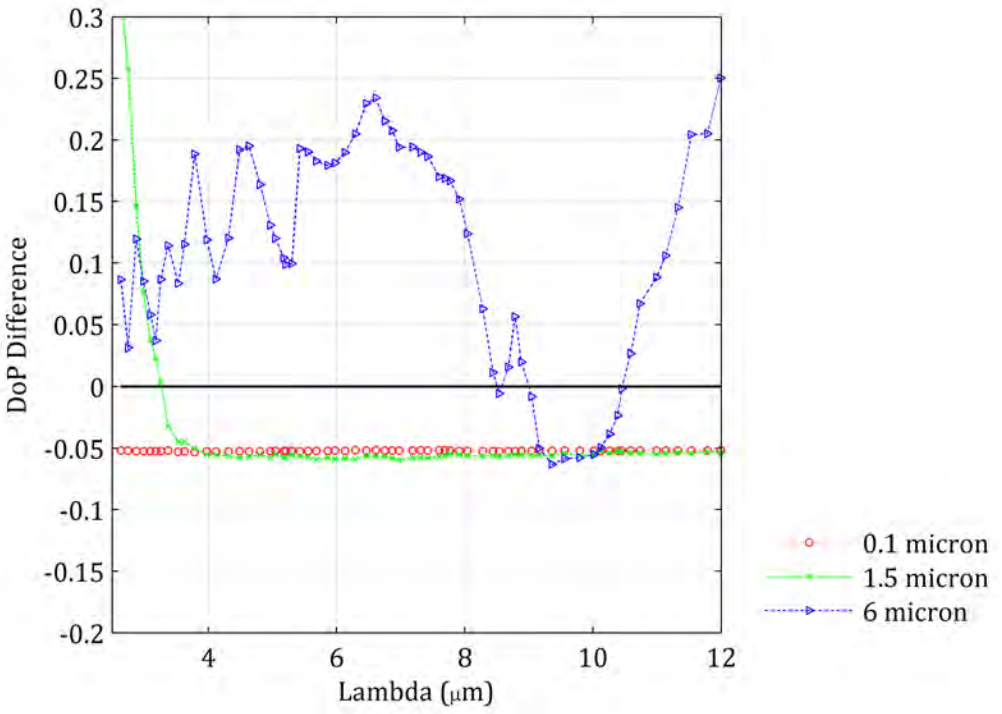

Figure 3.12: Transmission DoP_{diff} for small particle diameters of Sahara Dust for MWIR through LWIR wavelengths. 0.1 micron particle size results shown in red (circles), 1.5 micron particle size results shown in green (x's), and 6 micron particle size results shown in blue (triangles). A black line for $DoP_{diff} = 0$ delineates where linear polarization performs better (negative values) and where circular polarization performs better (positive values).

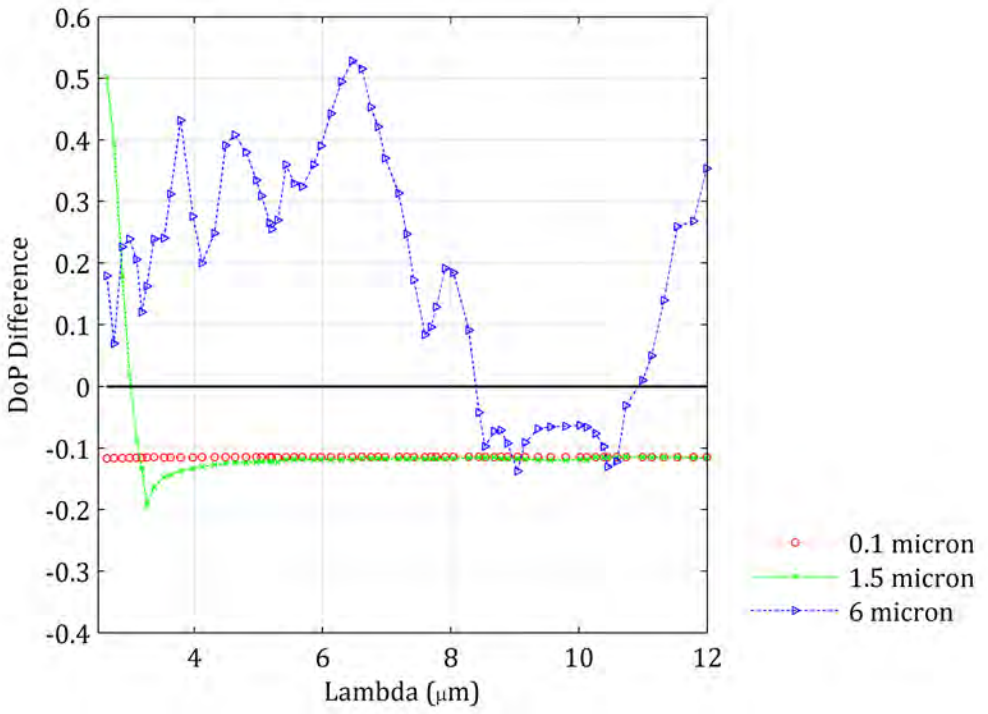

Figure 3.13: Reflection DoP_{diff} for small particle diameters of Sahara Dust for MWIR through LWIR wavelengths. 0.1 micron particle size results shown in red (circles), 1.5 micron particle size results shown in green (x's), and 6 micron particle size results shown in blue (triangles). A black line for $DoP_{diff} = 0$ delineates where linear polarization performs better (negative values) and where circular polarization performs better (positive values).

3.4.4 **Large Particle Sahara Dust**

The results for the large particle Sahara dust model for the MWIR through the LWIR are shown in Figure 3.14 for transmission and Figure 3.15 for reflection. The 10 micron particle oscillates in the MWIR region but shows some preference for transmitted circular polarization from 3.5 to 5 microns. Circular polarization again persists superiorly in the low and high ends of the LWIR region. Specifically, circular polarization is preferred up to wavelengths of 8.75 microns and from 11.25 to 12 microns. The 20 micron particle has a small wavelength range where circular polarization superiorly persists. The wavelength range is from a wavelength of 3.25 to 5.5 microns. The 20 micron particle also has a positive DoP_{diff} value from 7.5 to 8.5 microns, but generally linear polarization persists better in the LWIR for this particle size. The results for the 30 micron particle are nearly identical to the 20 micron particle results. The wavelength ranges are slightly smaller and the overall performance is smaller than with the 20 micron particle.

In summary, for large particle Sahara dust environments, linear polarization shows the dominant persistence benefits for all three particle sizes for a wavelength range of 8.75 – 12 microns. Circular polarization persists superiorly for the 10 micron particle size across a broad wavelength range of 3.5 – 8.75 microns. Otherwise, responses are small and mixed for the 20 and 30 micron particle sizes below a wavelength of 8.75 microns.

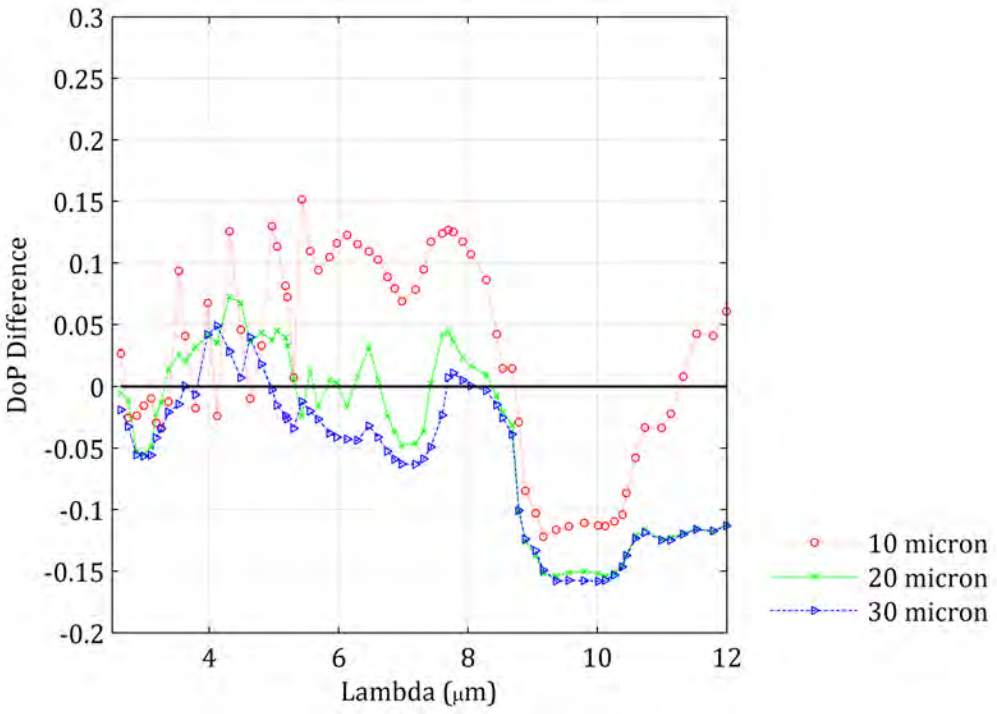

Figure 3.14: Transmission DoP_{diff} for large particle diameters of Sahara Dust for MWIR through LWIR wavelengths. 10 micron particle size results shown in red (circles), 20 micron particle size results shown in green (x's), and 30 micron particle size results shown in blue (triangles). A black line for $DoP_{diff} = 0$ delineates where linear polarization performs better (negative values) and where circular polarization performs better (positive values).

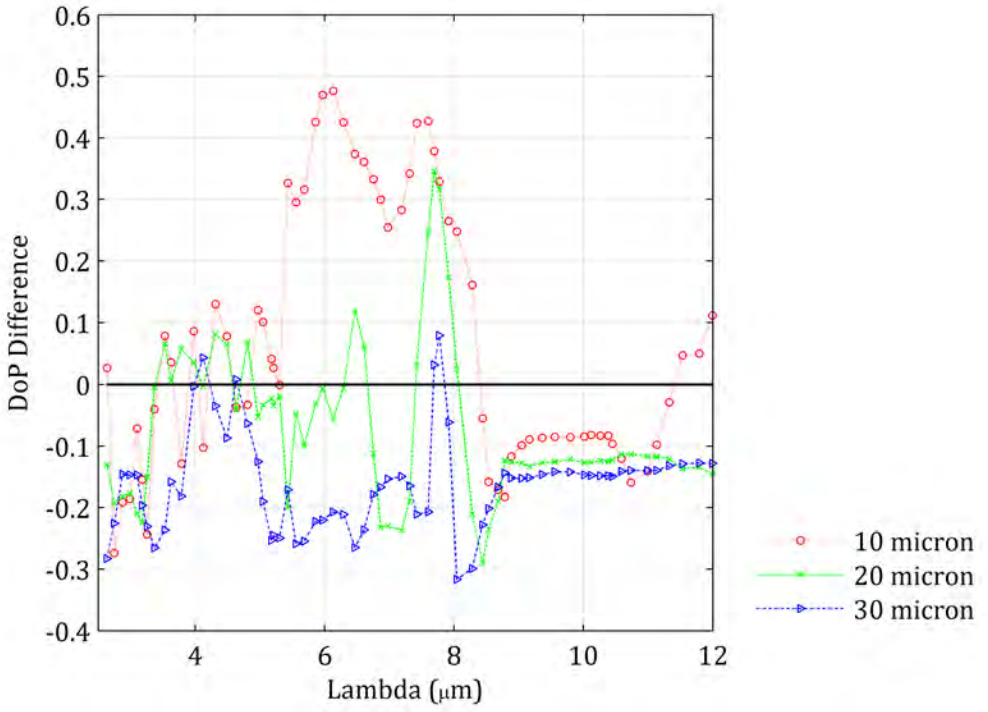

Figure 3.15: Reflection DoP_{diff} for large particle diameters of Sahara Dust for MWIR through LWIR wavelengths. 10 micron particle size results shown in red (circles), 20 micron particle size results shown in green (x's), and 30 micron particle size results shown in blue (triangles). A black line for $DoP_{diff} = 0$ delineates where linear polarization performs better (negative values) and where circular polarization performs better (positive values).

3.5 Summary

Through the use of polarization-tracking Monte Carlo simulations, I have shown that there are clear, broad wavelength ranges where transmitted circular polarization maintains its illuminating polarization state superiorly compared to linear polarization for highly scattering environments representative of fog, including radiation and advection fog. I also examined small and large particle Sahara dust and found that circular polarization maintains its illuminating polarization state, compared to linear polarization, with larger response and over broader wavelength ranges than with linear polarization, but only for the limited particle sizes of 6 microns and 10 microns.

All four realistic environments show wavelength ranges where circular polarization can be utilized to increase detection range. Radiation fog has wavelength ranges available in the entire IR spectrum. All three particle sizes simulated (1, 4, and 10 microns) show a preference for circular polarization in the SWIR, the 4 and 10 micron particles show a preference in the MWIR, and the 10 micron particle exhibits superior persistence for circular polarization in the LWIR. All three particle sizes in the advection fog model (10, 20, and 40 microns) show a preference for circular polarization at SWIR and LWIR wavelengths.

The persistence of circular polarization is positive but not as pronounced for the two dust model particle size regimes (small and large Sahara dust). Here, the 6 micron particle size results from the small particle Sahara dust shows persistence benefits for the broad wavelength ranges of 2.5 – 9 microns and 10.5 – 12 microns. Also in the large Sahara dust simulation, circular polarization persists superiorly for

the 10 micron particle size across a broad wavelength range of 3.5 – 8.75 microns.

This work breaks from previously published works and offers new insight into potential realistic environments with broad wavelength ranges of interest where circular polarization can be utilized to increase detection range. Most previous research focused on singular wavelengths in the visible region with underwater scattering environments typically utilizing readily available polystyrene microspheres, milk, or tissue phantoms as scattering objects. I have produced simulation results supporting broad wavelength responses for particle sizes and refractive indices representative of natural scattering environments, especially noting where circular polarization persists with a larger response and through broader wavelength ranges than linear polarization.

This work should inspire continued interest in circular polarization's benefits in various applications involved in scattering environments, specifically increasing detection range.

CHAPTER 4

Experimental Results and Analysis

4.1 Introduction

This chapter includes original research related to work published in a conference proceedings [97].

This chapter presents experimental and simulation results for underwater scattering environments of polystyrene microspheres in water. The experiments investigate linear polarization and circular polarization individually and the results allow comparison of the two polarization states. These results confirm circular polarization's persistence benefit compared to that of linear polarization. Polystyrene microspheres offer convenient and well-calibrated particle sizes and refractive indices for laboratory measurements. This chapter includes descriptions of the scattering environment, experimental setup, measurement methods, polarimetric calibration procedure, and simulation results. The chapter includes analysis of the variations of simulation results compared to physical experiments. Specifically, the final section of this chapter presents DoP sensitivity differences for circular and linear polarizations from collection geometry variations.

4.2 Scattering Environment: Polystyrene Microspheres

Three underwater scattering environments were investigated. Each scattering environment consisted of a solution of nearly monodisperse particle size distributions of polystyrene microspheres suspended in water. All three solutions were acquired from PolySciences, Inc. The first solution included polystyrene microspheres in water with a mean particle diameter of 0.0824 microns and a standard deviation of 0.006 microns. Similarly, the two other solutions had mean particle diameters of 0.99 and 1.925 microns and standard deviations of 0.03 and 0.042, respectively. These solutions have nearly monodisperse particle distributions and initial simulations consider them as purely monodisperse. Polystyrene's index of refraction as a function of wavelength is easily found in the literature for visible and near infrared wavelengths [19]. The following experiments and simulations were performed at a wavelength of 543.5 nm where polystyrene's refractive index is 1.597. These three particle sizes and the wavelength encompass an isotropically (Rayleigh regime) scattering environment as well as a forward-scattering environment. The size parameters ($x = 2\pi an/\lambda$) of these scattering environments are as follows: 0.635, 7.628, and 14.83. For comparison, size parameters of fog at infrared wavelengths are shown in Table 2.2.

4.3 Experimental Setup

The following experimental setup, shown in Figure 4.1, was built to investigate linearly and circularly incident polarization states on the same scattering environment samples. The experimental setup for circularly and linearly polarized light

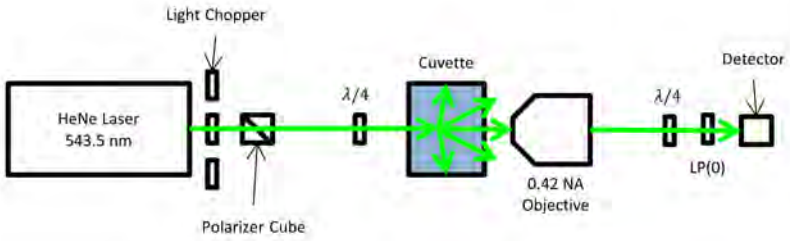

Figure 4.1: Experimental Setup.

investigation was the same. The illumination source was a green HeNe laser at a wavelength of 543.5 nm and power of 5 mW. Due to extremely small signals for the highly scattering environments, a light chopper was implemented. The light exiting the laser was chopped at a frequency of 200 Hz. A polarizing beam cube set the initial polarization state of the light as linearly polarized. The polarization-generating optics consisted of this polarizing beam cube and a quarter-wave retarder (labeled $\lambda/4$ in Figure 4.1). The quarter-wave retarder was mounted in a rotation stage; the retarder was rotated to two different positions in order to generate vertical linear polarization or left circular polarization. To generate vertical linearly polarized light, the quarter-wave retarder was rotated to the 90 degree location where its fast axis is aligned with the incident vertical linear polarization. To generate left circularly polarized light, the quarter-wave retarder was rotated to the 45 degree location. This leaves a 45 degree angle between the incident vertical linear polarized light's oscillation and the quarter-wave retarder's fast axis, thus generating left circularly polarized light.

After the desired polarization state was generated, the light was incident normal

to the front face of a cuvette. The front face of the cuvette has dimensions 1x4 cm and the cuvette has an overall length of 3 cm and height of 4 cm. For each experiment, the cuvette was filled with a volume of 6 mL of a scattering solution, made up of water and various determined densities of polystyrene microspheres. The density of microspheres correlates with the optical thickness, $\tau = \rho\sigma_{ext}L$, of the scattering environment of interest. Measurements began with a small optical thickness and were collected as each set of microspheres were added, resulting in measurements for increasing optical thickness.

Light that propagates through the scattering environment and exits the back face of the cuvette was collected by an objective lens. The objective lens used was a Mitutoyo infinity-corrected objective with a numerical aperture of 0.42. This lens collects all scattered light in a 100 micron radius area with exiting half angles up to 24.83 degrees. The collected light is collimated after passing through the objective lens.

Polarization state analyzing optics determine the polarization state of the collected scattered light. In the experimental set-up, the polarization state analyzing optics consisted of a quarter-wave retarder and a polarizer. Both the quarter-wave retarder and the polarizer were mounted in rotation stages. A 1 cm square detector collected the light after it went through the polarization analyzing optics. The polarizer was set to the 0 degree location for all measurements. A lock-in amplifier was used with the detector and light chopper to increase signal-to-noise for the highly scattering solutions. The polarization analyzing optics was configured as a rotating quarter-wave retarder fixed-polarizer polarimeter. This is a full Stokes polarimeter,

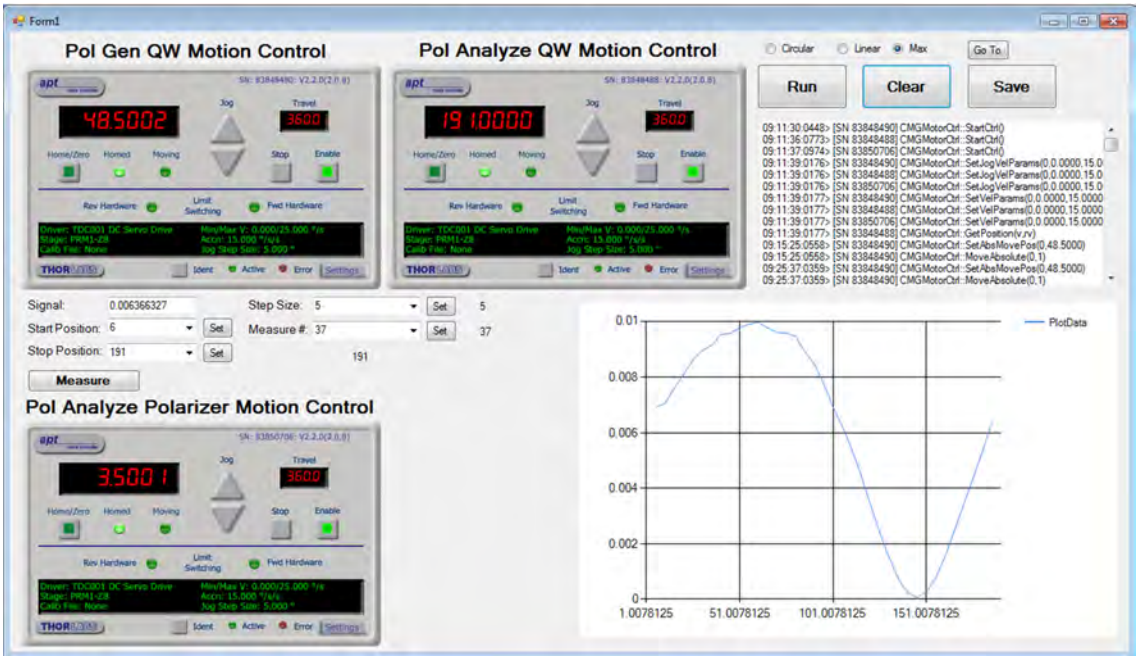

Figure 4.2: Experimental software graphical use interface.

therefore, it can measure all four Stokes parameters.

4.4 Measurement Automation

Software was developed to control the various components of the experimental setup. The software interface is shown in Figure 4.2. The rotation mounts each had their own separate controls and are labeled **Pol Gen QW**, **Pol Analyze QW**, and **Pol Analyze Polarizer** in Figure 4.2. The number of measurements and angular separation between measurements were set for automated rotation of the rotating retarder fixed polarizer polarimeter. The software also shows measurement results as they are taken, plotting the polarization modulation of the collected light.

4.5 Measurement Process and Polarimeter Calibration

Signal modulations from the rotating-retarder, fixed-polarizer polarimeter measure the transmitted scattered Stokes parameters. For each individual angular position of the retarder, 100 measurement samples were collected at a rate of 512 Hz. Voltage signals were collected from the detector via the lock-in amplifier. These 100 samples were averaged and saved as a single measurement value for the given rotating quarter-wave retarders angular position. This process was repeated for all the desired angular positions of the retarder. Three measurements were made for each solution at each incident polarization state, resulting in a total of six measurements for each solution. The three separate measurements were averaged for the final single angular position measurement value. A flowchart of the experimental process is shown in Figure 4.3.

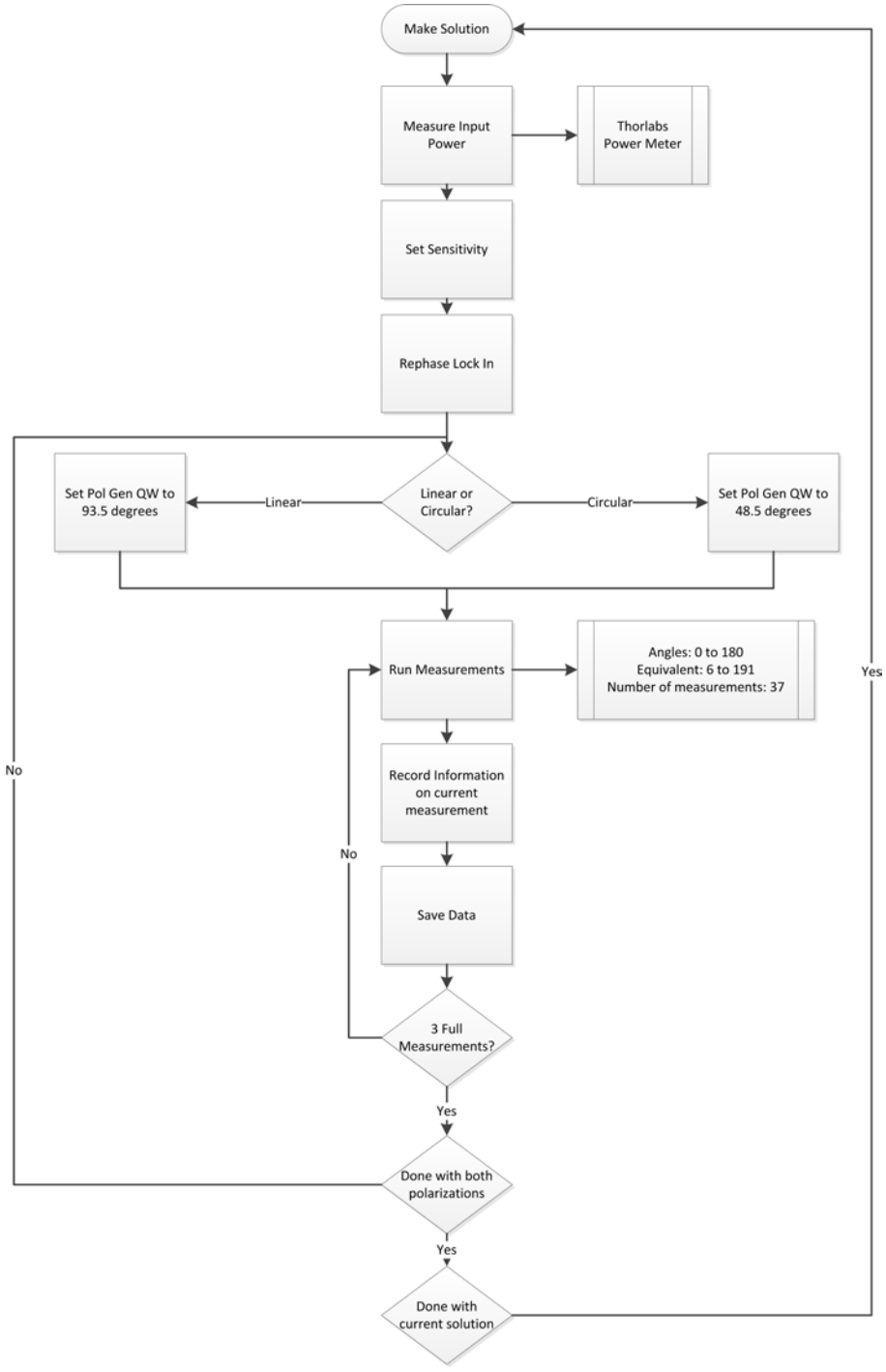

Figure 4.3: Experimental measurement process flowchart.

4.5.1 **Curve Fit Calibration**

For all the Stokes parameter calculations, 37 angular location measurements were used, corresponding to 5 degree increments from 0 to 180 degrees. The rotating quarter-wave retarder fixed polarizer polarimeter initially measured the polarization modulation when the cuvette was filled with only water. The measured curves for incident linear and circular polarizations were compared to the ideal fit. The ideal fit equation for the modulation of the polarization components for this type of polarimeter is given as [69],

$$\frac{1}{2}\begin{bmatrix} 1 & 1 & 0 & 0 \\ 1 & 1 & 0 & 0 \\ 0 & 0 & 0 & 0 \\ 0 & 0 & 0 & 0 \end{bmatrix} \begin{bmatrix} 1 & 0 & 0 & 0 \\ 0 & cos^2(2\theta) & cos(2\theta)sin(2\theta) & -sin(2\theta) \\ 0 & cos(2\theta)sin(2\theta) & sin^2(2\theta) & cos(2\theta) \\ 0 & sin(2\theta) & -cos(2\theta) & 0 \end{bmatrix} \begin{bmatrix} S_0 \\ S_1 \\ S_2 \\ S_3 \end{bmatrix} \tag{4.1}$$

$$I(\theta) = \frac{1}{2}(S_0 + S_1 cos^2(2\theta) + S_2 sin(2\theta)cos(2\theta) - S_3 sin(2\theta)). \tag{4.2}$$

The resulting measurement curves for linearly and circularly incident polarized light are shown in Figure 4.4 and Figure 4.5. The resulting measured normalized Stokes parameters for the linearly polarized incident light are $\mathbf{S} = (1.00, -0.9496, -0.0001, -0.1006)^T$, with a DoP of 0.9549 and a $DOLP$ of 0.9496. The coefficient of determination (R squared) is equal to 0.996, thus this is a very good fit to the measured curve. The resulting measured normalized Stokes parameters for the circularly polarized incident light are $\mathbf{S} = (1.00, 0.3914, -0.0705, -0.9526)^T$, with a DoP of 1.0004 and a $DoCP$ of 0.9526. The coefficient of determination is

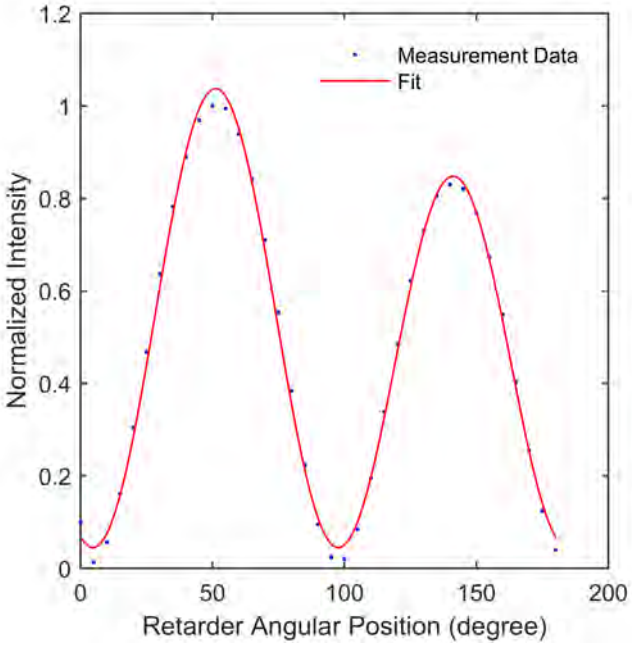

Figure 4.4: Measurement calibration curve fit for linearly polarized incident light.

equal to 0.9986, also a very good fit to the measured data. The reader will notice that the Stokes parameters are not perfectly linearly or circularly polarized; this variation is due to non-ideal optical elements in the system as well as not perfect angular positions of each polarization element [98]. If the system were ideal, the Stokes vectors for linearly and circularly polarized light would be $\mathbf{S} = (1, 1, 0, 0)^T$ and $\mathbf{S} = (1, 0, 0, 1)^T$, respectively.

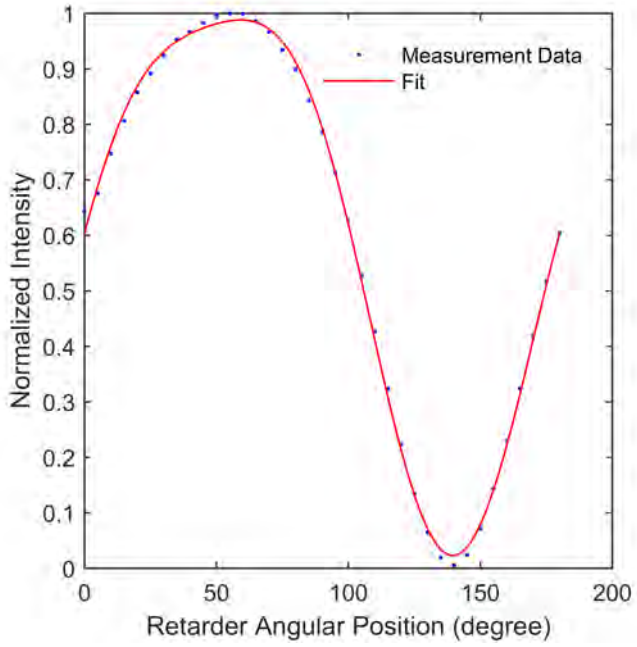

Figure 4.5: Measurement calibration curve fit for circularly polarized incident light.

4.5.2 **Data Reduction Matrix Calibration**

The calibration and generation of the Stokes parameters and DoP for measurements with scattering solutions were determined using the data reduction matrix method. This method is similar to the curve fitting procedure, as both fit the measured data to the modulation signals for each polarization component using a least squares fit, but the data reduction matrix method utilizes matrix calculus and takes into account the non-ideal optical elements. The basics of polarimetry are briefly described in Chapter 2 Section 2.1.3. The details of polarimetry using the data reduction matrix are explained in the following paragraphs.

In order to determine the Stokes parameters for collected light, a set of measurements are made with a set of polarization analyzers. For an individual measurement,

the measured intensity of light is given by,

$$I_q = \mathbf{A}_q \mathbf{S}, \tag{4.3}$$

where I_q is the measured intensity, $\mathbf{A}_q$ is the analyzer vector, and $\mathbf{S}$ is the light's Stokes vector. For the experimental measurements, 37 angular measurements were made and therefore the intensity values make up the $\mathbf{I}$ vector of the measurement equation [99],

$$\mathbf{I} = \begin{bmatrix} I_0 \\ I_1 \\ \vdots \\ I_{36} \end{bmatrix} = \mathbf{WS} = \begin{bmatrix} a_{0,0} & a_{0,1} & a_{0,2} & a_{0,3} \\ a_{1,0} & a_{1,1} & a_{1,2} & a_{1,3} \\ \vdots & \vdots & \vdots & \vdots \\ a_{36,0} & a_{36,1} & a_{36,2} & a_{36,3} \end{bmatrix} \begin{bmatrix} S_0 \\ S_1 \\ S_2 \\ S_3 \end{bmatrix}. \tag{4.4}$$

The individual analyzer vectors for each measurement position populate the $\mathbf{W}$ matrix. This matrix is a 4x37 sized matrix. The $\mathbf{W}$ matrix is determined by the polarization analyzing optics. Each column of the $\mathbf{W}$ matrix corresponds to each Stokes parameter's polarization modulation values, similar to the modulations in Equation 4.2. For the ideal case, plotting each column of the $\mathbf{W}$ matrix will yield the same curves as in Equation 4.2. With a known input polarization state, the $\mathbf{W}$ matrix can be calibrated to take into account all the non-ideal optical elements in the experimental setup. For the experiments presented here, this analysis was performed with the known polarization output from the polarizer beam cube. The $\mathbf{W}$ matrix was generated through a least squares fit process taking into account all

non-ideal optical element's parameters, such as diattenuation and retardance.

Ultimately, the desired resultant data from the collected light are the Stokes parameters. This is found by using the inverse matrix relationship.

$$\mathbf{S}_{measured} = \mathbf{W}^{-1}\mathbf{I} \tag{4.5}$$

Since the number of measurements in this experiment was larger than four (the number of Stokes parameters) the system is considered overdetermined. Instead of using the typical inverse matrix, a pseudoinverse is used. The pseudoinverse generates the best least squares estimate of $\mathbf{S}_{measured}$ when random noise is present. Thus, the measured Stokes parameters are given by,

$$\mathbf{S}_{measured} = (\mathbf{W}^T\mathbf{W})^{-1}\mathbf{W}^T\mathbf{I} = \mathbf{W}_p^{-1}\mathbf{I}. \tag{4.6}$$

This pseudoinverse matrix is called the data reduction matrix. This technique is used for all the following experimental results.

4.6 Experimental Results

The following results are separated by each environment of interest starting with the smallest particle size and ending with the largest. Each set of results investigates the persistence of linearly and circularly polarized light when transmitting through increasing optical thicknesses of polystyrene microspheres in water. The experimental results are compared to simulations of the same scattering environments at similar optical thicknesses.

4.6.1 **0.0824 micron Particle Size: Measurement**

The results for the 0.0824 micron particle size are shown in Figure 4.6. In the following section I discuss these results and compare them to theory. This scattering environment contains particles that are very small compared to the incident wavelength. The particles size parameter for this environment is 0.635. This type of scattering environment is isotropically scattering (i.e. Rayleigh regime), meaning the light is scattered in all directions equally. As a result, even for low numbers of scattering events, photons are scattered in large angles.

For this environment, linearly polarized light maintains its DoP better than circularly polarized light. This is a small effect for the measured samples. As the optical thickness increases, the DoP for both linear and circular polarization follow the same trend; both polarization states depolarize. Circular polarization is depolarized more than linear polarization but both decrease at the same rate. This is apparent in the simulation results as well. The simulation results are much more highly depolarized than the experimental results. The simulation results show a larger separation between linear and circular polarization's DoP values than the experimental results.

Despite these variations, the overall trend is the same for both measurement and simulation results: linearly polarized light persists better through the isotropically scattering environment than circularly polarized light, but the effect is small. The discrepancy between the simulation and experimental results is likely due to the experimental constraints. The cuvette in the experiments was very skinny in the lateral x and y dimensions compared to that used in the simulated environment. The

simulations assume an unbounded slab of scattering material in the lateral x and y dimensions. The z dimension for both simulation and experiments are the same. In simulations, a large number of photons scattered outside the bounds of the physical cuvette are able to return; they are counted as exiting the back face of the cuvette and collected by the objective lens. This can result in a much larger depolarization in the simulation results than the depolarization found in the experimental results. During simulation, many more multiply-scattered, highly-depolarized photons are collected than in the experimental case. In the experimental case, the collected photons are scattered only a few times, or not at all. The simulation results show this and later sections will explore this in more detail.

This experimental constraint is why for small optical thicknesses, the simulation results for isotropically scattering particles can have very low DoPs. Overall, the trends seen in simulations and experiments are similar, but the experimental results are not able to match those produced with the infinite slab width in simulations. Linear polarization persists longer than circular polarization for this environment, but measurements are only able to measure photons with small numbers of scattering events, and sampling only the photons that are scattered at small forward scattering directions.

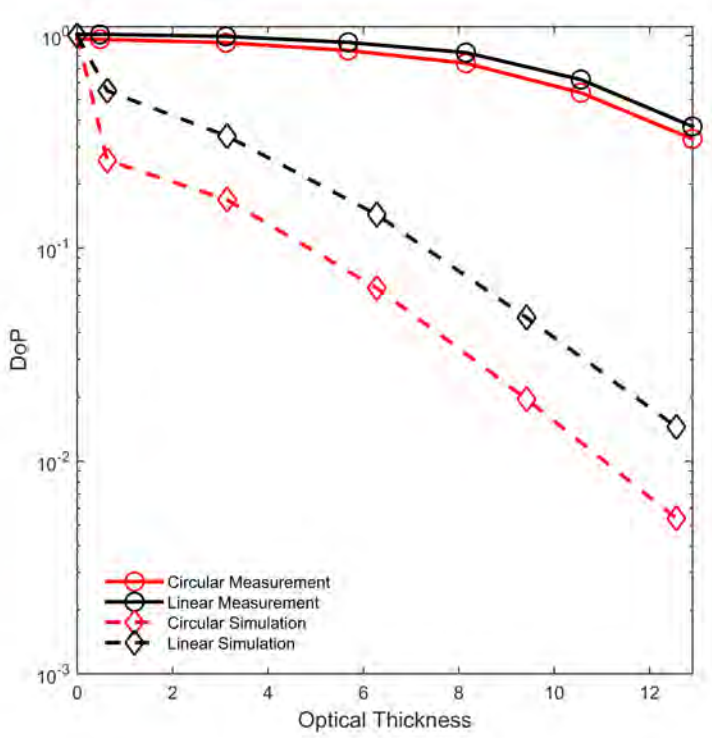

Figure 4.6: *DoP* versus optical thickness for measured and simulated scattering environments of 0.0824 micron polystyrene spheres in water.

4.6.2 **0.99 micron Particle Size: Experiment**

The results for the 0.99 micron particle size are shown in Figure 4.7. This scattering environment contains particles that are much larger than the incident wavelength, resulting in a size parameter of 7.628, that is ten times greater than that of the first environment. This type of scattering environment is forward scattering, meaning the light is scattered preferentially into a small range of angles in the forward direction.

For this environment, circularly polarized light persists longer than linearly polarized light. This is the case for both the experimental results as well as the simulation results. Circular polarization's performance in the scattering environment nearly matches that of the simulation results. The measured linear polarization response is higher than that in the simulations. Once again, this discrepancy is most likely due to the lateral dimensional constraints of the cuvette used in the measurements. A comment from Freund and Kaveh regarding the polarization memory work of MacKintosh *et al.* addresses a similar discrepancy [61, 100]. Freund and Kaveh point out that the walls of a cuvette can cause internal surface reflections that are not taken into account in simulations. The reflections from the inner surface of the cuvette will re-inject certain portions of the light and can be polarization dependent. These internal reflections are not taken into account by these simulations. As previously stated, the simulations assume an infinitely wide slab but are finite and well defined in the z direction. It is hypothesized here that the cuvette walls allow photons to be detected with fewer scattering events than would be the case in simulations. This limits the polarization degradation upon detection. Since circular polarization (shown later in Section 4.7) proves to be more tolerant of these

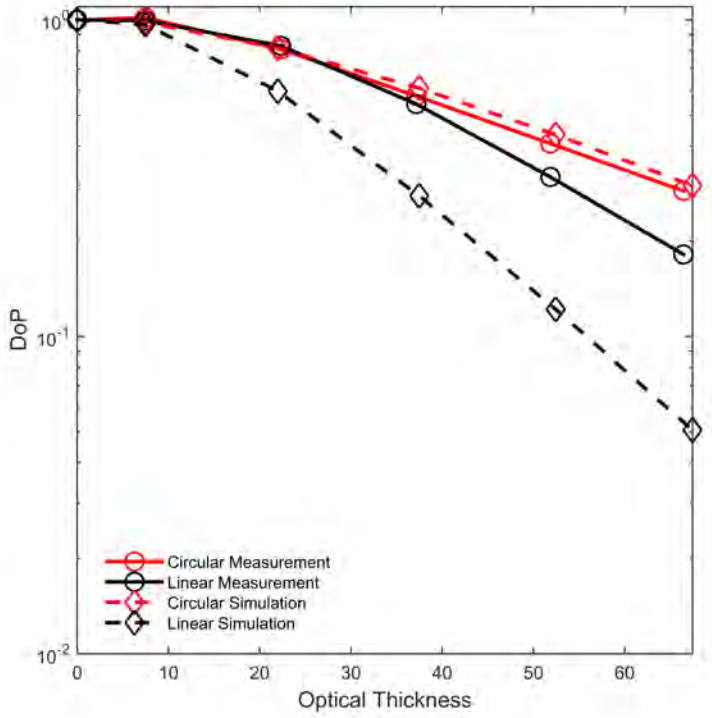

Figure 4.7: *DoP* versus optical thickness for measured and simulated scattering environments of 0.99 micron polystyrene spheres in water.

configurational variables, this cuvette enabled short-cut is not so detectable. Overall, circularly polarized light persists longer than linearly polarized light for this environment in spite of the cuvette surfaces and limited width.

4.6.3 **1.925 micron Particle Size: Measurement**

The results for the 1.925 micron particle size are shown in Figure 4.8. This scattering environment is similar to the 0.99 micron particle size in that it contains particles that are much larger than the incident wavelength. The environment is again forward scattering and the resulting size parameter for this environment is

14.83.

Results for this environment are similar to the previous forward-scattering 0.99 micron particle scattering environment. Circularly polarized light persists longer than linearly polarized light. As with the earlier forward-scattering case, circular polarization's measured DoP is close to the simulated values and linear polarization's DoP is higher than the simulated values. The same experimental dimensional issues are present with this measurement when comparing to the simulation results. It is hypothesized here that the cuvette walls allow photons to be detected with fewer scattering events than would be the case in simulations. Circular polarization outperforms linear polarization in spite of the cuvette constraints.

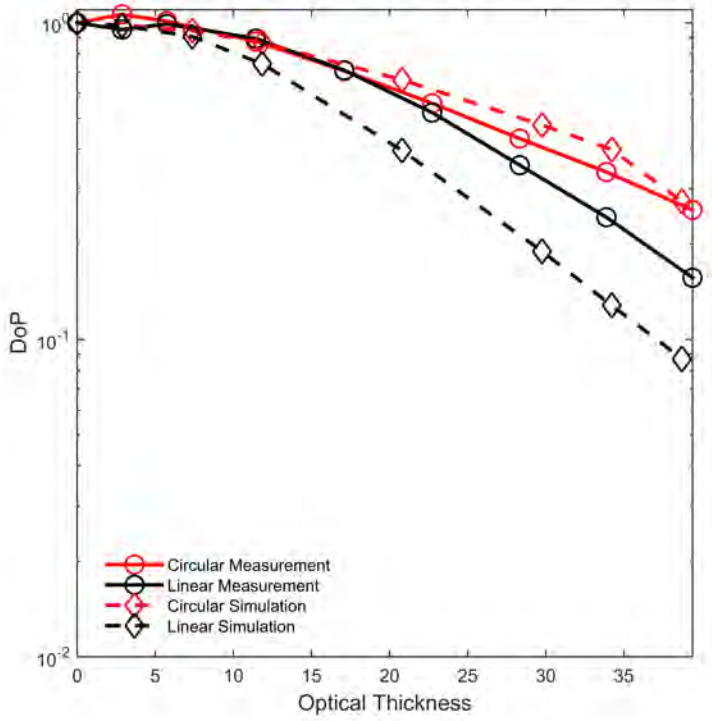

Figure 4.8: *DoP* versus optical thickness for measured and simulated scattering environments of 1.925 micron polystyrene spheres in water.

4.7 Collection Geometry Variations

The area and angular collection for the simulation results previously shown are consistent with those in the specific experimental setup. The experiments collected scattered photons from one area and angular collection geometry: 100 micron radius and 24.43 degree half angle collection. The experiments were limited in the lateral extent of the scattering environment due to the size of the cuvette used. This section will explore the variation in polarization's persistence when collection area and angles are varied in simulation.

Research investigating these variations is very limited. Ghosh *et al.* investigated two different scattering environments and the variation of collection angle on the measured DoP [101]. The environments investigated were 0.11 micron polystyrene microspheres in water at an optical thickness of 8.3, and 1.08 micron polystyrene microspheres in water with an optical thickness of 15, both illuminated with 632 nm light. The collection angle was varied from 2.5 to 16.4 degrees. The experiments did not keep the area of collection constant, so as collection angle increased, the area of collection also increased. They showed that as the collection angle and area is increased the DoP for both environments decreases. These results are limited to only a few sets of angular variations and do not separate the collection area as a separate variable.

Simulation results for varying collection geometry for the 0.0824 micron, 0.99 micron, and 1.925 micron environments are presented here. The following simulation results will show larger angular and area collection gathers more multiply scattered photons, therefore decreasing the collected DoP. Forward scattering en-

vironments do not vary as much as the isotropic scattering environment and show a larger variation for linear polarization than circular polarization. When investigating the persistence of polarization through scattering environments, the collection geometry as well as the extent of the scattering environment must be taken into careful consideration, as evidenced throughout this dissertation.

4.7.1 **0.0825 micron Particle Size: Simulation**

Figure 4.9 and Figure 4.10 show the simulation results for varying collection geometry for the small particle size scattering environment. Each figure has four plots for increasing angular collection: a) 10 degree half angle collection, b) 30 degree half angle collection, c) 50 degree half angle collection, and d) 70 degree half angle collection. Within each subplot the variation due to the area collection is shown. The collection area is circular on the output face of the cuvette with radii of 0.25, 0.5, 1, and 2 cm.

For the small particle environment, both linearly and circularly incident polarized light's transmitted DoP are affected by both the collection area and collection angle. As the collection angle increases the DoP of the collected light decreases for both polarization states. As the collection angle increases a larger number of multiply scattered photons are collected. This small particle environment is isotropically scattering and the results show that the angular collection variation has a lesser effect than the area collection variation. A change in the collection area on the exit face of the cuvette results in large changes in the collected DoP. Since light is scattered at broader angles in the isotropically scattering environment, the larger

collection area collects a larger number of photons that scatter off the incident beam's axis. This significant variation due to area collection is greatest for the small particle environment. The increased collection area issue further explains why the experiment's cuvette width is detrimental to achieving results that match the simulation results. The isotropically scattering particles scatter photons over a larger area than the forward-scattering environments does; thus, using a thin cuvette in experiments will filter out the larger angles of scattering and not collect as many multiply scattered photons.

Regardless of the collection geometry, circular polarization results in smaller signal persistence than linear polarization in a small particle size scattering environment. Both polarizations are affected by the variation of collection area and angle, but the collection area has a larger effect. The isotropic scattering particle environment scatters photons at larger angles and therefore more depolarized photons are off the axis of the incident beam.

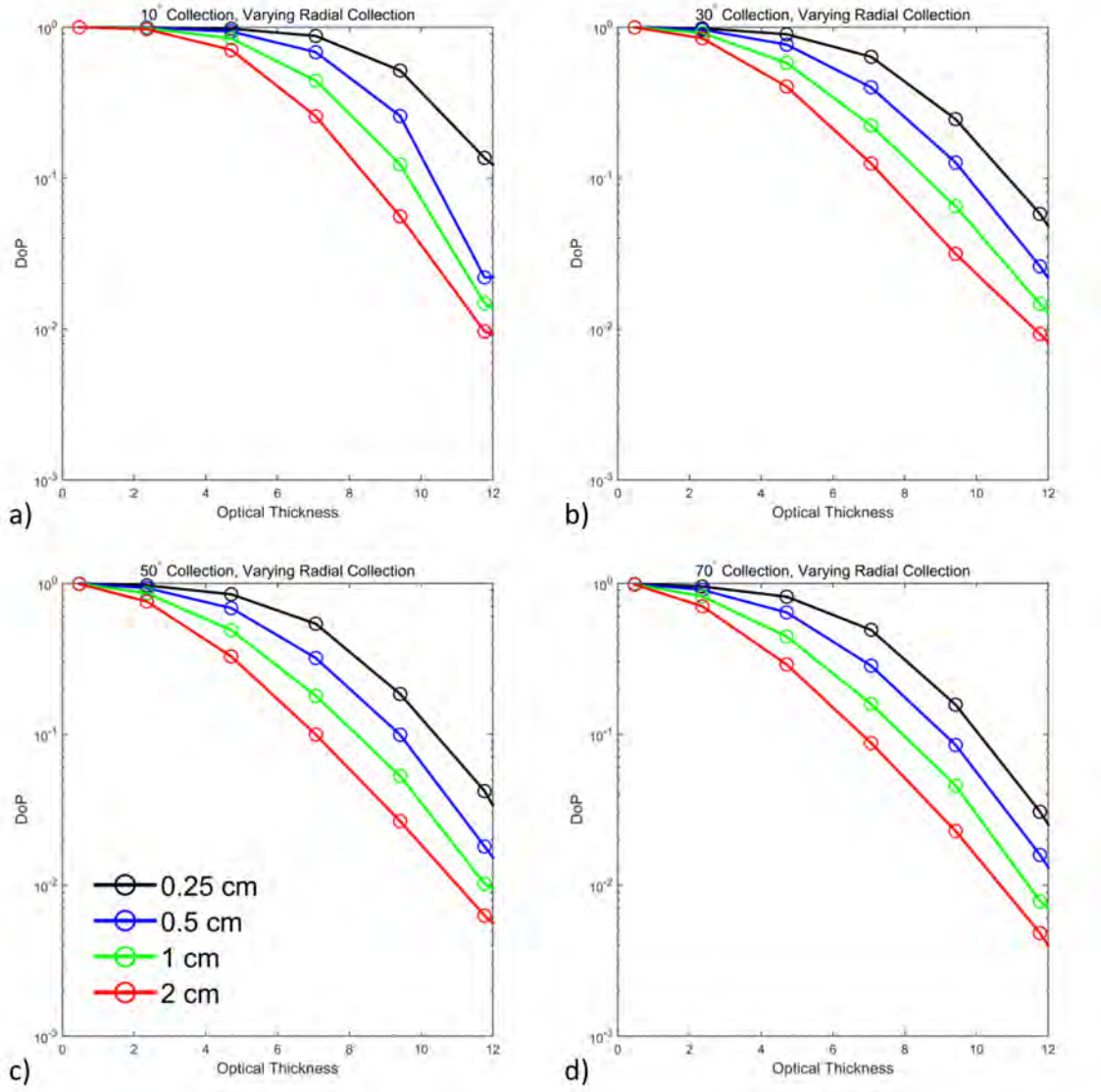

Figure 4.9: *DoP* versus optical thickness changes with variation of the angular and area collection geometry for incident linearly polarized incident light for a scattering environment of 0.0824 micron polystyrene microspheres in water. Radial area collection variation from 0.25 to 2 cm on the output face for a) 10 degree half angle collection, b) 30 degree half angle collection, c) 50 degree half angle collection, and d) 70 degree half angle collection.

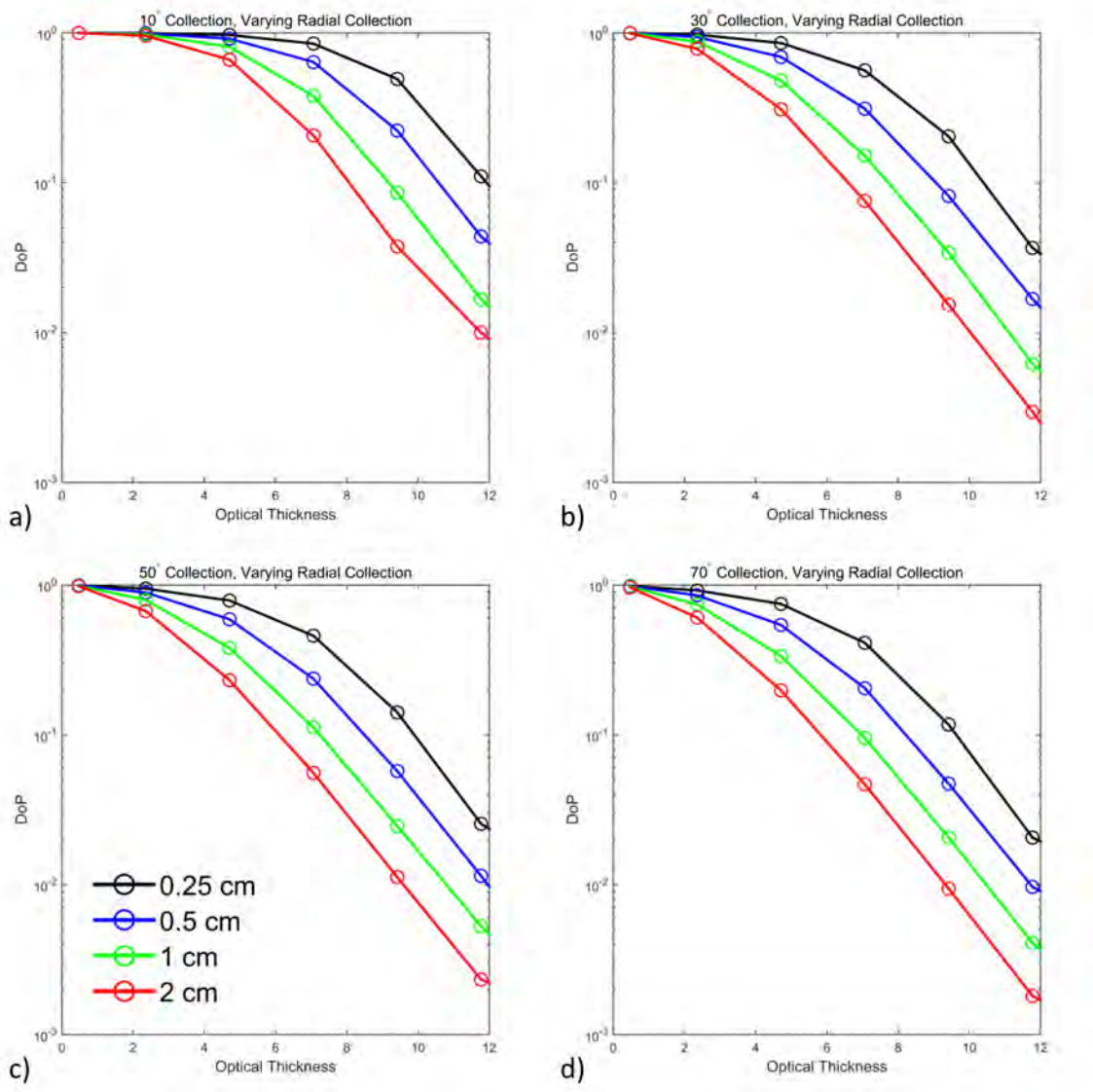

Figure 4.10: *DoP* versus optical thickness changes with variation of the angular and area collection geometry for incident circularly polarized incident light for a scattering environment of 0.0824 micron polystyrene microspheres in water. Radial area collection variation from 0.25 to 2 cm on the output face for a) 10 degree half angle collection, b) 30 degree half angle collection, c) 50 degree half angle collection, and d) 70 degree half angle collection.

4.7.2 **0.99 micron Particle Size: Simulation**

Figure 4.11 and Figure 4.12 show the simulations for varying collection geometry for the 0.99 micron particle scattering environment. The figure layout is the same configuration as that for the previous 0.0824 micron environment simulations.

The large particle environment results show a much different variation than the small particle environment results. In the large particle environment, both angular and area collection variation decrease the DoP for the linearly incident polarization. This variation has a much smaller effect than it did in the small particle case. The angular variation has a smaller effect than the collection area variation. As the collection angle increases, the DoP decreases but the change is small. Variations in the area cause a larger change in the collected DoP. There is no real difference between the 0.25 cm and 0.5 cm collection area variation. Area collections greater than 0.5 cm show a slightly larger change in the collected DoP.

Circular polarization shows a very different behavior. Variation of both the angles collected and the area collected show almost no change in the collected DoP. All four subplots look nearly identical. There is nearly no change in the collected DoP for larger angle collection. Circularly polarized light is highly polarized even for multiply scattered photons at large angles. There is a small variation in the collected DoP when the collection area is increased. The DoP decreases when the collection area is increased, but it is an insignificant decrease, less than 0.1. Circular polarization's transmitted DoP is not largely affected by changes in the collection geometry for the larger 0.99 micron particle scattering environment.

For this 0.99 micron particle forward-scattering environment, circular polariza-

tion is more tolerant to variations in collection geometry than linear polarization. The experimental results for the forward-scattering environment and the collection geometry simulations for the 0.99 micron particle showed another reason why linear polarization measurements do not match the simulations. Linear polarization is more susceptible to the collection area variations and photons that are scattered off the axis of the incident beam. The cuvette interferes with these off-axis linearly polarized photons more than the circularly polarized photons. Since circular polarization proves to be more tolerant of these collection geometry variations, the effects of the cuvette are not so detectable compared to linear polarization.

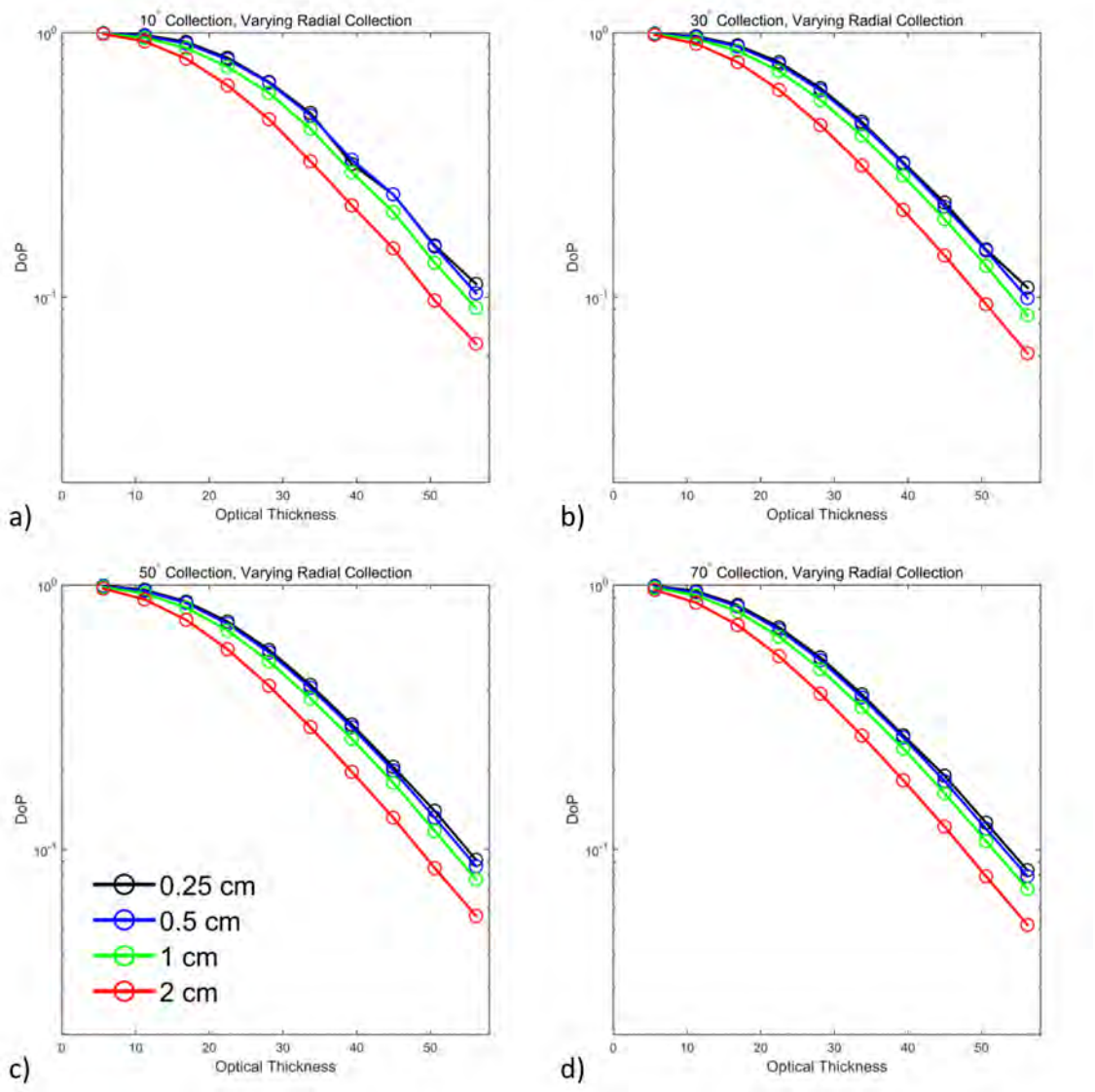

Figure 4.11: *DoP* versus optical thickness changes with variation of the angular and area collection geometry for incident linearly polarized incident light for a scattering environment of 0.99 micron polystyrene microspheres in water. Radial area collection variation from 0.25 to 2 cm on the output face for a) 10 degree half angle collection, b) 30 degree half angle collection, c) 50 degree half angle collection, and d) 70 degree half angle collection.

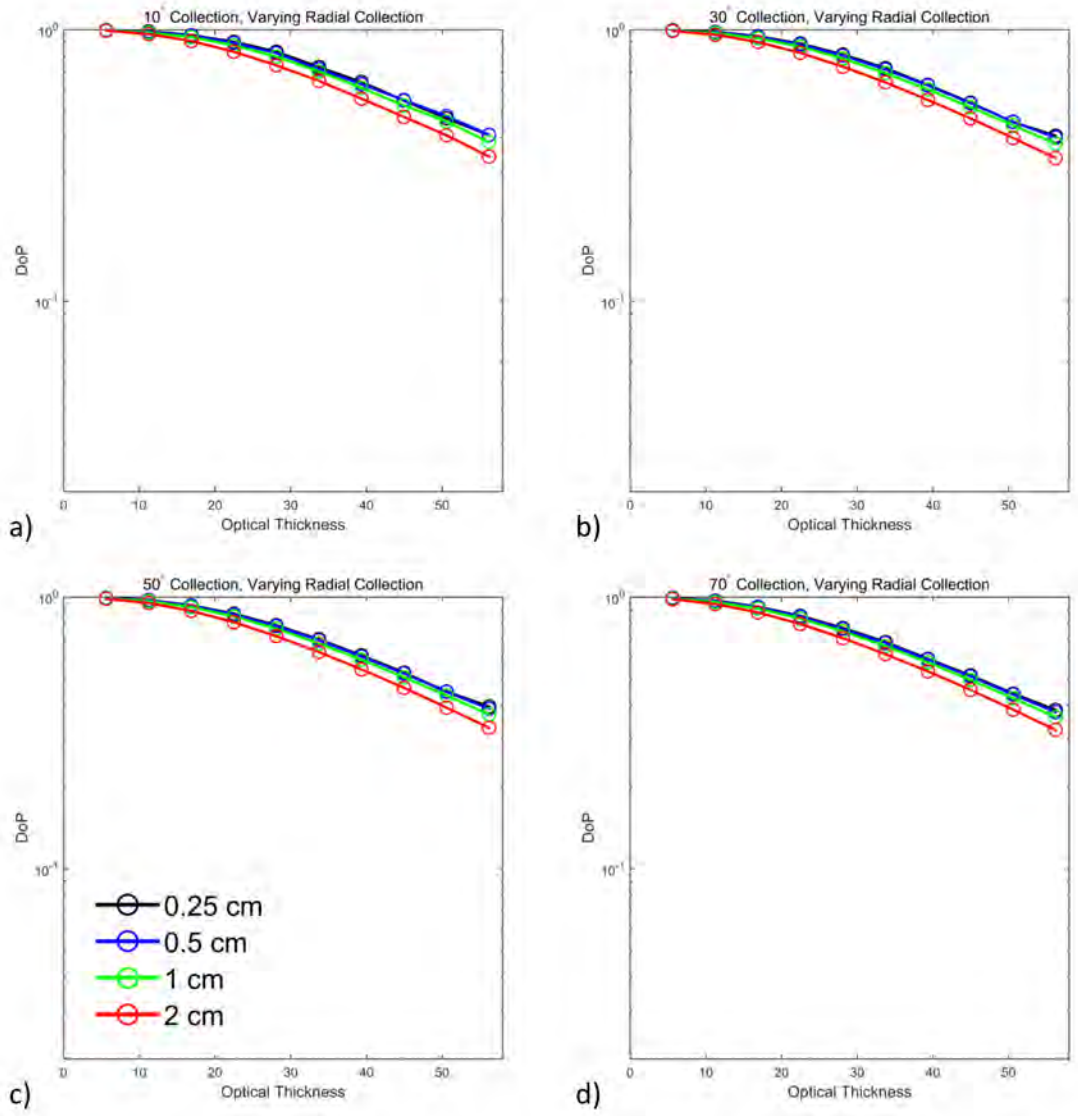

Figure 4.12: *DoP* versus optical thickness changes with variation of the angular and area collection geometry for incident circularly polarized incident light for a scattering environment of 0.99 micron polystyrene microspheres in water. Radial area collection variation from 0.25 to 2 cm on the output face for a) 10 degree half angle collection, b) 30 degree half angle collection, c) 50 degree half angle collection, and d) 70 degree half angle collection.

4.7.3 **1.925 micron Particle Size: Simulation**

Figure 4.13 and Figure 4.14 show the simulations for varying the collection geometry for the 1.925 micron particle scattering environment.

The 1.925 micron particle environment exhibits similar results to the previous 0.99 micron forward-scattering environment results. As with the 0.99 micron environment, linear polarization shows a larger variation due to the collection geometry than circular polarization. Collection area variations have a larger effect than angular variations. Circular polarization shows more variation for this 1.925 micron particle size than it did for the 0.99 micron particle environment, although the variation is still very small.

For both forward-scattering environments, particle sizes of 0.99 and 1.925 microns, circular polarization is not changed significantly by variations in collection geometry and environmental extent. Linear polarization exhibits different characteristics. Linear polarization is more affected by variations in the collection area and environmental extent. Linear polarization is also affected to a smaller degree by variations in collection angle. Linear polarization is more susceptible to changes in the collection geometry, which can lead to uncertainty when the experimental scattering environment geometry is not perfectly matched to the simulations. Circular polarization proves to be more tolerant of these collection geometry variations, the effects of the experimental geometry are not so detectable compared to linear polarization.

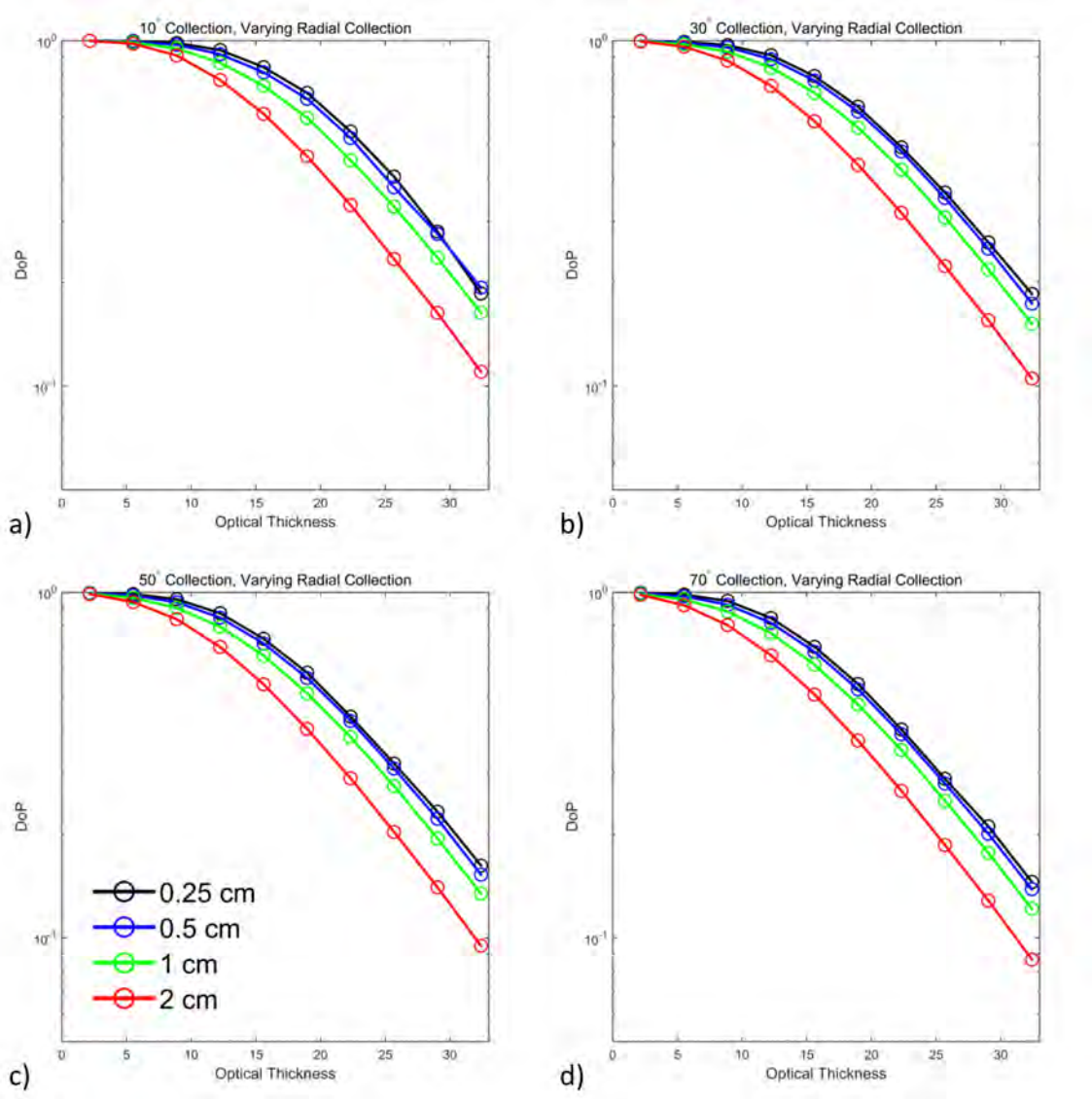

Figure 4.13: *DoP* versus optical thickness changes with variation of the angular and area collection geometry for incident linearly polarized incident light for a scattering environment of 1.925 micron polystyrene microspheres in water. Radial area collection variation from 0.25 to 2 cm on the output face for a) 10 degree half angle collection, b) 30 degree half angle collection, c) 50 degree half angle collection, and d) 70 degree half angle collection.

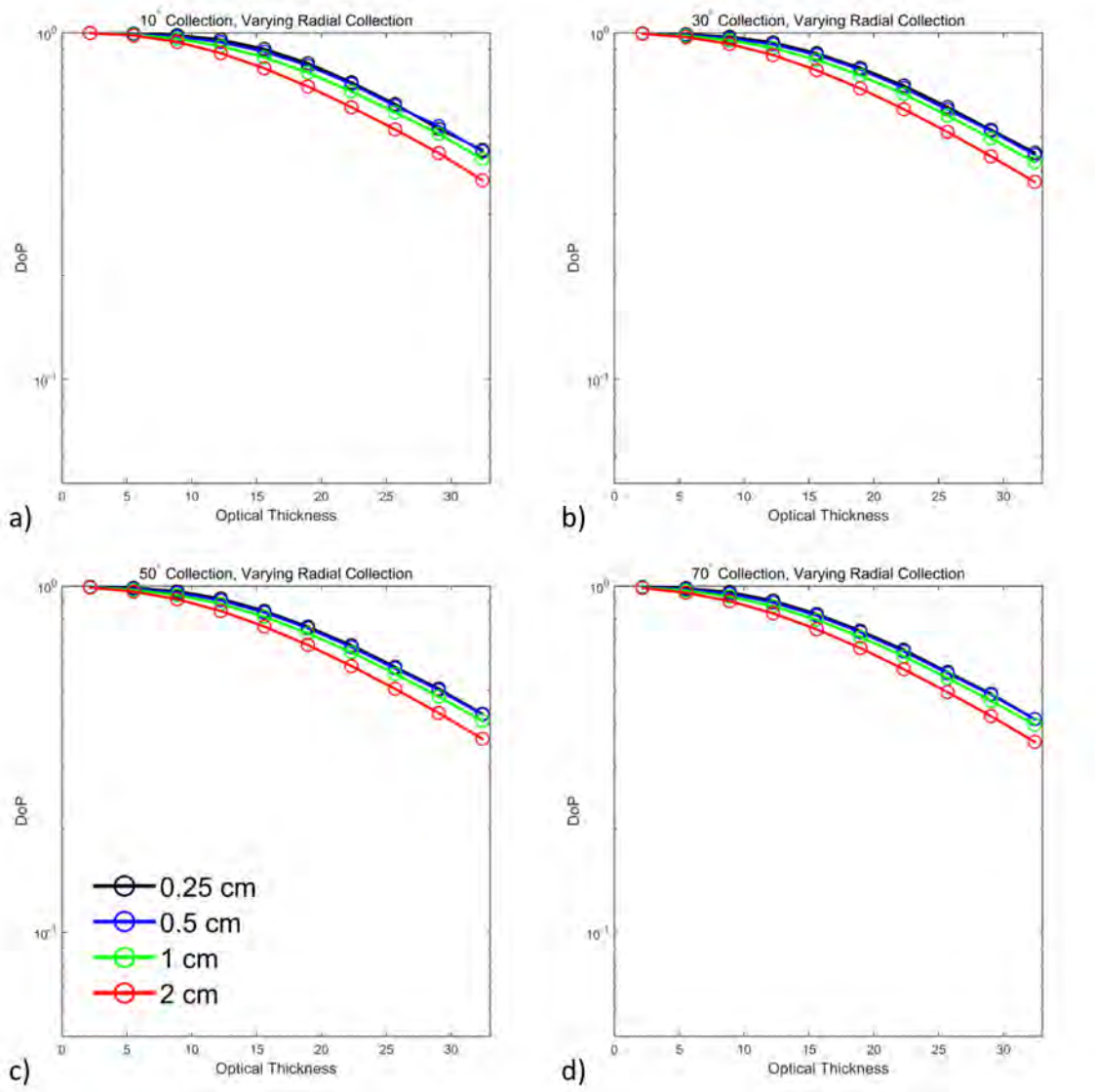

Figure 4.14: *DoP* versus optical thickness changes with variation of the angular and area collection geometry for incident circularly polarized incident light for a scattering environment of 1.925 micron polystyrene microspheres in water. Radial area collection variation from 0.25 to 2 cm on the output face for a) 10 degree half angle collection, b) 30 degree half angle collection, c) 50 degree half angle collection, and d) 70 degree half angle collection.

4.8 Summary

For the forward-scattering environments of 0.99 and 1.925 micron particle diameters, circular polarization maintains its DoP through increasing optical thickness better than linear polarization. The opposite is true for the isotropically scattering (Rayleigh regime) environment of 0.0824 micron particle diameter. This is shown in measurements made through scattering environments of polystyrene microspheres in water with an illuminating wavelength of 543.5 nm. Experimental results show the same trend seen in simulations of the same environments. I hypothesize the limited extent of the experiment's cuvette volume as compared to the simulation's infinite lateral extent can account for the difference between measured DoP and simulated DoP values. This hypothesis is further quantified in simulation for varying collection geometries. The DoP for both linear and circular polarization is susceptible to collection geometry variation in the isotropically scattering (Rayleigh regime) environment. Similar susceptibilities are shown for linear polarization in the forward-scattering environments, but the effect is smaller. Uniquely, circular polarization is nearly unaffected by variations in collection geometry for the forward-scattering environments. Circular polarization proves to be more tolerant of variations in angular and area collection compared to linear polarization, making it ideal and flexible for use in optical sensing systems. Overall, despite variations from the size of the cuvette, circular polarization persists longer than linear polarization for forward-scattering environments.

The following chapter will investigate this increased persistence in detail, specifically addressing the evolution of the polarization states in isotropic and forward-

scattering environments.

CHAPTER 5

Evolution of Circular and Linear Polarization in Scattering Environments

This chapter includes original research in the process of being published in a journal article [102]. The focus of this chapter will be on the results after 1, 2, and 10 scattering events presented in the journal article, but the results after 5, 15 and 20 scattering events will also be added here. The addition of these plots facilitate a clearer presentation of the evolution of the polarization states.

This chapter presents simulation results showing the evolution of polarized light in scattering environments of forward and isotropically (Rayleigh regime) scattering particles. In particular, this work shows circularly polarized light exhibits superior persistence for forward-scattering particle environments. Circularly polarized light's increased persistence compared to linearly polarized light, often called polarization memory, is of importance for many sensing techniques in scattering environments but until now this scattering evolution has not been detailed. In this work, the evolution of circularly and linearly polarized light as it scatters throughout a variety of scattering environments is fully investigated.

The use of polarized light in scattering environments has been of increasing interest in recent years. The difference between circularly and linearly polarized light's interactions in scattering environments is of particular interest. Previous research has shown benefits for the use of both linear and circular polarization for sensing

in specific scattering environments, often showing increased performance benefits for circularly polarized techniques [17, 18, 24, 28, 33, 60]. Previous work has focused on isolated visible wavelengths and underwater scattering environments. I recently published unique simulation results showing superior persistence for circular polarization versus linear polarization in scattering environments of fog and dust over broad wavelength ranges at infrared wavelengths [87, 88, 97]. Sensing in scattering environments utilizing polarization relies on the polarization persistence, or polarization memory, of the light. The mechanism of circular polarization's increased persistence has been theoretically hypothesized; it is proposed that circular polarization depolarizes due to the randomization of the photon's direction and the randomization of the helicity [61, 62]. Xu and Alfano find the benefits for circular polarization are largest for large particles with refractive indices close to the air environment (refractive index ~ 1) and for small, high-index contrast particles (refractive indices between 1.5 and 2) [62]. This work as well as Bicout *et al.*'s preceding work focus on the analytical uncoiling length and circular depolarization length as their metrics [20]. These works do not present how polarized light evolves in scattering environments leading to this increased persistence for circular polarization.

A number of groups have investigated the temporal evolution of polarized light pulses in scattering environments. Ishimaru *et al.* performed simulations for polarized pulses of light incident on a slab of latex scattering particles in water for an angularly limited exit beam at a wavelength of 0.53 microns [30]. The solution's size distribution was nearly monodisperse with a mean particle diameter of 2.019 microns. Their results show circular polarized light has a larger DoP over time for

photons exiting the slab into a narrow forward half angle of 3 degrees. As in this work, Ishimaru *et al.* show that the DoP for circularly polarized pulses decreases more gradually than it does for linearly polarized pulses for the forward direction. Ishimaru's work shows circular polarized pulses maintain their DoP longer in time than linearly polarized pulses transmitted through the slab but offers no insight in how or when the polarized states are modified throughout the environment. Kim and Moscoso simulated the temporal variations of backscattered flux for incident circularly polarized pulses [32]. They investigated scattering environments of latex spheres with monodisperse particle distributions of 0.076 microns, 0.189 microns, and 0.303 microns with an illumination wavelength of 633 nm. For the smallest particle size, the dominant backscattered flux is from the opposite handedness circular polarization. For the larger two particle sizes, the initial backscattered state is the opposite handedness but almost immediately the backscattered flux is dominated by the initial incident handedness. Finally, Cai *et al.* show temporal results for simulations of particle diameters of 0.1, 0.213, 0.855, and 8 microns and experiments with particle diameters of 0.213 and 8 microns, all at an illuminating wavelength of 610 nm [35]. They generally conclude that circularly polarized pulsed light, of the same handedness dominates backscattered light when the scattering particles are larger than the incident wavelength. When the scattering particles are smaller than the wavelength the opposite is shown to be the case (Rayleigh regime). These works are all limited to the temporal variation of backscattered light.

To date, no research has examined the evolution of incident polarized light, as a function of scattering event. In this work I present simulation results for scat-

tering environments of polystyrene microspheres in water. Specifically, I look at monodisperse particle distributions with particle diameters of 0.1, 1.0, 2.0, and 3.0 microns at an incident wavelength of 543.5 nm. These parameters correspond to both isotropically (Rayleigh regime) as well as forward-scattering particles. The parameters are representative of radiation and advection fog at infrared wavelengths. This work builds on my recent conference paper which was limited to a single size parameter and did not include the Rayleigh regime results [103]. Monte Carlo simulations, presented here, for these scattering environments illustrate the evolution of circularly and linearly polarized incident light using the Poincaré sphere after successive scattering events throughout the scattering environment. Circular polarization persists through a larger number of scattering events for both forward and backscattered photons for all of the large particle scattering environments. These results quantify circular polarization's smooth and slow degradation as a function of scattering event, compared to linear polarization's abrupt degradation through a scattering environment.

This chapter is organized as follows: Section 2 covers the background of polarization, polarization-tracking Monte Carlo simulations, and the representation of polarization on the Poincaré sphere, Section 3 presents the Monte Carlo simulation results for linearly polarized light scattering in forward and isotropic scattering environments, Section 4 presents Monte Carlo simulation results for circularly polarized light in the isotropic and forward-scattering environments, comparing these results to those presented for linearly polarized light, and Section 5 concludes, showing circular polarization persists superiorly for forward and backscattered photons in all

of the forward-scattering environments.

5.1 Background

As previously discussed in Chapter 2, the fraction of measured light that is purely polarized is the DoP. The DoP is defined in Equation 2.4. The DoP ranges from 0 for completely unpolarized light to 1 for purely polarized light. A Stokes vector with a DoP between 0 and 1 is partially polarized.

Any polarization state can be represented on the Poincaré sphere. The Poincaré sphere is a sphere with the x, y, and z coordinate axes defined by the normalized Stokes parameters. The x axis is defined by the normalized S_1 parameter, the y axis is defined by the normalized S_2 parameter, and the z axis is defined by the normalized S_3 parameter. The axis parameters are all normalized by S_0 so that the radius of the sphere is equal to 1. The surface of the Poincaré sphere defines all the possible purely polarized states. Any state defined inside the surface of the sphere, but not at the origin, is considered a partially polarized state. The center of the sphere, located at the origin, is the location of any completely unpolarized polarization states. The radial location of the polarization state within the sphere is given by the DoP. The Poincaré sphere is shown in Figure 5.1. The axes are labeled with the commonly used descriptor for each of the core polarization states. The positive x axis is labeled as **H** for horizontally linearly polarized. The negative x axis is labeled as **V** for vertically linearly polarized. The positive y axis is labeled **45** for 45 degree linearly polarized, and the negative y axis is labeled **135** for 135 degree linearly polarized. The positive z axis is labeled **R** for right circularly polarized and

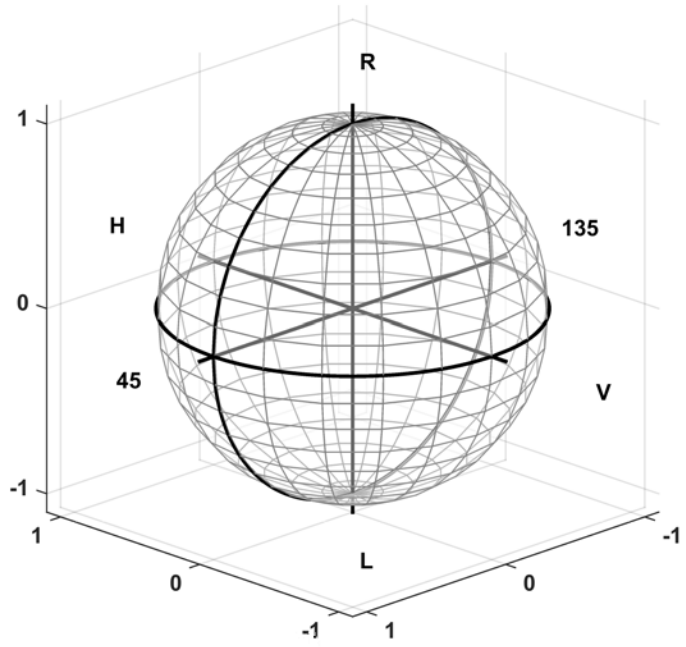

Figure 5.1: The Poincaré Sphere.

the negative z axis is labeled **L** for left circularly polarized. Any polarization state along the equator is a linearly polarized state. As the polarization state moves into either hemisphere it becomes elliptically polarized, and only the **R** and **L** poles represent pure circular polarization states.

The goal of this work is to investigate the evolution of circularly and linearly polarized light's polarization state in scattering environments. To this end, I use a polarization-tracking Monte Carlo program for all the simulation results [82]. Full details of the Monte Carlo program and Mie Theory are previously described in Chapter 2. The simulations propagate one million photons of both linear and circular polarization states perpendicular to the face of a slab of scattering media. Each scattering particle is modeled as a homogenous sphere of defined refractive

index (1.597 for polystyrene). The particle diameters 0.1, 1.0, 2.0, and 3.0 microns and the incident wavelength of 543.5 nm used in these simulations correspond to unitless size parameters 0.77, 7.7, 15.4, and 23.1. Scattering environments with size parameters in these ranges encompass a wide range of natural environments, such as radiation and advection (marine) fog. These particle sizes and the resulting scattering environments cover both isotropically (Rayleigh regime) and forward-scattering situations.

The simulation tracks the location of each photon before and after each scattering event as well as the polarization state of each photon before and after each scattering event. The initial polarization state of the photons is set by an initial Stokes vector. After a scattering event the polarization state of the photon is modified and the Stokes vector is updated. Photons that are scattered to a location further into the scattering slab than the scattering event location are considered forward scattered. Conversely, photons scattered to locations closer to the input face of the slab are considered backscattered. The density of particles for each simulation was such that a sufficient number of scattering events would occur for each incident photon, resulting in an optical thickness of 10 [79, 88].

5.2 **Linearly Polarized Initial Illumination**

The vertical linearly polarized state of the incident photons is plotted on the Poincaré sphere in Figure 5.2. The center of the large orange sphere is located at the position of the initial Stokes state. All one million photons for this polarization state started in this position on the Poincaré sphere.

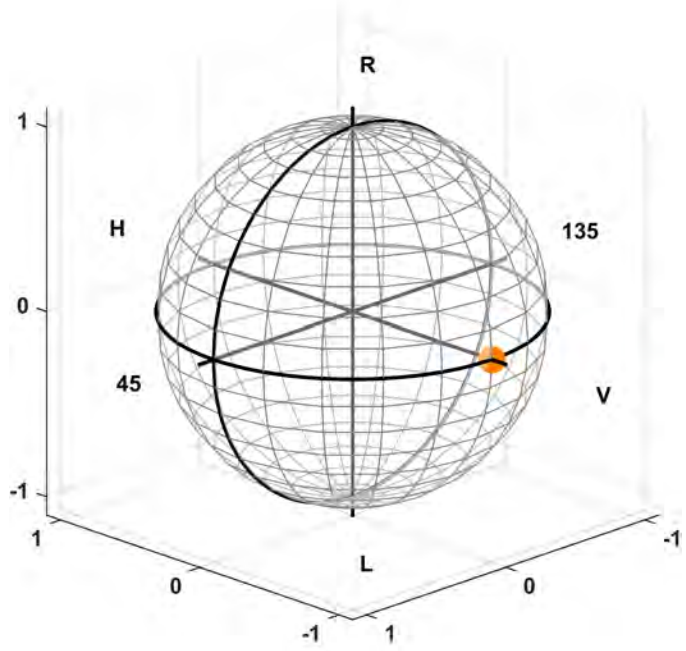

Figure 5.2: Poincaré sphere representation of vertical linearly polarized incident light. (Orange sphere represents location.)

In order to reduce the clutter of the plots in the following figures, I choose the first one hundred thousand photons from the incident one million for each plot. Each of the one hundred thousand photon's Stokes parameters is plotted on the Poincaré sphere after a specified number of scattering events. If the photon is scattered in the forward direction it is colored red; if it is backscattered it is colored blue. All the photons' Stokes parameters are ultimately transformed into the global reference frame set by the initial slab geometry and the initial polarization states. The following figures illustrate the resulting scattered Stokes parameters after 1, 2, 5, 10, 15, and 20 scattering events. Each individual photon's Stokes polarization state is purely polarized, and thus plotted on the surface of the Poincaré sphere. The cumulative Stokes state, for all the forward or backscattered photons of the incident one million photons, is shown as a large sphere in either orange or purple, respectively. The cumulative Stokes state is partially polarized and therefore is inside or very close to the surface of the Poincaré sphere.

The following results are split into two sets: 1) for the forward-scattering particle environments, and 2) for the isotropic (Rayleigh regime) scattering particle environment.

5.2.1 **Forward Scattering Environments: Linear Polarization**

The normalized angular scattering for each particle is shown on the polar plots in Figure 5.3. These plots illustrate the differences between the angular scattering properties of each particle size. The particle is placed at the center of the plot and the plots show how likely it is, for incident radiation from the 180 degree location, to

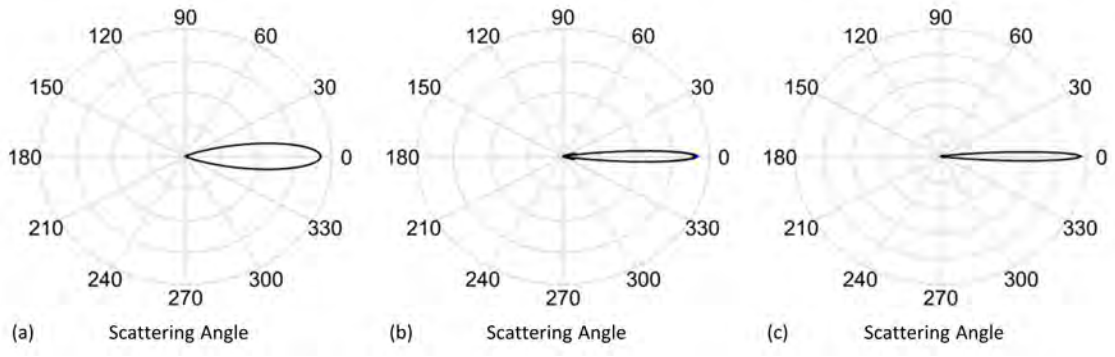

Figure 5.3: Scattering profiles for particle sizes of (a) 1.0 micron, (b) 2.0 microns, and (c) 3.0 microns. Perpendicular and parallel incident polarization states scattering are plotted as black and blue curves. For these forward-scattering particles, the blue and black curves are indistinguishable and the blue curves are not visible on the plots.

scatter at each angle. The scattering from radiation perpendicularly polarized to the page is plotted in solid black; the dashed blue curve corresponds to parallel oriented incident radiation. For these forward-scattering particles, the blue and black curves are nearly indistinguishable and the blue curves are not visible on the plots. As is evident in the plots, the probability to scatter backwards is very small for these environments. Less than 1 percent of all the incident photons are backscattered after any single scattering event for the forward-scattering particle environments.

Figures 5.4 – 5.12 show the results for incident linearly polarized scattered photons after one (a), two (b), five (c), ten (d), fifteen (e) and twenty (f) scattering events for the forward-scattering particle sizes 1.0 micron (Figures 5.4 – 5.6), 2.0 microns (Figures 5.7 – 5.9), and 3.0 microns (Figures 5.10 – 5.12). After one scattering event, forward scattered photons (red) for the particles remain close to the initial location on the Poincaré sphere. The forward scattered photons' cumula-

tive Stokes state (orange) is nearly purely polarized for the each of the particle sizes. The backscattered photons Stokes parameters (blue) are spread around the Poincaré sphere. As the particles size increases more of the backscattered photons gain ellipticity. Although there are more elliptical states for increasing sizes, the cumulative backscattered photons' Stokes state (purple) is highly depolarized and has little to no ellipticity. The resulting cumulative depolarized state still has a small preference for vertical linear polarization but it is close to the origin of the Poincaré sphere. After a single scattering event, vertical linearly polarized light tends to remain nearly purely polarized if forward scattered but is highly depolarized if backscattered. After two scattering events, both forward and backscattered photons' Stokes parameters are spread around the Poincaré sphere more so than after one scattering event. The cumulative forward scattered Stokes state is still highly polarized and remains close to the initial polarization's location. The cumulative backscattered Stokes state is slightly more depolarized than after one scattering event. The forward scattered photons' Stokes parameters spread more around the equator than toward the poles. By ten scattering events the photons' polarization states are highly spread around the Poincaré sphere. The cumulative backscattered state is nearly completely depolarized and is located near the origin, $DoP \approx 0$. The cumulative forward scattered state is not visible but has depolarized and is inside the surface of the Poincaré sphere. The depolarization of the vertical linearly polarized photons tends to spread along the equator more than toward the poles for all particle sizes. Linear polarization depolarizes into other linear states faster and more readily than into elliptical polarization states.

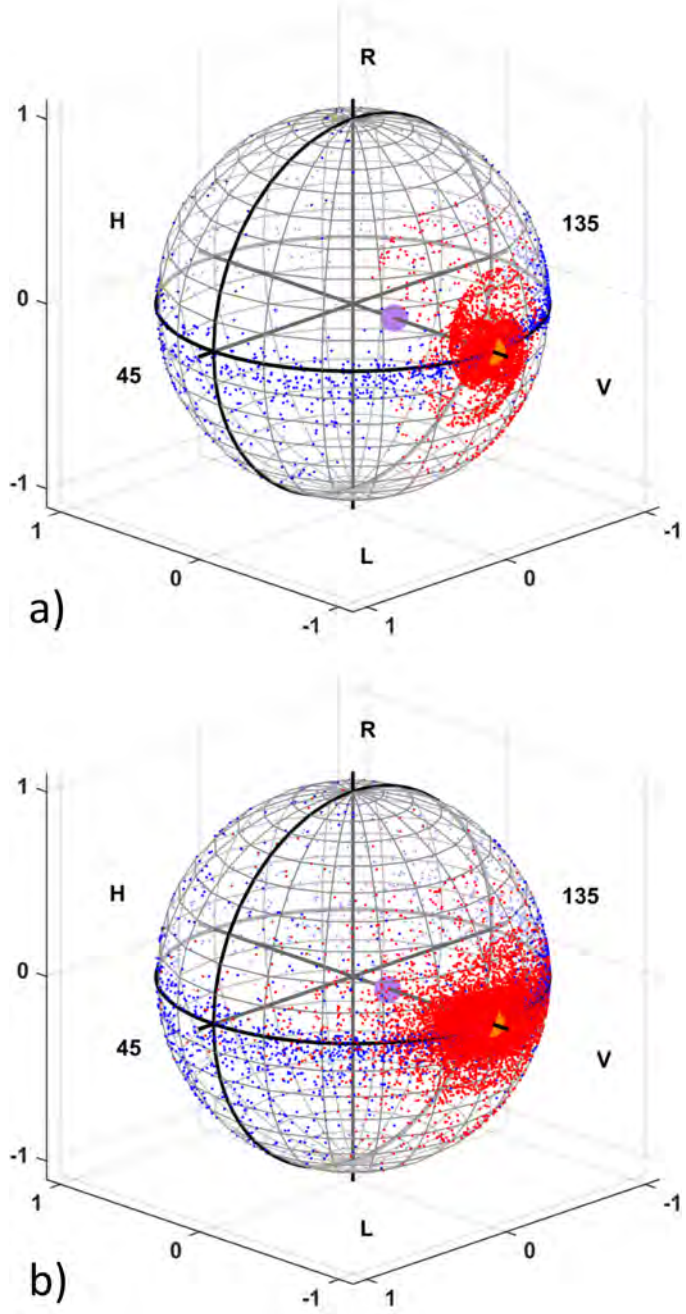

Figure 5.4: Scattered Stokes parameter values for incident linearly polarized light after (a) 1 and (b) 2 scattering events for a scattering environment consisting of particles with diameter 1.0 micron and an illuminating wavelength of 543.5 nm. This figure shows the first 100,000 photons' resulting Stokes parameters after each scattering event; forward scattered photons are shown in red and backscattered photons are shown in blue. The resulting cumulative Stokes state, for the forward or backscattered photons, is shown as large orange or purple spheres.

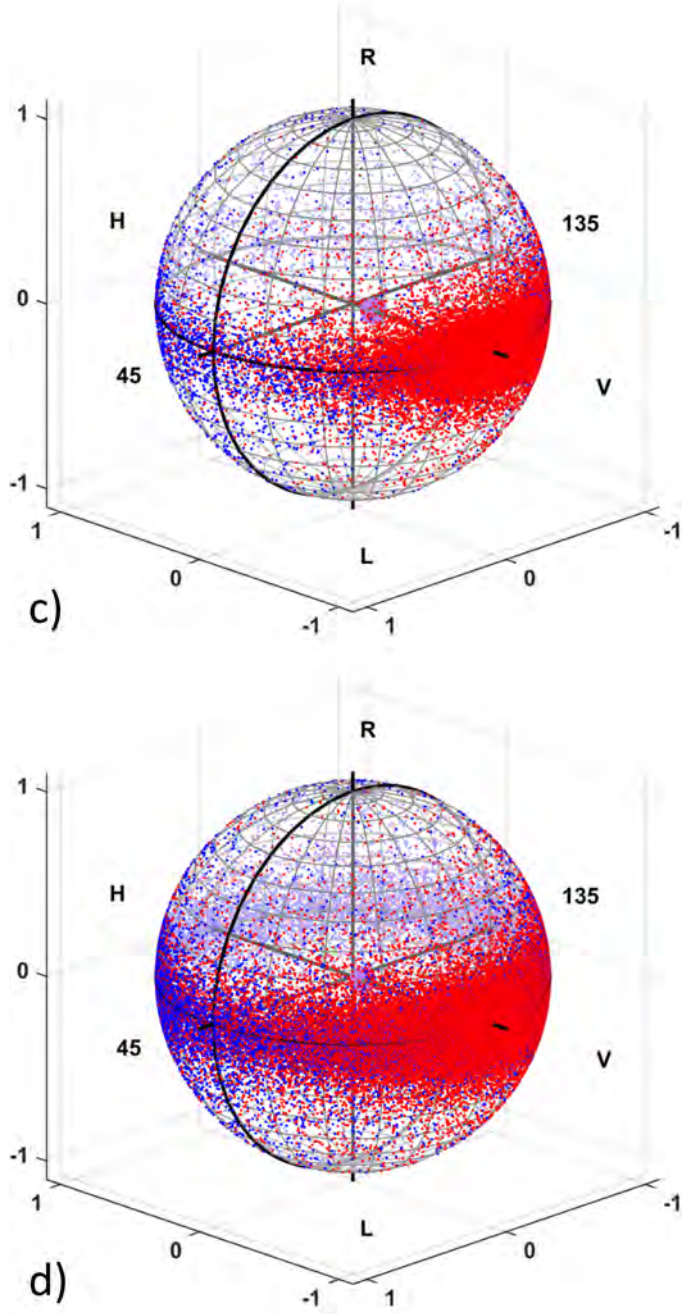

Figure 5.5: Scattered Stokes parameter values for incident linearly polarized light after (c) 5 and (d) 10 scattering events for a scattering environment consisting of particles with diameter 1.0 micron and an illuminating wavelength of 543.5 nm. This figure shows the first 100,000 photons' resulting Stokes parameters after each scattering event; forward scattered photons are shown in red and backscattered photons are shown in blue. The resulting cumulative Stokes state, for the forward or backscattered photons, is shown as large orange or purple spheres.

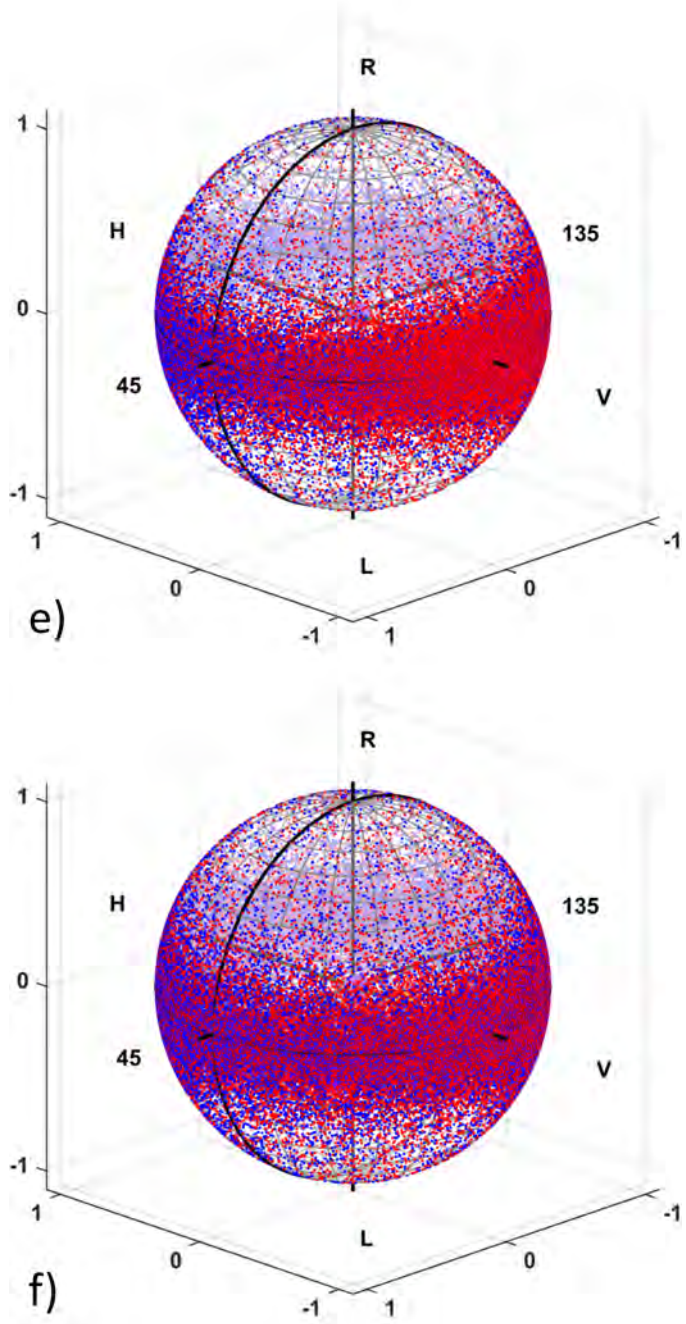

Figure 5.6: Scattered Stokes parameter values for incident linearly polarized light after (e) 15 and (f) 20 scattering events for a scattering environment consisting of particles with diameter 1.0 micron and an illuminating wavelength of 543.5 nm. This figure shows the first 100,000 photons' resulting Stokes parameters after each scattering event; forward scattered photons are shown in red and backscattered photons are shown in blue. The resulting cumulative Stokes state, for the forward or backscattered photons, is shown as large orange or purple spheres.

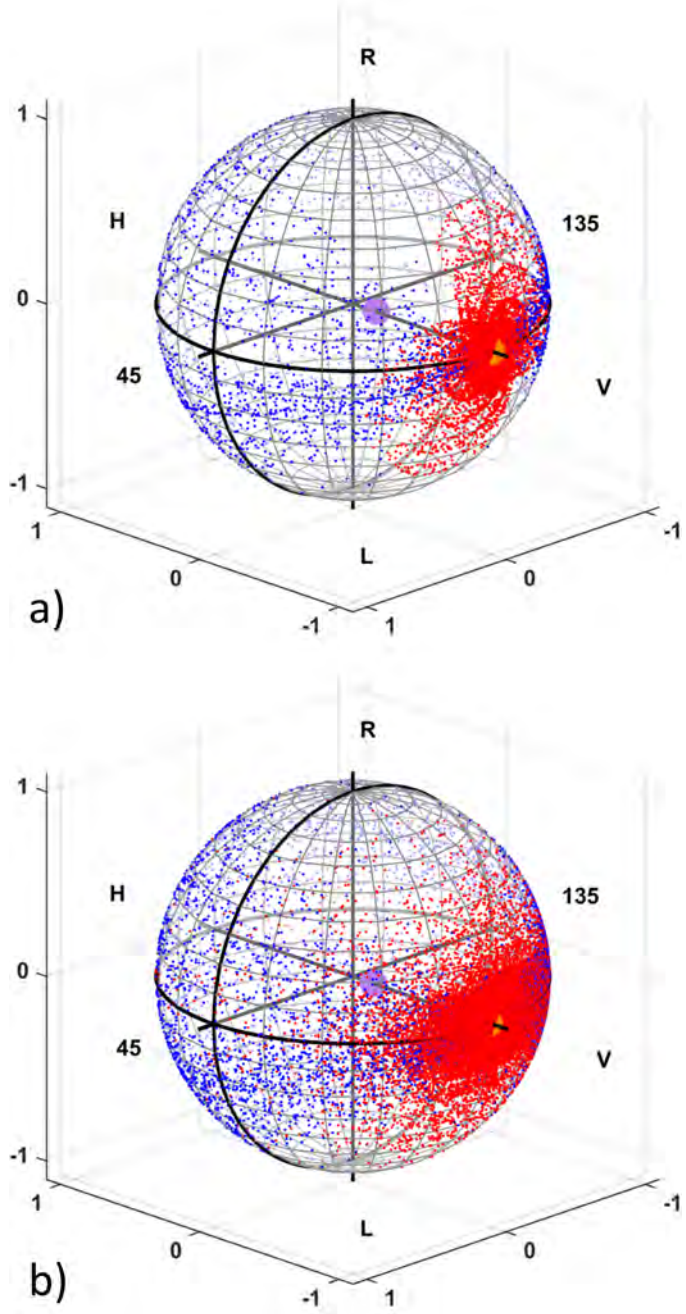

Figure 5.7: Scattered Stokes parameter values for incident linearly polarized light after (a) 1 and (b) 2 scattering events for a scattering environment consisting of particles with diameter 2.0 micron and an illuminating wavelength of 543.5 nm. This figure shows the first 100,000 photons' resulting Stokes parameters after each scattering event; forward scattered photons are shown in red and backscattered photons are shown in blue. The resulting cumulative Stokes state, for the forward or backscattered photons, is shown as large orange or purple spheres.

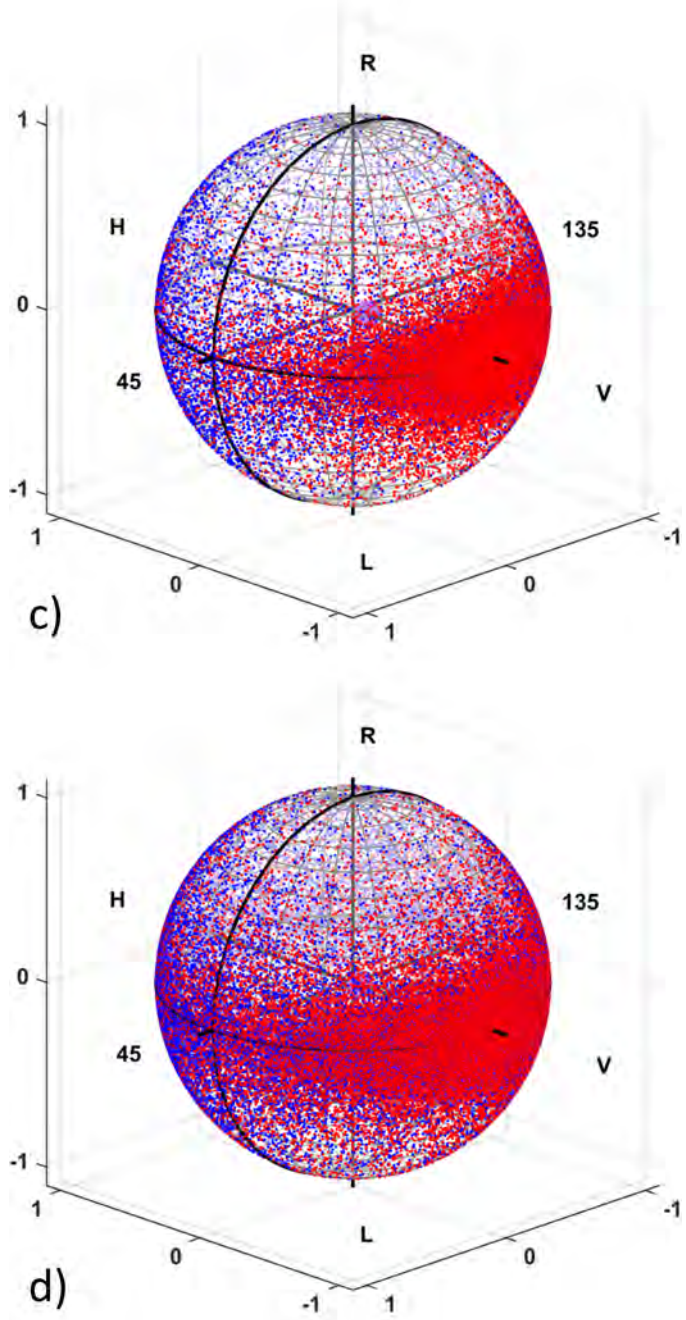

Figure 5.8: Scattered Stokes parameter values for incident linearly polarized light after (c) 5 and (d) 10 scattering events for a scattering environment consisting of particles with diameter 2.0 micron and an illuminating wavelength of 543.5 nm. This figure shows the first 100,000 photons' resulting Stokes parameters after each scattering event; forward scattered photons are shown in red and backscattered photons are shown in blue. The resulting cumulative Stokes state, for the forward or backscattered photons, is shown as large orange or purple spheres.

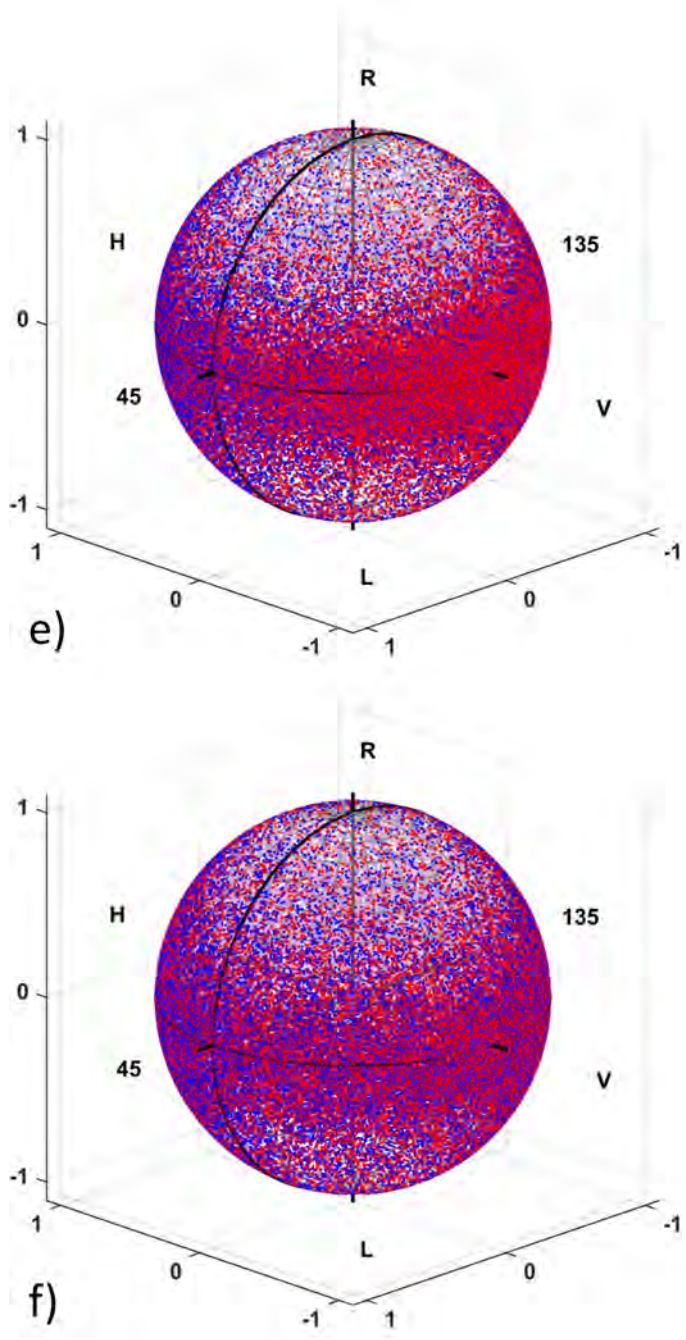

Figure 5.9: Scattered Stokes parameter values for incident linearly polarized light after (e) 15 and (f) 20 scattering events for a scattering environment consisting of particles with diameter 2.0 micron and an illuminating wavelength of 543.5 nm. This figure shows the first 100,000 photons' resulting Stokes parameters after each scattering event; forward scattered photons are shown in red and backscattered photons are shown in blue. The resulting cumulative Stokes state, for the forward or backscattered photons, is shown as large orange or purple spheres.

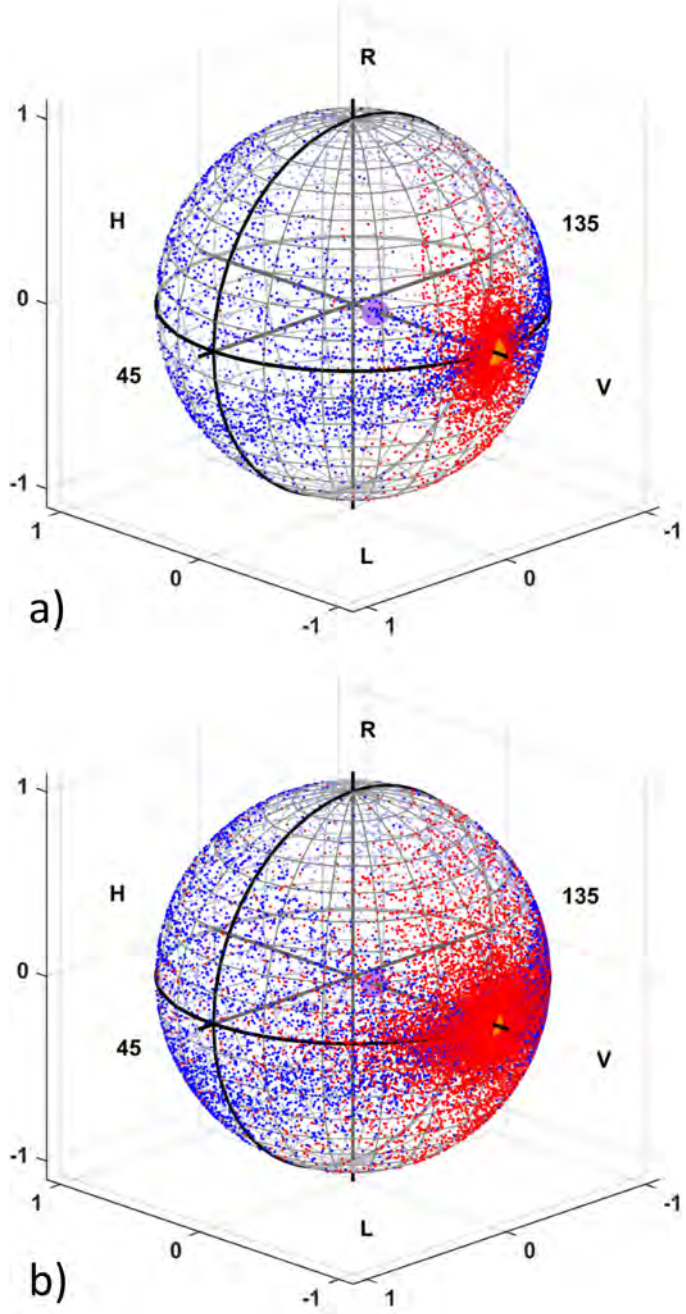

Figure 5.10: Scattered Stokes parameter values for incident linearly polarized light after (a) 1 and (b) 2 scattering events for a scattering environment consisting of particles with diameter 3.0 micron and an illuminating wavelength of 543.5 nm. This figure shows the first 100,000 photons' resulting Stokes parameters after each scattering event; forward scattered photons are shown in red and backscattered photons are shown in blue. The resulting cumulative Stokes state, for the forward or backscattered photons, is shown as large orange or purple spheres.

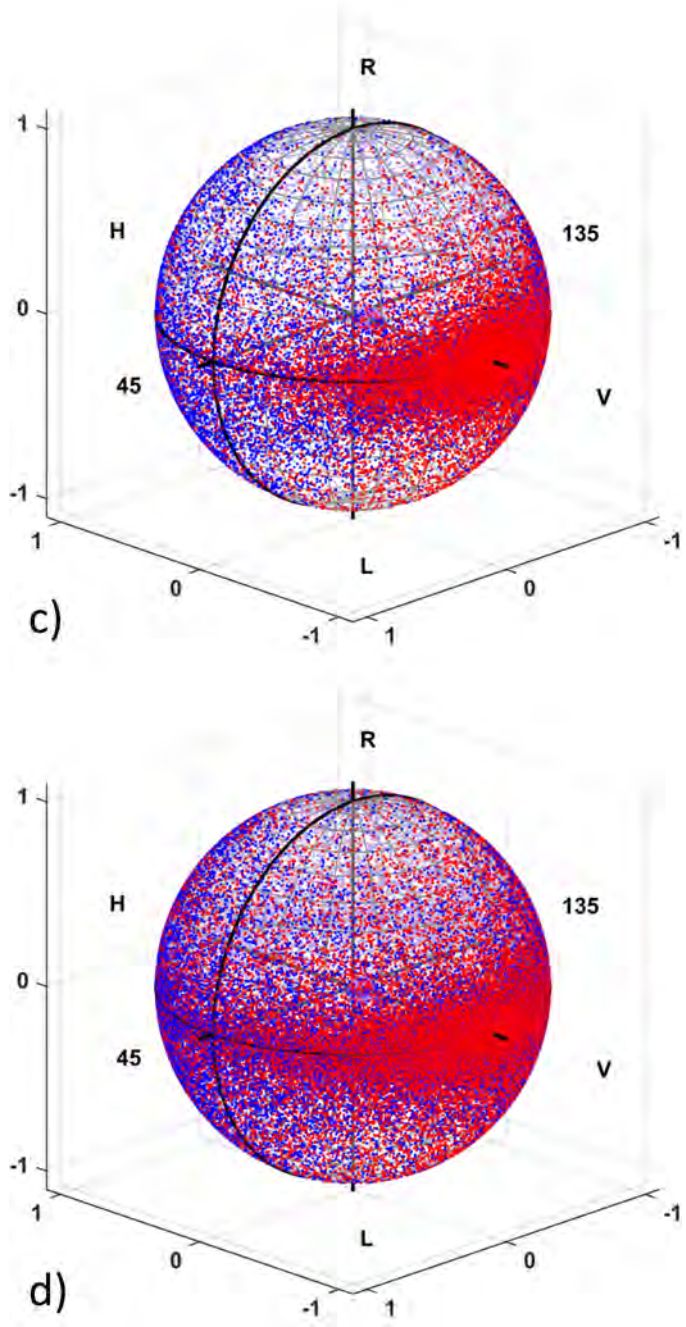

Figure 5.11: Scattered Stokes parameter values for incident linearly polarized light after (c) 5 and (d) 10 scattering events for a scattering environment consisting of particles with diameter 3.0 micron and an illuminating wavelength of 543.5 nm. This figure shows the first 100,000 photons' resulting Stokes parameters after each scattering event; forward scattered photons are shown in red and backscattered photons are shown in blue. The resulting cumulative Stokes state, for the forward or backscattered photons, is shown as large orange or purple spheres.

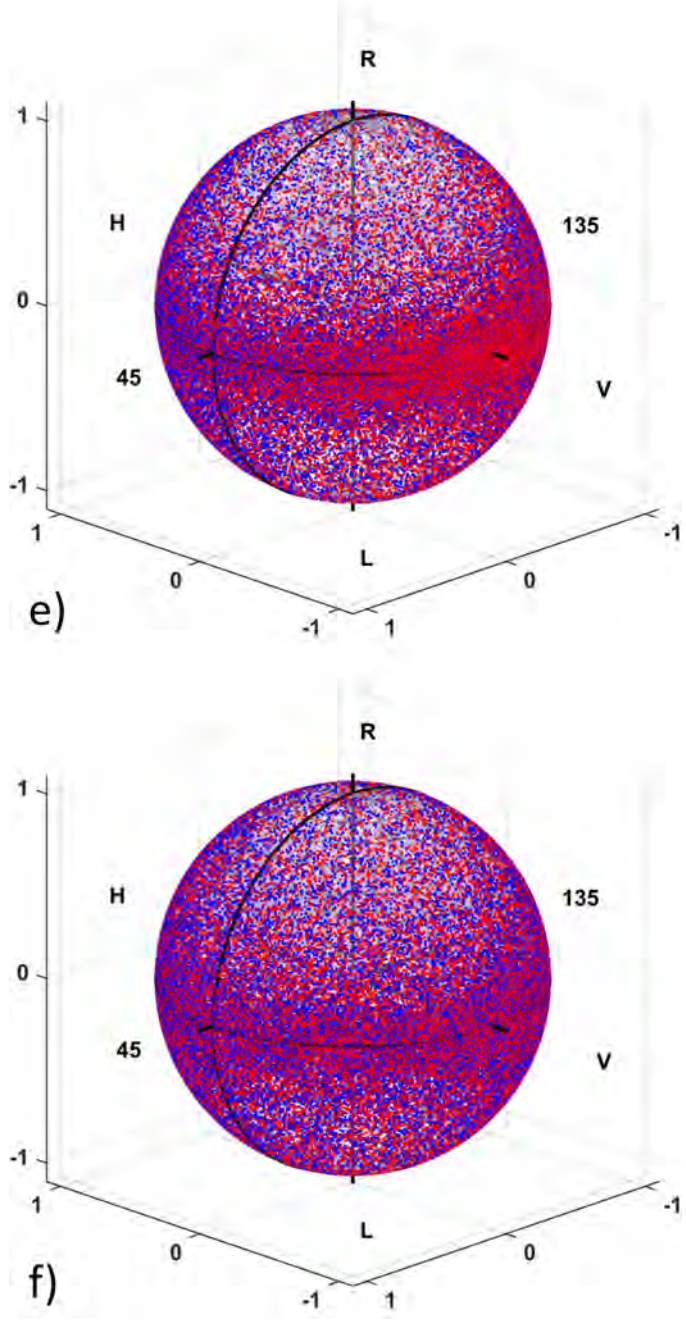

Figure 5.12: Scattered Stokes parameter values for incident linearly polarized light after (e) 15 and (f) 20 scattering events for a scattering environment consisting of particles with diameter 3.0 micron and an illuminating wavelength of 543.5 nm. This figure shows the first 100,000 photons' resulting Stokes parameters after each scattering event; forward scattered photons are shown in red and backscattered photons are shown in blue. The resulting cumulative Stokes state, for the forward or backscattered photons, is shown as large orange or purple spheres.

5.2.2 Isotropically Scattering Environment (Rayleigh Regime): Linear Polarization

The normalized angular scattering for the 0.1 micron particle is shown on the polar plots in Figure 5.13. This plot is similar in design to the plots in Figure 5.3. However, for the isotropic scattering particle, the parallel and perpendicular polarizations scattering are distinct. The isotropic scattering particle has a much larger amount of backscattering compared to the forward scattered particles. After any single scattering event, roughly 42 percent of the incident photons will be backscattered for the isotropically scattering environment.

Figures 5.14 – 5.16 show the results for incident linearly polarized scattered photons after one (a), two (b), five (c), ten (d), fifteen (e) and twenty (f) scattering events for the isotropic scattering particle size 0.1 microns. The results for the isotropic scattering environment are drastically different than the forward-scattering environments. After the first scattering event (a), forward (red) and backscattered (blue) photons remain along the equator of the Poincaré sphere, thus linearly polarized states. The cumulative forward (orange) and backscattered (purple) Stokes states are slightly depolarized for the isotropic scattering environment. Although there appear to be a multitude of states around the equator, the cumulative states show the majority of the scattered photons remain near the initial location on the Poincaré sphere but have moved just inside the surface of the sphere, $DoP < 1$. After two scattering events (b), the photons Stokes parameters remain near the equator but the cumulative forward and backscattered Stokes states are more depolarized and move toward the center of the Poincaré sphere. Both the cumulative forward

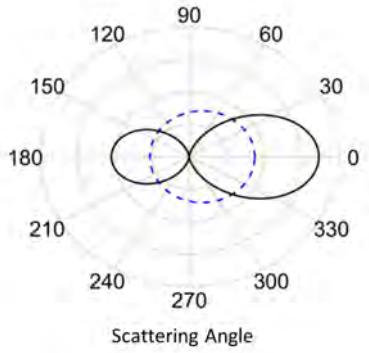

Figure 5.13: Scattering profile for a particle size of 0.1 micron. Perpendicular and parallel incident polarization states scattering are plotted as a solid black and dashed blue curves.

and backscattered Stokes states depolarize along the S_1 axis. After ten scattering events (d), the forward and backscattered states are evenly distributed around the equator of the Poincaré sphere. The cumulative forward and backscattered Stokes state are both at the origin and thus completely depolarized, $DoP \approx 0$.

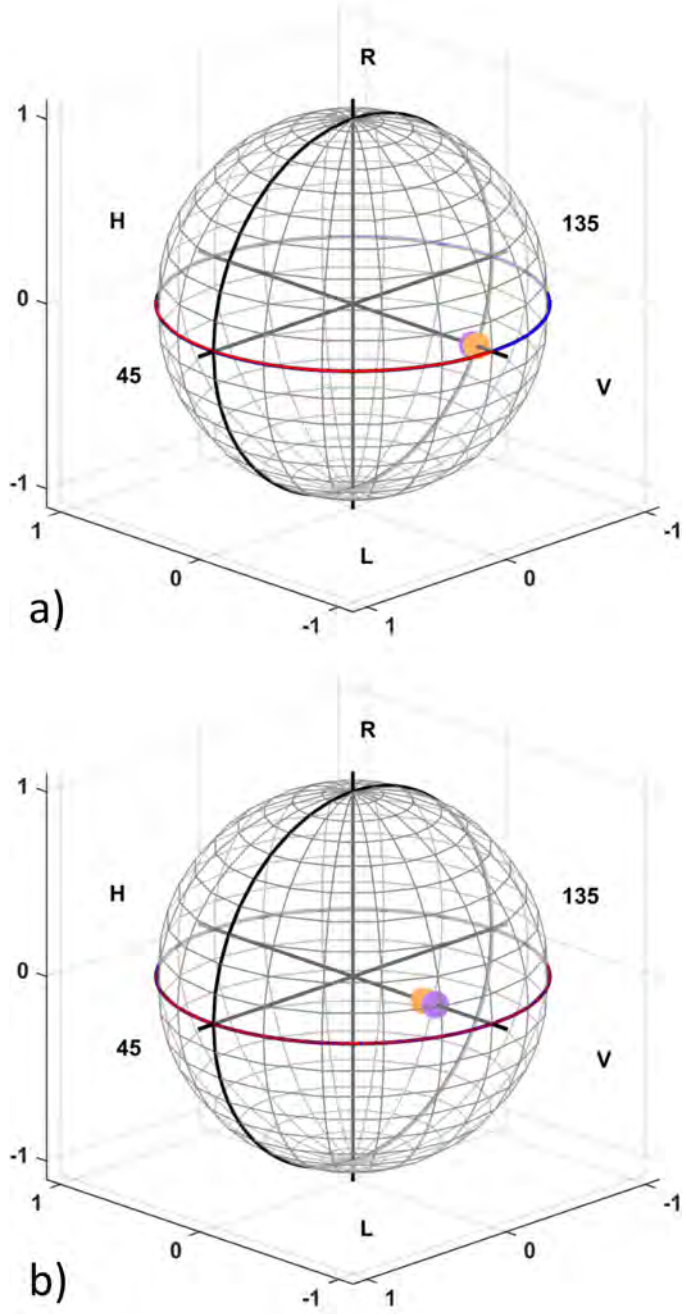

Figure 5.14: Scattered Stokes parameter values for incident linearly polarized light after (a) 1 and (b) 2 scattering events for a scattering environment consisting of particles with diameter 0.1 micron and an illuminating wavelength of 543.5 nm. This figure shows the first 100,000 photons' resulting Stokes parameters after each scattering event; forward scattered photons are shown in red and backscattered photons are shown in blue. The resulting cumulative Stokes state, for the forward or backscattered photons, is shown as large orange or purple spheres.

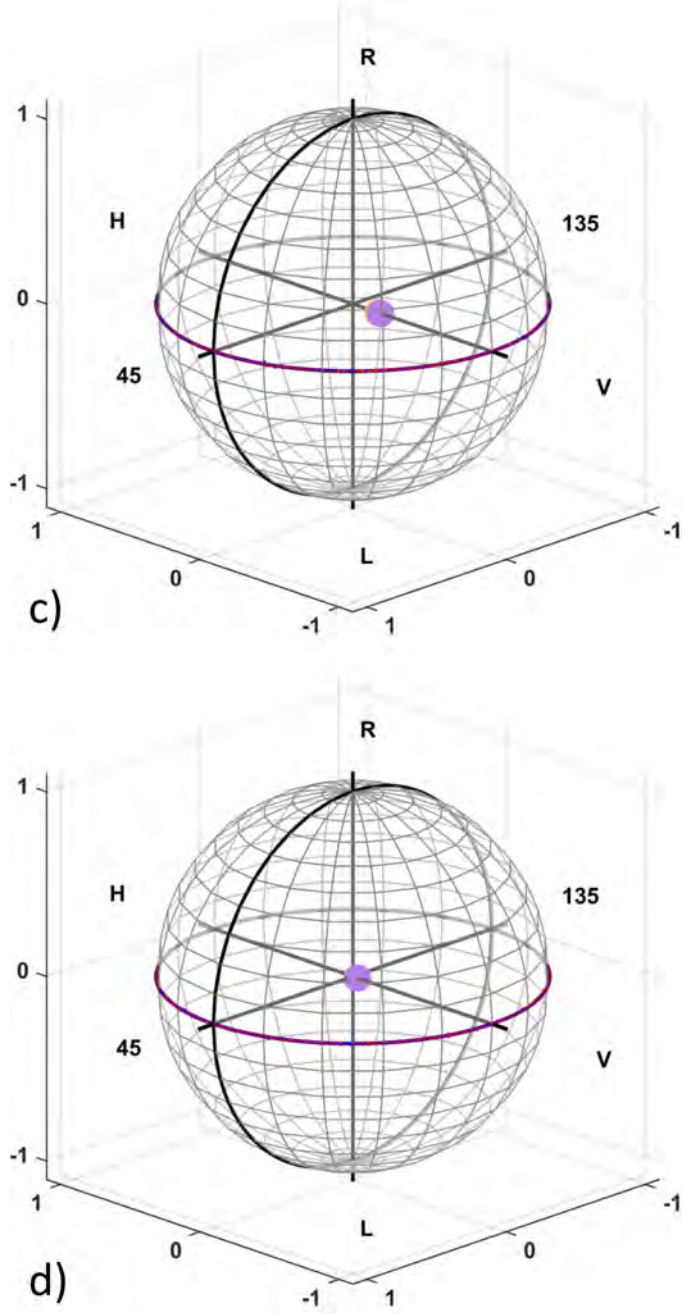

Figure 5.15: Scattered Stokes parameter values for incident linearly polarized light after (c) 5 and (d) 10 scattering events for a scattering environment consisting of particles with diameter 0.1 micron and an illuminating wavelength of 543.5 nm. This figure shows the first 100,000 photons' resulting Stokes parameters after each scattering event; forward scattered photons are shown in red and backscattered photons are shown in blue. The resulting cumulative Stokes state, for the forward or backscattered photons, is shown as large orange or purple spheres.

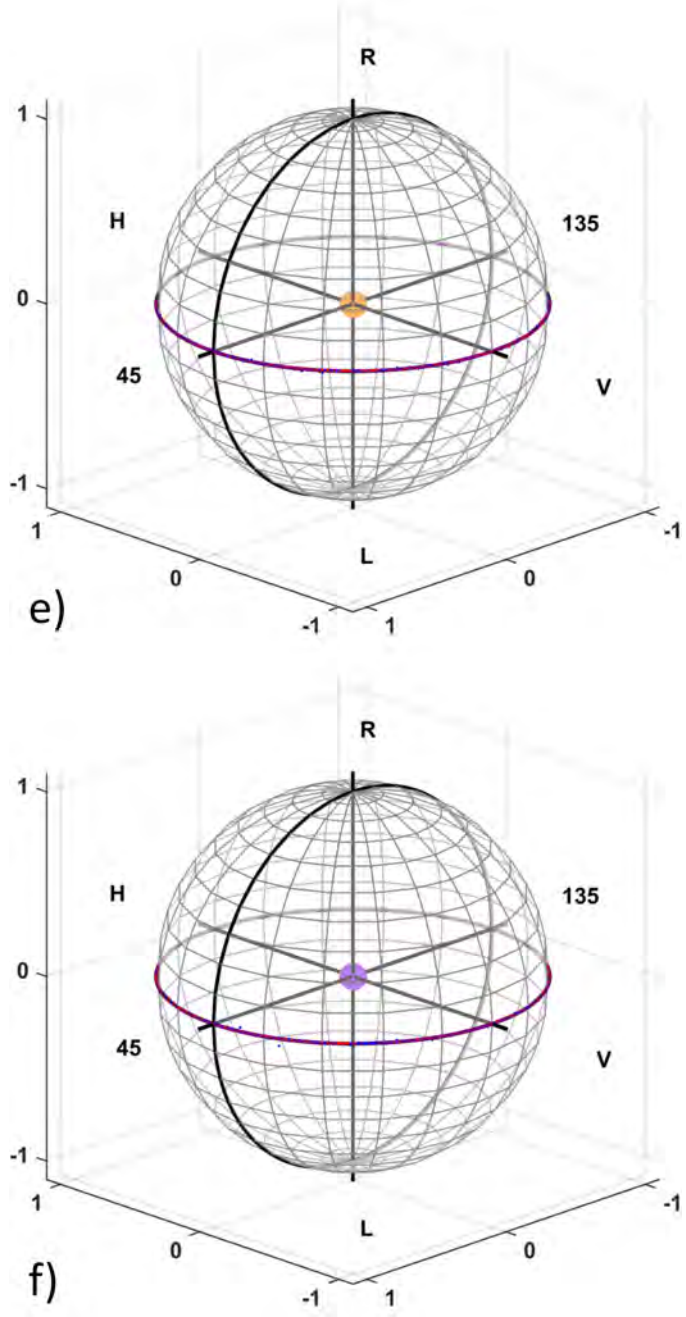

Figure 5.16: Scattered Stokes parameter values for incident linearly polarized light after (e) 15 and (f) 20 scattering events for a scattering environment consisting of particles with diameter 0.1 micron and an illuminating wavelength of 543.5 nm. This figure shows the first 100,000 photons' resulting Stokes parameters after each scattering event; forward scattered photons are shown in red and backscattered photons are shown in blue. The resulting cumulative Stokes state, for the forward or backscattered photons, is shown as large orange or purple spheres.

5.3 Circularly Polarized Initial Illumination

The incident right circularly polarized state for this next set of simulations is located at the positive z axis of the Poincaré sphere. This initial polarization state of the incident photons is plotted on the Poincaré sphere in Figure 5.17. The center of the large orange sphere is located at the position of the initial Stokes state. All one million photons for this polarization state started in this position on the Poincaré sphere.

As in the previous linear polarization case, I chose the first one hundred thousand photons, from the incident one million, for each of the following plots. The same plotting scheme is utilized: red for individual forward scattered photons, blue for individual backscattered photons, the orange sphere represents the cumulative Stokes state for forward scattering, and the purple sphere represents the cumulative Stokes state for backscattering.

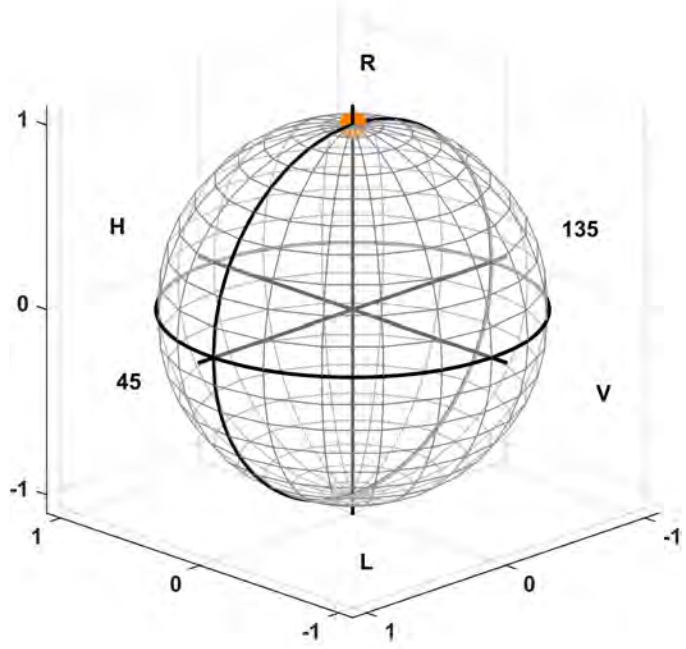

Figure 5.17: Poincaré sphere representation of right circularly polarized incident light. (Orange sphere represents location.)

5.3.1 Isotropically Scattering Environment (Rayleigh Regime): Circular Polarization

Figures 5.18 – 5.20 show the results for incident circularly polarized scattered photons after one (a), two (b), five (c), ten (d), fifteen (e) and twenty (f) scattering events for the isotropic scattering particle size 0.1 micron. After the first scattering event (a), the forward (red) scattered photons maintain their right handedness but are spread around the entire positive S_3 hemisphere. Conversely, the backscattered (blue) photons reverse handedness and spread around the entire negative S_3 hemisphere. Both forward and backscatter states modify to a plethora of polarization states. Although it is not apparent from the plot, the cumulative forward (orange) and backscattered (purple) Stokes states are only somewhat depolarized. The cumulative states are on the S_3 axis but have moved just below the surface of the Poincaré sphere. The backscattered cumulative state has also flipped handedness. After two scattering events (b), the forward and backscattered photons Stokes parameters are intermixed on the entire Poincaré sphere. The forward and backscatter photons are no longer clearly separated by handedness. The cumulative forward and backscattered Stokes states are now highly depolarized. The cumulative forward scattered Stokes state is still right-handed and the cumulative backscattered Stokes state is still left-handed. After ten scattering events (d), both forward and backscattered photons have migrated toward the equator and have lost most of their handedness. The cumulative forward and backscattered Stokes states are completely depolarized and located at the origin, $DoP = 0$. As the number of scattering events increases, circularly polarized photons evolve into a collection of linearly polarized states, re-

sulting in completely depolarized cumulative forward and backscattered states.

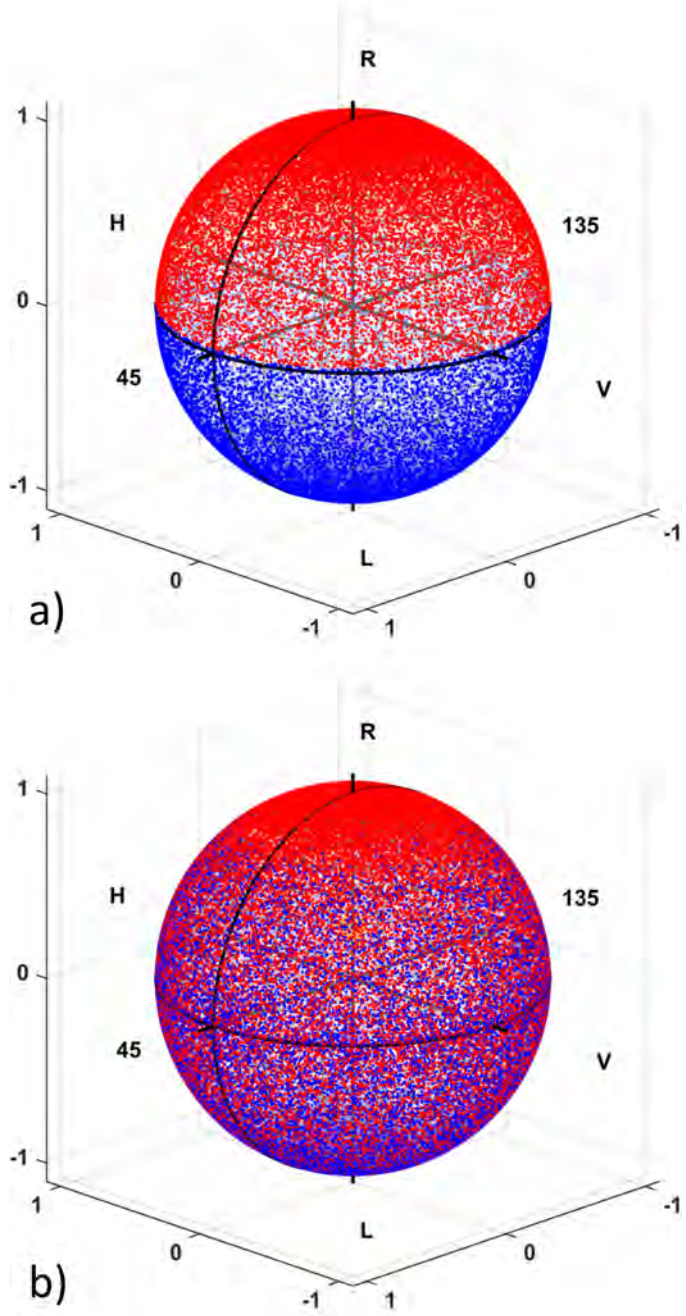

Figure 5.18: Scattered Stokes parameter values for incident circularly polarized light after (a) 1 and (b) 2 scattering events for a scattering environment consisting of particles with diameter 0.1 micron and an illuminating wavelength of 543.5 nm. This figure shows the first 100,000 photons' resulting Stokes parameters after each scattering event; forward scattered photons are shown in red and backscattered photons are shown in blue. The resulting cumulative Stokes state, for the forward or backscattered photons, is shown as large orange or purple spheres.

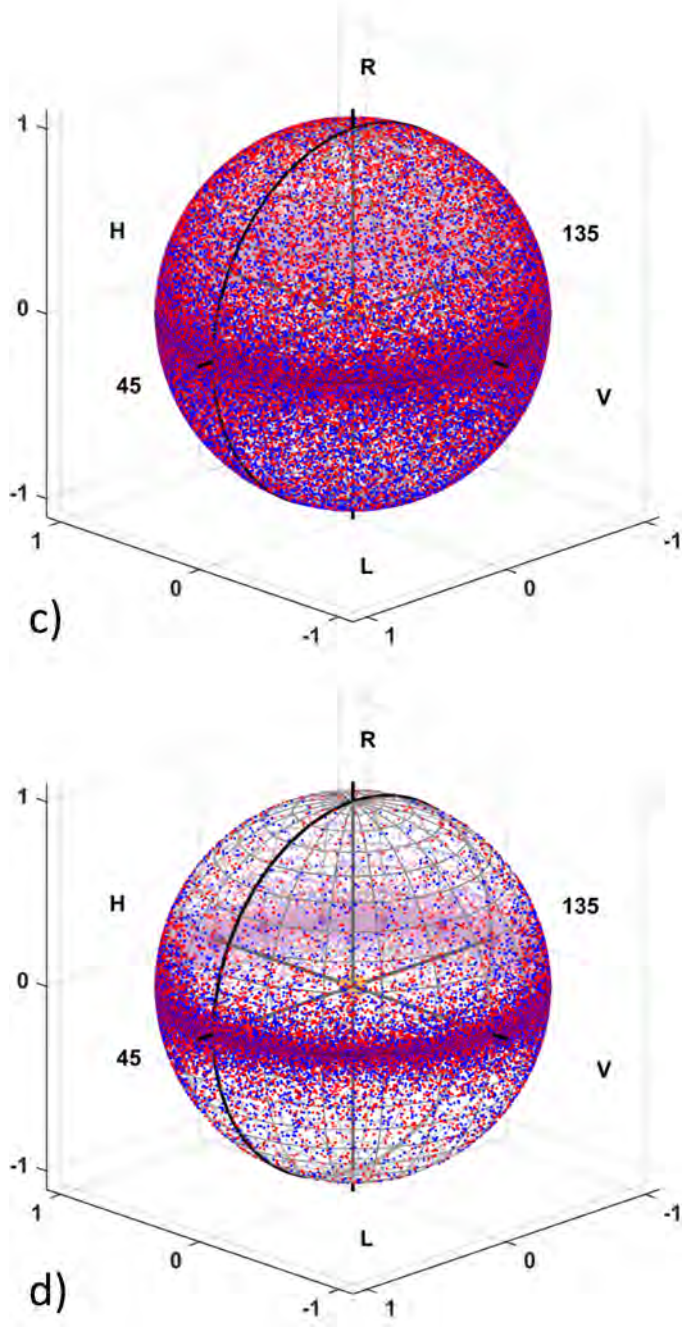

Figure 5.19: Scattered Stokes parameter values for incident circularly polarized light after (c) 5 and (d) 10 scattering events for a scattering environment consisting of particles with diameter 0.1 micron and an illuminating wavelength of 543.5 nm. This figure shows the first 100,000 photons' resulting Stokes parameters after each scattering event; forward scattered photons are shown in red and backscattered photons are shown in blue. The resulting cumulative Stokes state, for the forward or backscattered photons, is shown as large orange or purple spheres.

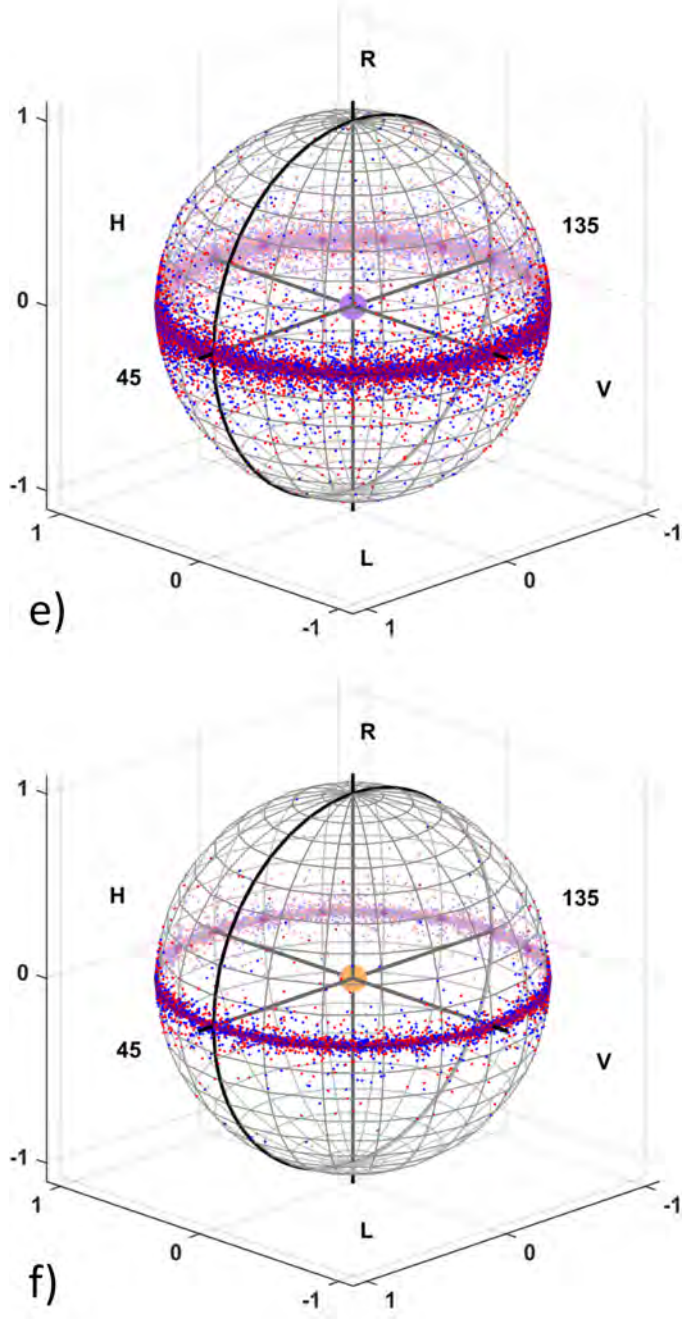

Figure 5.20: Scattered Stokes parameter values for incident circularly polarized light after (e) 15 and (f) 20 scattering events for a scattering environment consisting of particles with diameter 0.1 micron and an illuminating wavelength of 543.5 nm. This figure shows the first 100,000 photons' resulting Stokes parameters after each scattering event; forward scattered photons are shown in red and backscattered photons are shown in blue. The resulting cumulative Stokes state, for the forward or backscattered photons, is shown as large orange or purple spheres.

The plots in Figures 5.14 – 5.16 and Figures 5.18 – 5.20 show linear and circular polarization's modification due to the isotropically scattering environment after individual scattering events. The evolution of the cumulative forward and backscattered DoP plots, as a function of scattering event, are shown in Figure 5.21.

The initial DoP for forward or backscattered photons in this plot is set to 1. Even though linear polarization is superior for this isotropic scattering environment, both linear and circular forward and backscattered photons depolarize rapidly as a function of scattering event. Circularly polarized light is completely depolarized after merely eight scattering events while linear polarization is completely depolarized after fourteen scattering events.

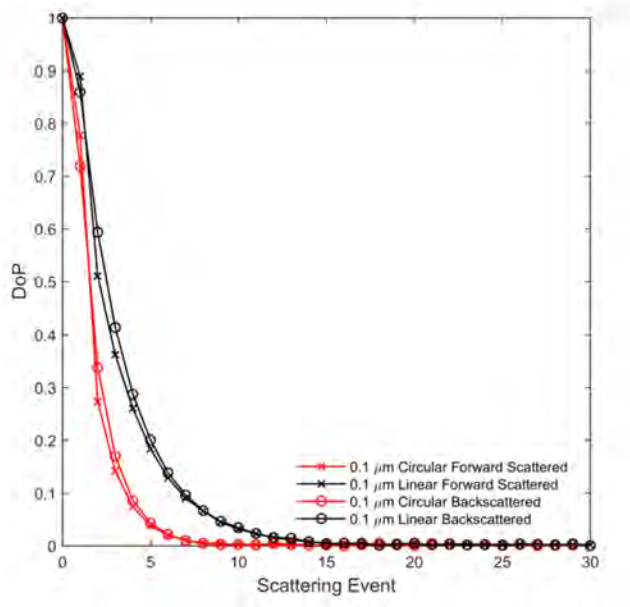

Figure 5.21: Cumulative DoP, for forward (x's) and backscattered (o's) photons, from circularly (red) and linearly (black) polarized incident polarization states versus number of scattering events. Both linear and circular forward and backscattered photons depolarize rapidly as a function of scattering event. Circularly polarized light is completely depolarized after merely eight scattering events while linear polarization is completely depolarized after fourteen scattering events.

5.3.2 **Forward Scattering Environments: Circular Polarization**

Figures 5.22 – 5.30 show the results for incident circularly polarized scattered photons after one (a), two (b), five (c), ten (d), fifteen (e) and twenty (f) scattering events for the forward-scattering particle sizes 1.0 micron (Figures 5.22 – 5.24), 2.0 microns (Figures 5.25 – 5.27), and 3.0 microns (Figures 5.28 – 5.30). The forward-scattering environments for both the linear as well as circular incident polarizations exhibit a very different behavior than the isotropic case. For this incident circular polarization, after the first scattering event (a), forward scattered photons remain close to their initial pole location on the Poincaré sphere. The forward scattered photons' cumulative Stokes state is nearly purely polarized. The backscattered photons Stokes parameters are spread out around the Poincaré sphere more than the forward scattered photons, but the Stokes parameters remain in the same handedness. The resulting cumulative backscattered Stokes state is depolarizing. Circularly polarized light tends to remain nearly purely polarized if forward scattered but is slightly depolarized if backscattered. Remember that after one scattering event, just over 1 percent of the incident photons are backscattered for each of the forward-scattering particle environments as was illustrated in Figure 5.3. After two scattering events (b), both forward and backscattered photons' Stokes parameters are spread around the Poincaré sphere slightly more so than after one scattering event. The cumulative forward scattered Stokes state is still nearly purely polarized and remains close to the initial polarization's location. The forward scattered photons' Stokes parameters spread down from the **R** pole but still remain in a cap packed near the pole. The cumulative backscattered Stokes state is more polarized than after one scattering

event. Backscattered photons largely maintain right-handed helicity but fill more of the hemisphere than the after one scattering event. After ten scattering events (d), the forward scattered photons' Stokes parameters are still highly polarized and remain in a cap near the **R** circular pole. The backscattered Stokes parameters are spread out more around the upper hemisphere. The cumulative forward scattered Stokes state is highly polarized, and it is located just under the **R** pole cap. The cumulative backscattered Stokes state is also highly polarized. Circularly polarized incident light maintains a high DoP, for both forward and backscattered photons, through a large number of scattering events for the forward-scattering environments.

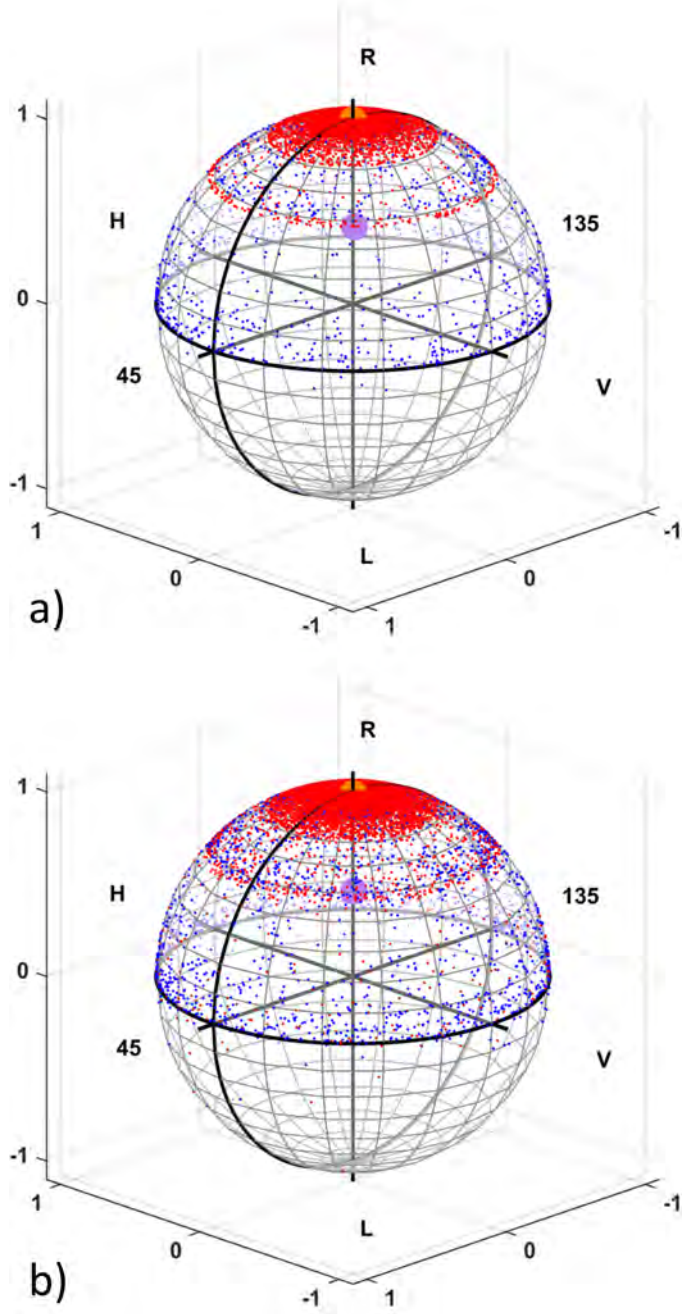

Figure 5.22: Scattered Stokes parameter values for incident circularly polarized light after (a) 1 and (b) 2 scattering events for a scattering environment consisting of particles with diameter 1.0 micron and an illuminating wavelength of 543.5 nm. This figure shows the first 100,000 photons' resulting Stokes parameters after each scattering event; forward scattered photons are shown in red and backscattered photons are shown in blue. The resulting cumulative Stokes state, for the forward or backscattered photons, is shown as large orange or purple spheres.

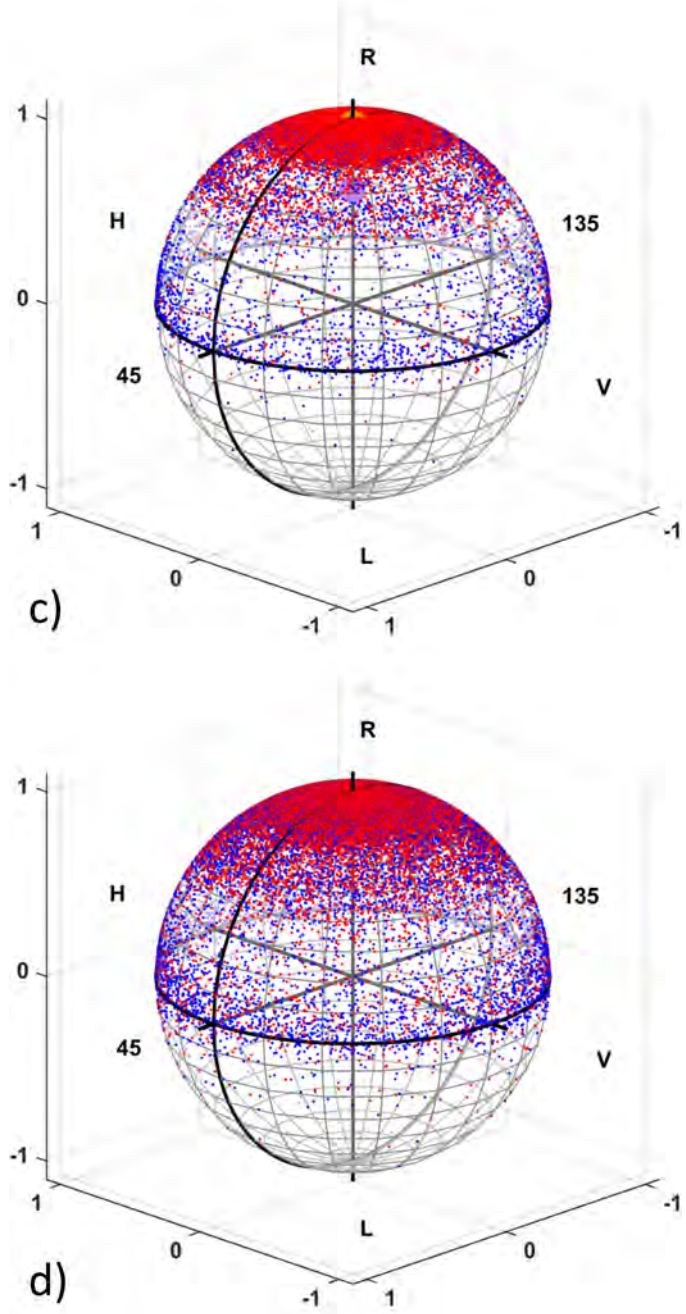

Figure 5.23: Scattered Stokes parameter values for incident circularly polarized light after (c) 5 and (d) 10 scattering events for a scattering environment consisting of particles with diameter 1.0 micron and an illuminating wavelength of 543.5 nm. This figure shows the first 100,000 photons' resulting Stokes parameters after each scattering event; forward scattered photons are shown in red and backscattered photons are shown in blue. The resulting cumulative Stokes state, for the forward or backscattered photons, is shown as large orange or purple spheres.

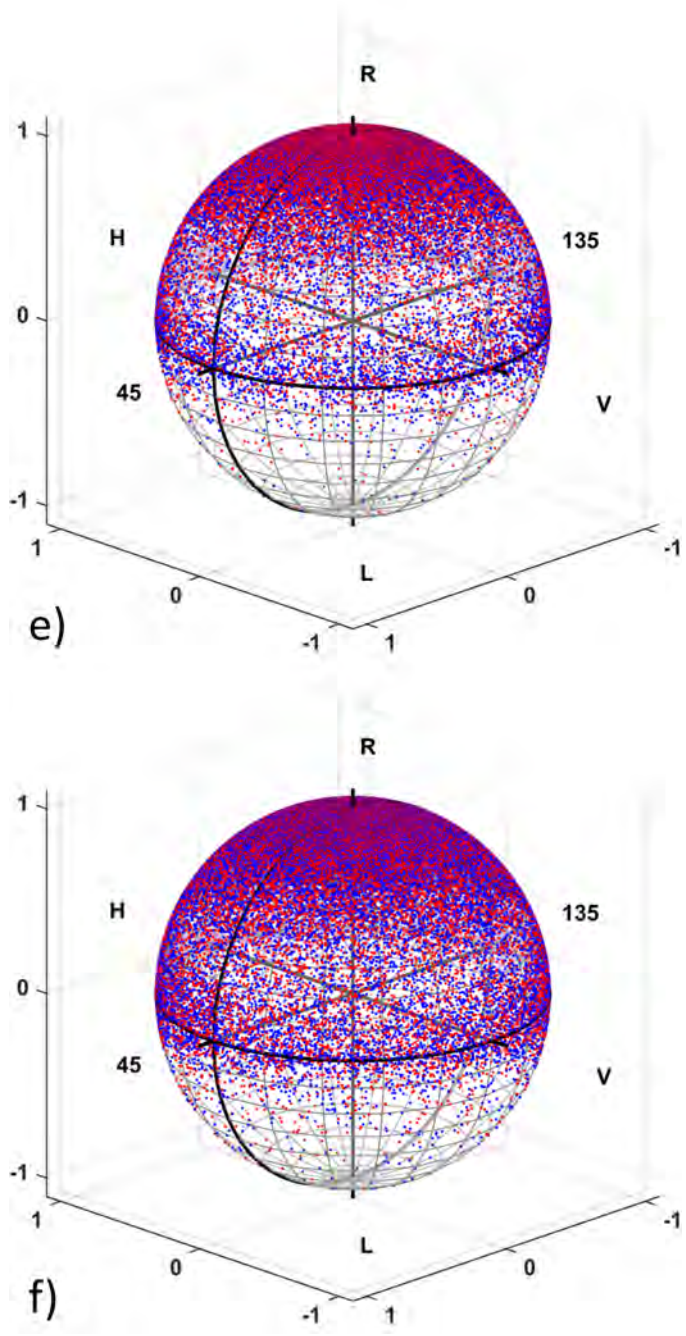

Figure 5.24: Scattered Stokes parameter values for incident circularly polarized light after (e) 15 and (f) 20 scattering events for a scattering environment consisting of particles with diameter 1.0 micron and an illuminating wavelength of 543.5 nm. This figure shows the first 100,000 photons' resulting Stokes parameters after each scattering event; forward scattered photons are shown in red and backscattered photons are shown in blue. The resulting cumulative Stokes state, for the forward or backscattered photons, is shown as large orange or purple spheres.

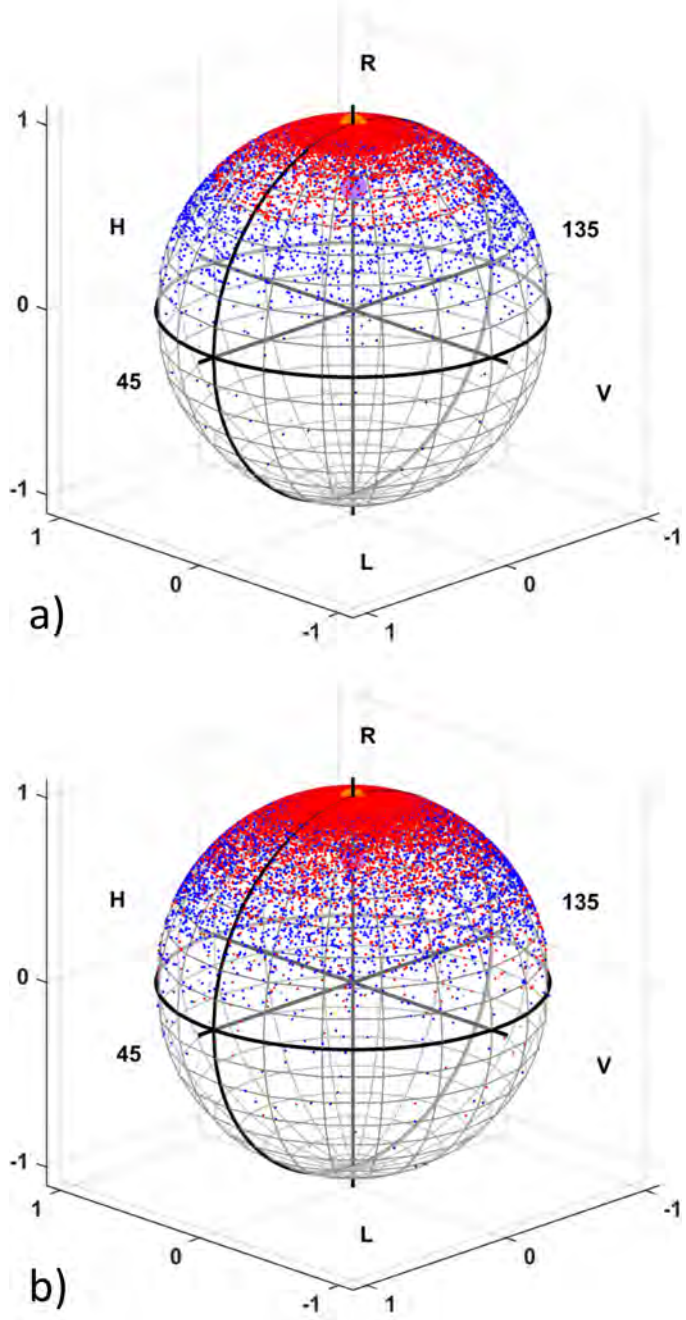

Figure 5.25: Scattered Stokes parameter values for incident circularly polarized light after (a) 1 and (b) 2 scattering events for a scattering environment consisting of particles with diameter 2.0 micron and an illuminating wavelength of 543.5 nm. This figure shows the first 100,000 photons' resulting Stokes parameters after each scattering event; forward scattered photons are shown in red and backscattered photons are shown in blue. The resulting cumulative Stokes state, for the forward or backscattered photons, is shown as large orange or purple spheres.

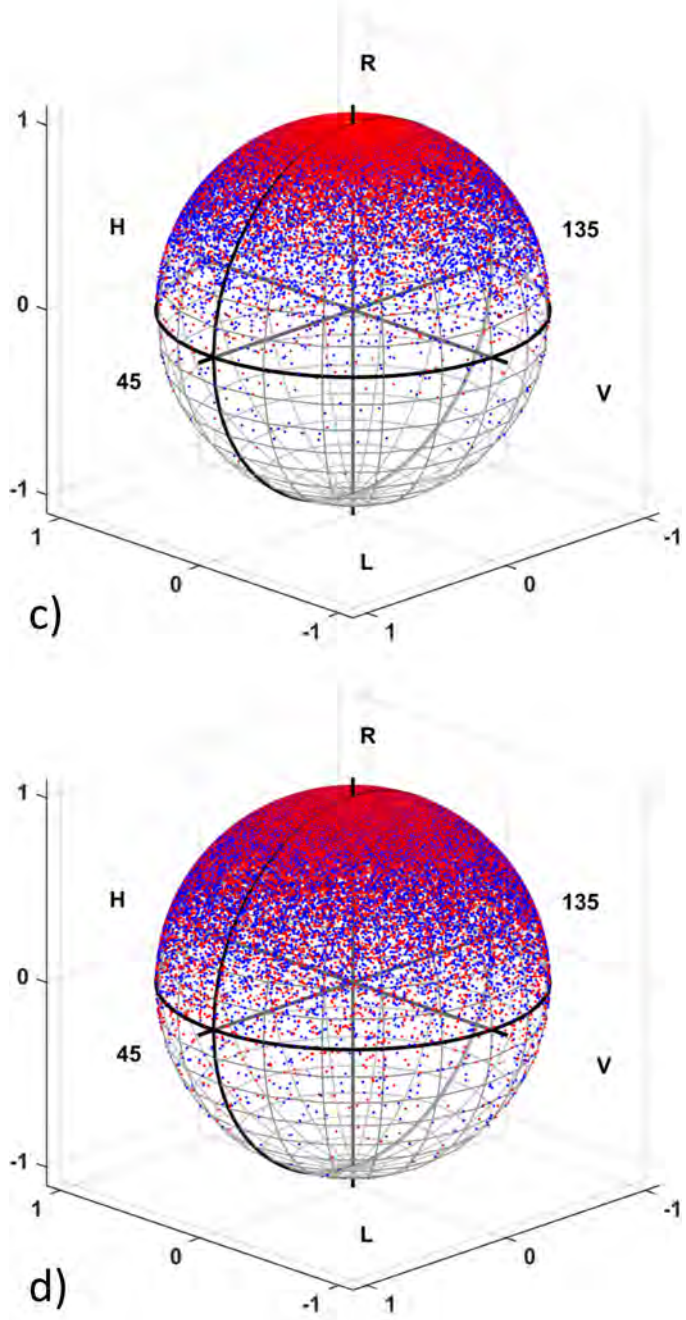

Figure 5.26: Scattered Stokes parameter values for incident circularly polarized light after (c) 5 and (d) 10 scattering events for a scattering environment consisting of particles with diameter 2.0 micron and an illuminating wavelength of 543.5 nm. This figure shows the first 100,000 photons' resulting Stokes parameters after each scattering event; forward scattered photons are shown in red and backscattered photons are shown in blue. The resulting cumulative Stokes state, for the forward or backscattered photons, is shown as large orange or purple spheres.

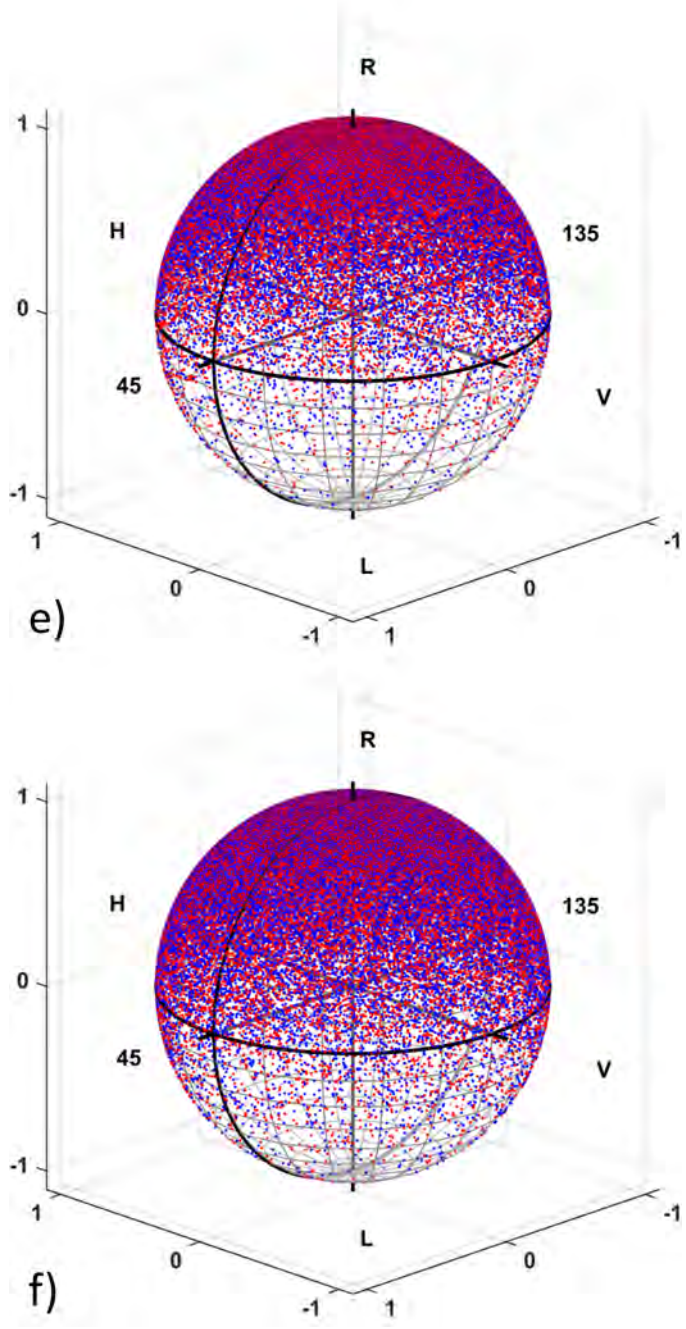

Figure 5.27: Scattered Stokes parameter values for incident circularly polarized light after (e) 15 and (f) 20 scattering events for a scattering environment consisting of particles with diameter 2.0 micron and an illuminating wavelength of 543.5 nm. This figure shows the first 100,000 photons' resulting Stokes parameters after each scattering event; forward scattered photons are shown in red and backscattered photons are shown in blue. The resulting cumulative Stokes state, for the forward or backscattered photons, is shown as large orange or purple spheres.

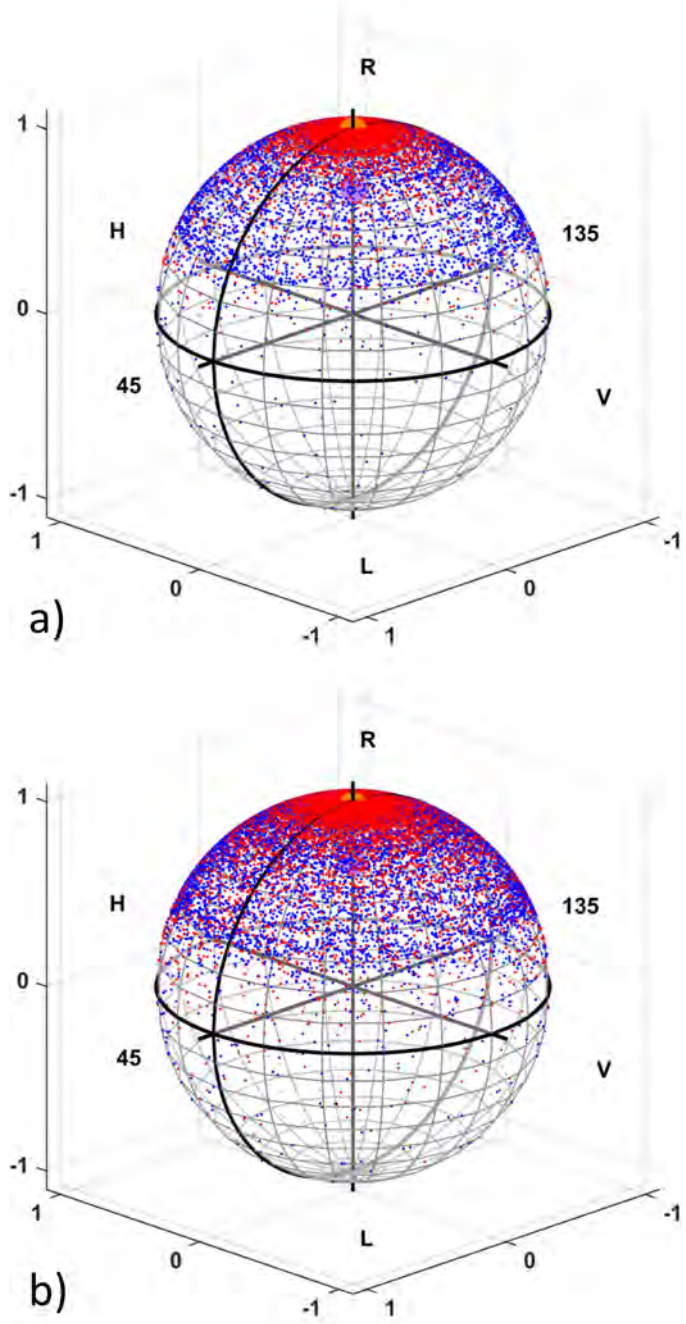

Figure 5.28: Scattered Stokes parameter values for incident circularly polarized light after (a) 1 and (b) 2 scattering events for a scattering environment consisting of particles with diameter 3.0 micron and an illuminating wavelength of 543.5 nm. This figure shows the first 100,000 photons' resulting Stokes parameters after each scattering event; forward scattered photons are shown in red and backscattered photons are shown in blue. The resulting cumulative Stokes state, for the forward or backscattered photons, is shown as large orange or purple spheres.

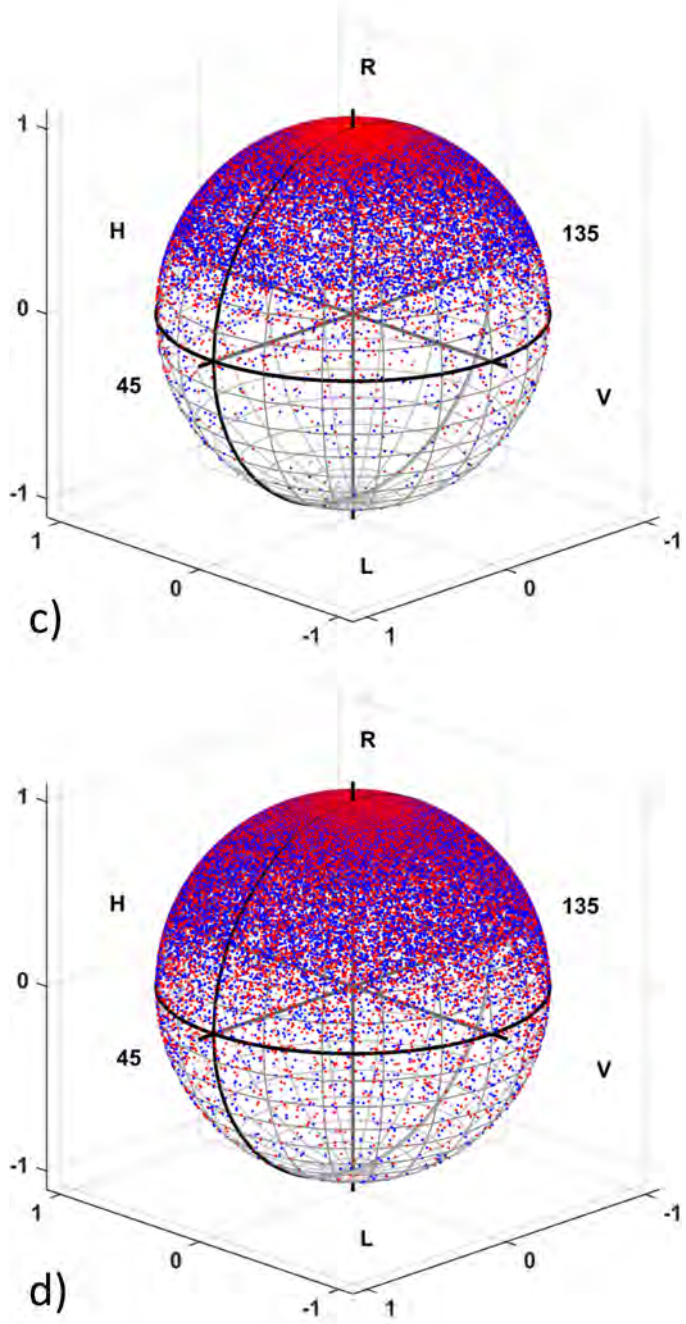

Figure 5.29: Scattered Stokes parameter values for incident circularly polarized light after (c) 5 and (d) 10 scattering events for a scattering environment consisting of particles with diameter 3.0 micron and an illuminating wavelength of 543.5 nm. This figure shows the first 100,000 photons' resulting Stokes parameters after each scattering event; forward scattered photons are shown in red and backscattered photons are shown in blue. The resulting cumulative Stokes state, for the forward or backscattered photons, is shown as large orange or purple spheres.

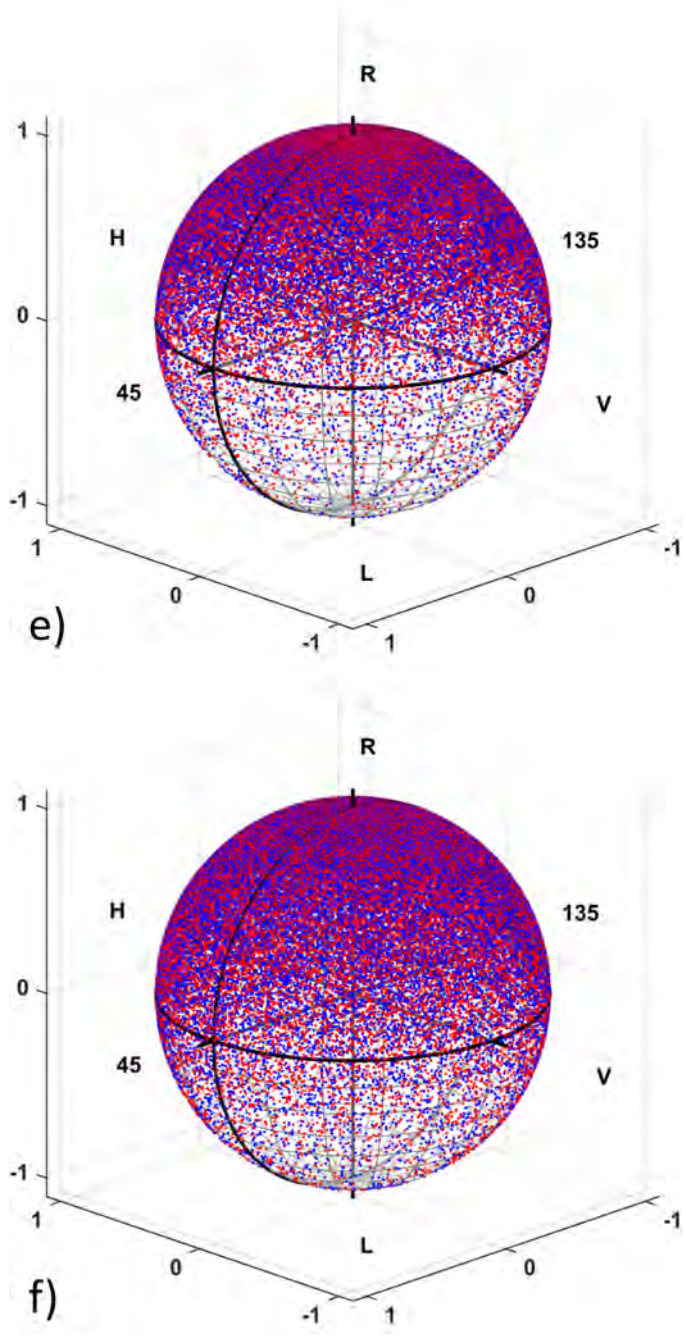

Figure 5.30: Scattered Stokes parameter values for incident circularly polarized light after (e) 15 and (f) 20 scattering events for a scattering environment consisting of particles with diameter 3.0 micron and an illuminating wavelength of 543.5 nm. This figure shows the first 100,000 photons' resulting Stokes parameters after each scattering event; forward scattered photons are shown in red and backscattered photons are shown in blue. The resulting cumulative Stokes state, for the forward or backscattered photons, is shown as large orange or purple spheres.

The plots in Figures 5.4 – 5.12 and Figures 5.22 – 5.30 show linear and circular polarization's modification due to the forward-scattering environments after individual scattering events. The evolution of the cumulative forward and backscattered DoP plots, as a function of scattering event, are shown in Figure 5.31.

In the forward-scattering environments (as opposed to the Rayleigh regime) the following results are quantified. Figure 5.31 clearly shows that circular polarization maintains its DoP better than linear and thus persists through increasing scattering events for either forward or backscattered photons. The initial DoP for forward or backscattered photons is set to 1. In Figure 5.31 (a), backscattered linear polarized light is highly depolarized after only one scattering event. As the number of scattering events increases, linearly polarized light's DoP decreases to a completely unpolarized state. Backscattered light from circular polarization is also depolarized after one scattering event, although not to the extent of linear polarization, but the DoP increases for circular polarization as the number of scattering events increases. After about ten scattering events, circular polarized backscattered light peaks to its largest DoP. After this, circular backscattered photon's DoP begins to decrease but remains highly polarized even after 30 scattering events. It is difficult to understand the significance of this initial depolarization and then increase in DoP for backscattered circular polarized photons from the forward-scattering environments since the relative number of backscattered photons is so small. After one scattering event just over 1 percent of the light is backscattered for these environments. As the number of backscattered photons increases after successive scattering events there are a larger number of photons for the cumulative Stokes state. In Figure 5.31 (b), cir-

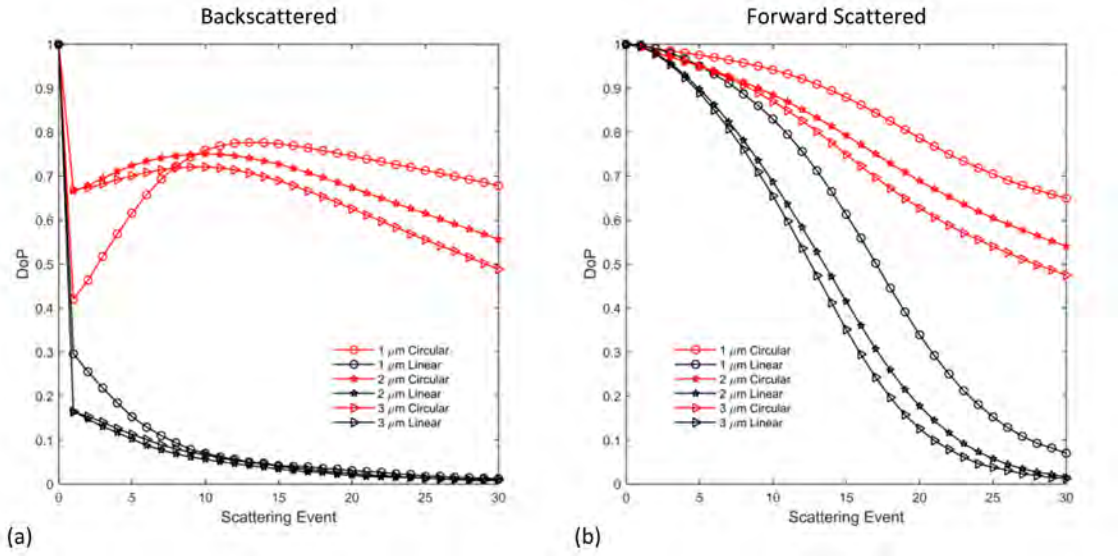

Figure 5.31: Cumulative DoP, for (a) backscattered and (b) forward scattered photons, from circularly (red) and linearly (black) polarized incident polarization states versus number of scattering events. The three particle sizes are plotted as follows: 1.0 microns is plotted with o's, 2.0 microns is plotted with stars, and 3.0 microns is plotted with triangles. Forward and backscattered light from incident circularly polarized light for the forward-scattering environments maintains its DoP and therefore persists through a larger number of scattering events.

cularly incident forward scattered photons remain highly polarized through a larger number of scattering events. The linearly polarized incident photons remain highly polarized for small numbers of scattering events but depolarize more quickly than circularly polarized photons. As the number of scattering events increases, circular polarization remains largely polarized while linear polarization depolarizes into a plurality of linearly polarized states. Overall, forward and backscattered light from incident circularly polarized light for the forward-scattering environments maintains its DoP and therefore persists through a larger number of scattering events.

5.4 **Summary**

This work quantitatively and qualitatively presents the evolution of linear and circularly polarized light as it scatters throughout both isotropic (Rayleigh regime) and forward-scattering environments. Circularly polarized light persists through a larger number of scattering events longer than linearly polarized light for all forward-scattering environments. In this forward-scattering environment circular polarization's increased persistence occurs for both forward and backscattered light. The simulated forward-scattering environments modeled polystyrene microspheres in water with particle diameters of 1.0, 2.0, and 3.0 microns. The scattering profiles of these environments are consistent with advection (marine) fog at infrared wavelengths. The evolution of the polarization states as they scatter throughout the various environments are illustrated on the Poincaré sphere after one, two, five, ten, fifteen and twenty scattering events. This work also modeled a more isotropically scattering environment with a 0.1 micron particle diameter. In this isotropic

scattering regime circularly and linearly polarized light depolarize rapidly. Linear polarization persists better for this isotropic environment. Incident linearly polarized light depolarizes into various other linearly polarized states while incident circularly polarized light depolarizes into a multitude of elliptical states initially and then evolves into more and more linear polarized states.

For all of the forward-scattering environments, circular polarization maintains a high degree of polarization, and remains in a range of states near the incident polarization state, throughout a large number of scattering events. Linear polarization depolarizes more rapidly into other linearly polarized states than into elliptical states, leading to a more highly depolarized cumulative state compared to that of circular polarization. This work shows clearly that circular polarization is superior to linear polarization in maintaining its DoP as a function of scattering event, and persisting through the larger forward-scattering particle environments. Circularly polarized light slowly, and smoothly degrades from its initial state, maintaining the same handedness, while linearly polarized light abruptly depolarizes into a plethora of other linear polarization states. This work quantifies the polarization persistence and memory of circularly polarized light in forward-scattering environments; and for the first time, details the evolution and modification of both circularly and linearly polarized states through scattering environments.

CHAPTER 6

Conclusions and Future Work

This dissertation presents simulations and experimental results quantifying the use of circularly polarized light in various laboratory and real-world scattering environments; specifically, it focuses on circularly polarized light's superior persistence in these environments. This chapter summarizes conclusions from these simulation and experimental results, identifies future work, and identifies potential real world benefits of utilizing circularly polarized light.

From Chapter 3, the use of polarization-tracking Monte Carlo simulations shows that there are clear, broad wavelength ranges where transmitted and reflected circular polarization maintains its illuminating polarization state superiorly compared to linear polarization, in highly scattering environments representative of radiation and advection fog. This work also examines small and large particle Sahara dust where it is shown that circular polarization also maintains its illuminating polarization state better than linear polarization. Compared to linear polarization, circular polarization results in a larger response and maintains its polarization state over broader wavelength ranges, for limited particle sizes.

Simulations of these four real-world environments identify wavelength ranges where circular polarization can be employed to increase detection range. Radiation fog has wavelength ranges available in the entire infrared spectrum. All three fog particle sizes simulated (1, 4, and 10 microns) show an advantage for circular

polarization in the short-wave infrared (SWIR); the 4 and 10 micron fog particles show an advantage in the mid-wave IR (MWIR); and the 10 micron fog particles exhibit superior persistence for circular polarization over linear polarization in the long-wave IR (LWIR). All three fog particle sizes in the advection fog model (10, 20, and 40 microns) persist longer for circular polarization than they do for linear polarization through the SWIR and LWIR wavebands.

The persistence of circular polarization is positive but not as pronounced for the two dust model particle size regimes (small and large Sahara dust). The 6 micron particle size results from the small particle Sahara dust show persistence benefits for the broad wavelength ranges of 2.5 – 9 microns and 10.5 – 12 microns. In the large Sahara dust simulation, circular polarization persists superiorly for the 10 micron particle size across a broad wavelength range of 3.5 – 8.75 microns.

This dissertation work is distinct from previously published works, offering new insight into realistic environments with broad wavelength ranges of interest where circular polarization can be utilized to increase detection range. This work presents simulation results supporting broad wavelength responses for particle sizes and refractive indices representative of natural scattering environments; the dissertation quantifies circular polarization's advantage over linear polarizations through broader wavelength ranges than linear polarization.

Experimental measurements are performed and analyzed in Chapter 4 for three scattering environments of polystyrene microspheres in water with particle diameters of 0.0824, 0.99 and 1.925 microns. For the forward-scattering environments (0.99 and 1.925 micron particle diameters), simulations show that circular polar-

ization maintains its DoP through increasing optical thickness much better than linear polarization. The opposite is true for simulations of isotropically (Rayleigh regime) scattering environment of 0.0824 micron particle diameter. Experimental results confirm these simulated predictions for all three particle sizes. I hypothesize the limited extent of the experiment's cuvette volume as compared to the simulation's infinite lateral extent can account for the difference between measured DoP and simulated DoP values. This hypothesis is further quantified in simulation for varying collection geometries. The collected DoP for both linear and circular polarization is very susceptible to collection geometry variation in the isotropically scattering (Rayleigh regime) environment. Similar susceptibilities are shown for linear polarization in the forward-scattering environments, but the effect is much smaller. Uniquely, circular polarization is nearly unaffected by variations in collection geometry for the forward-scattering environments. Circular polarization proves to be more tolerant of collection geometry variations compared to linear polarization. Overall, despite variations from the size of the cuvette and collection geometry, circular polarization persists longer than linear polarization for forward-scattering environments and point to follow-on work that can lead to a discriminating measurement for real-world configurations.

Lastly, in Chapter 5, this dissertation quantitatively illustrates the evolution of linearly and circularly polarized light as it scatters throughout both isotropic (Rayleigh regime) and forward-scattering environments as a function of scattering event. Circularly polarized light persists through a larger number of scattering events longer than linearly polarized light for all forward-scattering environments.

In each of these forward-scattering environments, circular polarization's increased persistence occurs in forward as well as back-scattered light configurations. The simulated forward-scattering environments consist of polystyrene microspheres in water with particle diameters of 1.0, 2.0, and 3.0 microns. The evolution of the polarization states as they scatter throughout the various environments are illustrated on the Poincaré sphere after one, two, five, ten, fifteen, and twenty scattering events. This work also models a more isotropically scattering environment using a 0.1 micron particle diameter. In the isotropic scattering regime, circularly and linearly polarized light depolarizes rapidly. Uniquely, linear polarization persists better for this isotropic environment. Incident linearly polarized light depolarizes into various linearly polarized states while incident circularly polarized light depolarizes into a multitude of elliptical states initially and then evolves into more and more linear polarized states.

For all of the forward-scattering environments, circular polarization maintains a high degree of polarization, and remains in a range of states near the incident polarization state throughout numerous scattering events. Linear polarization depolarizes more rapidly into other linearly polarized states than into elliptical states, leading to a highly depolarized cumulative state, compared to that of circular polarization. This work clearly shows that circular polarization is superior to linear polarization in maintaining its DoP as a function of scattering event for larger, forward-scattering particle environments. During propagation, circularly polarized light slowly and smoothly degrades from its initial state, maintaining the same handedness, while linearly polarized light abruptly depolarizes into a plethora of

other linear polarization states. This work quantifies the polarization persistence and memory of circularly polarized light in forward-scattering environments; and for the first time, details the evolution and modification of both circularly and linearly polarized states through scattering environments.

This dissertation's unique contributions call for continued interest in circular polarization's benefits in scattering environmental applications, specifically the potential to increase detection range. This work has shown that utilizing the light's polarization state can improve signal persistence, increase range, and thus improve target detection in scattering environments. This research quantifies a waveband's sensing advantage in specific adverse scattering environments. This work identifies and highlights the mechanisms behind circular polarization's advantage in critical scattering environments of interest, enabling future real-world sensor configurations.

Follow-on this field of study includes a number of key investigations. One such effort is expanding simulations of polarization persistence in fog, dust and other scattering environments with polydisperse distributions of scattering particles. Realistic scattering environments can have a large range of particle sizes that may encompass a range of scattering regimes. With the addition of broader particle size distributions, the persistence of the polarization states will be affected by a combination of particle size responses. Further confirming experimental research on the variations of polarization persistence as a function of field of view and collection area for the various scattering environments is a compelling area of future work. Specifically, experimental analysis with larger cuvette sizes will be an important next step in this research. Certain optical configurations may be able to utilize circular polar-

ization's increased persistence more readily than others. Investigating and testing various optical configurations will lend insight into the best configuration for remote sensing.

Ultimately, measuring and utilizing the increased persistence of active illuminating circular polarization in real-world scattering environments is the goal. Preliminary measurements in a fog chamber have been performed at Sandia National Laboratories. These initial results can be found in Appendix A. Future work may investigate circular polarized light's increased persistence in various types of fog generated in calibrated fog chambers. This work could lead to increased detection range for remote sensing and security systems that encounter dense and highly scattering fog environments. Similar work may be performed in a variety of other real-world scattering environments like dust and smoke. Sandia National Laboratories is continuing related research, investigating the use of circular polarization for Light Detection and Ranging (LIDAR) remote sensing systems with the goal of increasing LIDAR's capabilities in all-weather situations where scattering has traditionally constrained performance.

Sensing an object or target in a scattering environment is a challenge for many sensors. There are many examples of scattering environments in nature that deteriorate human and machine vision capabilities. The results of this research provide valuable insights and expand the fundamental understanding of circular polarization's use in scattering environments that can be utilized to detect targets at larger ranges. From the Mantis shrimp to modern LIDAR systems, circular polarization offers superior persistence and increased detection range in scattering environments.

APPENDIX A

Monte Carlo Code

```
/*************************************************************
*  Copyright Jessica C. Ramella-Roman, Steve L. Jacques
and Scott A. Prahl 2005
*
*  Meridian Planes MC
*  Main program for Monte Carlo simulation of photon
*  travelling into scattering media keeping track of
*  its status of polarization. Slab geometry.
*
*  by Jessica C. Ramella-Roman
*
* This program is free software; you can redistribute it and/or
* modify it under the terms of the GNU General Public License
* as published by the Free Software Foundation; either version 2
*  of the License, or (at your option) any later version.
*  This program is distributed in the hope that it will be useful,
*  but WITHOUT ANY WARRANTY; without even the implied warranty of
*  MERCHANTABILITY or FITNESS FOR A PARTICULAR PURPOSE.  See the
*  GNU General Public License for more details.
*  You should have received a copy of the GNU General Public License
*  along with this program; if not, write to the Free Software
*  Foundation, Inc., 59 Temple Place - Suite 330, Boston, MA
02111-1307, USA.
*
****/

/*************************************************************
*  Modifications to original code were made by
John D. van der Laan
*  Results of these modifications are found throughout
this dissertation
*  Standard files needed to run this code can be found in
Ramella-Roman's archive:
*  http://omlc.org/software/polarization/
```

```
*
****/

#include <stdio.h>
#include <math.h>
#include <stdlib.h>
#include "array.h"
#include "complex.h"
#include "mie.h"
#include "nrutil.h"
#include <time.h>

#define ALIVE       1
#define DEAD        0
#define NN       201
#define THRESHOLD   0.01                /* used in roulette */
#define CHANCE      0.1                 /* used in roulette */
#define RandomNum (double) RandomGen(1, 0, NULL)
#define SIGN(x) ((x)>=0 ? 1:-1)
#define InitRandomGen (double) RandomGen(0, 1, NULL)

/* Declare Subroutines */
void  rotSphi(double* S, double phi, double* S2);
double RandomGen(char Type, long Seed, long *Status);
void  multS(double* S, double theta, double* S2);
void  rotateXXYY(double* XX, double* YY,double* ZZ,
double phi, double theta, double* XX2, double* YY2,double* ZZ2);
void  updateU(double* U, double phi, double theta, double* U2);
double  sincos(double *x);

/*************** MAIN *******************************/
int main() {
double pi = 3.1415926535897932384;

/* Mie Theory Inputs */
double radius,lambda, A;
long nangles,i;
struct complex m;
struct complex*s1=NULL;
struct complex*s2=NULL;
double *mu=NULL;
double x,qext,qsca,qback,g, rho, vol;
```

```
double nre_p, nim_p, nre_med, nim_med;
double jjj;

/* E field and Stokes Vector values */
double phi, theta,I,I0;
int  ithedeg;
double IT, QT, UT, VT;
double IR_1, QR_1, UR_1, VR_1;

/* Propagation parameters */
double y,z,x_p,y_p,z_p;/* photon position */
double s;          /* step sizes */
long i_photon;   /* current photon */
long Nphotons;   /* number of photons in simulation */
short   photon_status;  /* ALIVE=1 or DEAD=0 */

/* other variables */
double mua;        /* absorption coefficient [cm^-1] */
double mus;        /* scattering coefficient [cm^-1] */
double musp;       /* reduced scattering coefficient [cm^-1] */
double  albedo;     /* albedo */
double  W,absorb;  /* photon weight */
double  slabsize;  /*Max Extent of the Slab in Z direction*/
double  optdepth;  /*Optical Thickness*/

/* dummy variables */
double  rnd; /* assigned random value 0-1 */
double  cos22,sin22,costheta,sini,cosi;

/*Radial and Angular Values*/
double r_direction; /*cylindrical coordinate r direction */
double r_location; /*cylindrical coordinate r location */
double theta_out; /*exit angle of photon*/

double *U, *U2;
double *S;      /* */
double *S0;      /* */
double *S2;      /* */
double *s11=NULL;
double *s12=NULL;
double *s33=NULL;
double *s43=NULL;
```

```
double *IQUV;      /* [I, Q, U, V] Stokes Vector */
double  start_time,finish_time,temp;

/*Output Files*/
FILE *phoOutRefLin;
FILE *phoOutRefCirc;
FILE *phoOutTranLin;
FILE *phoOutTranCirc;

start_time = clock();

/* CHOOSE MIE SCATTERING parameters */
/* Values are inputted via bash script
* by searching for terms and replacing
* with desired values */
radius   = RADIUS; /* microns */
lambda  = LAMBDA; /* microns */
rho  = RHO;/*Dilution 1*/
Nphotons = NPHOTONS;
mua  = MUA; /*a  */
nre_p    = NRE_P;
nim_p     = NIM_P;
nre_med = NRE_MED;
nim_med  = NIM_MED;
nangles  = 1000;
optdepth = OPTDEPTH;
slabsize = SLABSIZE;

/**** allocate matrices and arrays *******/
U      = new_darray(3);//previous directional cosine
U2     = new_darray(3);//new direction after rejection method
S      = new_darray(4);//Stokes vector
S0     = new_darray(4);//Incident Stokes vector
S2     = new_darray(4);/* dummy S*/

IQUV   = new_darray(4);

/**** end  allocate matrices and arrays *******/

/* Setup MIE SCATTERING parameters */
mu  = new_darray(nangles);
s1  = new_carray(nangles);
```

```
s2  = new_carray(nangles);
s11 = new_darray(nangles);
s12 = new_darray(nangles);
s33 = new_darray(nangles);
s43 = new_darray(nangles);


/* Refractive index */
m.re = nre_p/nre_med;
if(nim_med == 0.00){m.im = nim_p;}
else{m.im = nim_p/nim_med;}

x    = 2*pi*radius/(lambda/nre_med); /*Size Parameter*/
vol  = 4.0/3*pi*radius*radius*radius; /*Volume of sphere*/
A    = pi*radius*radius; /*Geometrical Cross Section Area*/

for(i=0;i<=nangles;i++){
mu[i] = cos(pi*i/nangles); //Cos[Theta] Values
s11=new_darray(nangles);
s12=new_darray(nangles);
s33=new_darray(nangles);
s43=new_darray(nangles);
s1=new_carray(nangles);
s2=new_carray(nangles);
}

Mie(x,m,mu,nangles,s1,s2,&qext,&qsca,&qback,&g); /* <-- Call Mie program -- */
optdepth = rho*qsca*A*1e4*slabsize; /* Optical Thickness */
mus  = qsca*A*rho*1e4; /* Mus is in cm^-1 */
musp  = mus*(1-g);/* [cm^-1] */
albedo  = mus/(mus + mua);
free_darray(mu);

printf("Polarized Monte Carlo\n dia=%5.5f;\n mus=%5.8f;\n g=%5.8f;\n
 rho=%5.8f;\n lambda=%5.5f;\n n_p=%5.3f;\n k_p=%5.3f;\n n_m=%5.3f;\n
  k_m=%5.3f;\n slabsize=%5.3f;\n optdepth=%5.5f;\n Qext=%5.5f;\n
  Qsca=%5.5f;\n Qback=%5.5f;\n x=%5.5f;\n",radius*2,mus,g,rho,
  lambda,nre_p,nim_p,nre_med,nim_med,slabsize,mus*slabsize,qext,qsca,qback,x);


/*Scattering parameters s11 s12 s33 s43*/
for(i=0;i<=nangles;++i){
```

```
s11[i] = 0.5*cabbs(s2[i])*cabbs(s2[i]) + 0.5*cabbs(s1[i])*cabbs(s1[i]);
s12[i] = 0.5*cabbs(s2[i])*cabbs(s2[i]) - 0.5*cabbs(s1[i])*cabbs(s1[i]);
s33[i] = (cmul(conj(s1[i]),s2[i])).re;
s43[i] = (cmul(conj(s1[i]),s2[i])).im;
}

/******** Run MONTE CARLO *******/

InitRandomGen;

/* LAUNCHNOW*/
IT=0;/*W*/
QT=0;
UT=0;
VT=0;

IR_1=0;/*W*/
QR_1=0;
UR_1=0;
VR_1=0;

temp=0;

/*Determine the input Stokes Vector*/
for (jjj = 1; jjj <= 2; jjj++) {


//Vertical
if (jjj == 1){

S0[0] = 1;
S0[1] = -1;
S0[2] = 0;
S0[3] = 0;
printf("launch V\n");
}


//Right Circular
if (jjj == 2){

S0[0] = 1;
```

```
S0[1] = 0;
S0[2] = 0;
S0[3] = 1;
printf("launch R\n");}

Nphotons_c = 0;

/** LAUNCH photon **/
for (i_photon = 1; i_photon <= Nphotons; i_photon++) {

/* pencil beam */
x = 0.0;
y = 0.0;
z = 0.0;

/* photon initial direction cosines */
U[0] = 0.0;
U[1] = 0.0;
U[2] = 1.0;

for (i=0; i<4; i++) S[i] = S0[i]; /* set incident Stokes vector to S0 */
for (i=0; i<4; i++) S2[i] = 0.0; /* set meridian Stokes vector to 0 */

photon_status = ALIVE;
W = 1; /* photon weight */


/********* ALIVE cycle *****************/
while (photon_status == ALIVE) {

/**** HOP - Move photon ****/
rnd = 0;
while (rnd == 0) rnd = RandomNum;  /* choose a step size */

s = -log(rnd)/(mus+mua);
x += U[0]*s;
y += U[1]*s;
z += U[2]*s;

/**** ABSORB ****/
absorb = W*(1-albedo);
W-= absorb;
```

```
/* Exits Front Face - Reflection: Z is negative or 0 */
if ( z<=0) {

/*return to detector reference frame*/
phi=atan2(U[1],U[0]);
rotSphi(S, phi, S2);

//Save cumulative Stokes Vector
IR_1+=S2[0];
QR_1+=S2[1];
UR_1+=S2[2];
VR_1+=S2[3];

/*Trace photon back to previous scattering position */
x_p = x - U[0]*s;
y_p = y - U[1]*s;
z_p = z - U[2]*s;

r_location = sqrt(x_p*x_p + y_p*y_p);
r_direction = sqrt(U[0]*U[0] + U[1]*U[1]);
theta_out = atan(-1*r_direction/U[2]);
/*Angle with respect to surface. i.e. normal
* to surface = 0 deg. Note that U[2] is negative
* when travelling in backscattering direction */

/*Linear Photon Output Information*/
if(jjj==1){
phoOutRefLin = fopen("LinearReflectionOutput.dat","a+");
fprintf(phoOutRefLin,"%ld %f %f %f %f %f %f %f %f
%f %f %f %f %f\n",i_photon,x,y,z,x_p,y_p,z_p,
r_location,r_direction,theta_out,S2[0],S2[1],S2[2],S2[3]);
fclose(phoOutRefLin);
}
/*Circular Photon Output Information*/
if(jjj==2){
phoOutRefCirc = fopen("CircularReflectionOutput.dat","a+");
fprintf(phoOutRefCirc,"%ld %f %f %f %f %f %f %f %f
%f %f %f %f %f\n",i_photon,x,y,z,x_p,y_p,z_p,
r_location,r_direction,theta_out,S2[0],S2[1],S2[2],S2[3]);
fclose(phoOutRefCirc);
}
```

```
photon_status = DEAD;
}
/* Exits Back Face - Transmission
* Z is > than slabsize */
else if ( z>=slabsize) {

/*return to detector reference frame*/
phi=-atan2(U[1],U[0]);
rotSphi(S, phi, S2);

//Save cumulative Stokes Vector
IT+=S2[0]*W;
QT+=S2[1]*W;
UT+=S2[2]*W;
VT+=S2[3]*W;

/*Trace photon back to previous scattering position */
x_p = x - U[0]*s;
y_p = y - U[1]*s;
z_p = z - U[2]*s;

r_location = sqrt(x_p*x_p + y_p*y_p);
r_direction = sqrt(U[0]*U[0] + U[1]*U[1]);
theta_out = atan(1*r_direction/U[2]);
/*Angle with respect to surface. i.e. normal
* to surface = 0 deg. */


/*Linear Photon Output Information*/
if(jjj==1){
phoOutTranLin = fopen("LinearTransmissionOutput.dat","a+");
fprintf(phoOutTranLin,"%ld %f %f %f %f %f %f %f %f
%f %f %f %f %f\n",i_photon,x,y,z,x_p,y_p,z_p,
r_location,r_direction,theta_out,S2[0]*W,S2[1]*W,S2[2]*W,S2[3]*W);
fclose(phoOutTranLin);
}
/*Circular Photon Output Information*/
if(jjj==2){
phoOutTranCirc = fopen("CircularTransmissionOutput.dat","a+");
fprintf(phoOutTranCirc,"%ld %f %f %f %f %f %f %f %f
%f %f %f %f %f\n",i_photon,x,y,z,x_p,y_p,z_p,
```

```
r_location,r_direction,theta_out,S2[0]*W,S2[1]*W,S2[2]*W,S2[3]*W);
fclose(phoOutTranCirc);
}

photon_status = DEAD;
}/*z>slab size*/

/*** SPIN ***/

/* REJECTION METHOD to choose azimuthal angle phi and deflection angle theta */

do{ theta = acos(2*RandomNum-1);
phi = RandomNum*2.0*pi;  /*choose phi randomly */
I0=s11[0]*S[0]+s12[0]*(S[1]*cos(2*phi)+S[2]*sin(2*phi));
ithedeg = floor(theta*nangles/pi);
/*MIE PHASE FUNCTION. Probability AT GIVEN PHI AND THETA!! */
I=s11[ithedeg ]*S[0]+s12[ithedeg]*(S[1]*cos(2*phi)+S[2]*sin(2*phi));
}while(RandomNum*I0>=I);

/****-----------------------------------------
Scattering : rotate to meridian plane then scatter
-----------------------------------------------*****/

updateU(U, phi, theta, U2);  /* update photon trajectory vector */
costheta=cos(theta);
rotSphi(S, phi, S2);

//Update Incident Stokes after Scattering Event
S[0]= s11[ithedeg]*S2[0]+s12[ithedeg]*S2[1];
S[1]= s12[ithedeg]*S2[0]+s11[ithedeg]*S2[1];
S[2]= s33[ithedeg]*S2[2]+s43[ithedeg]*S2[3];
S[3]= -s43[ithedeg]*S2[2]+s33[ithedeg]*S2[3];

temp=(sqrt(1-costheta*costheta)*sqrt(1-U2[2]*U2[2]));

if ( temp==0){
cosi=0;}
else{
if ((phi>pi) & (phi<2*pi))
cosi=(U2[2]*costheta-U[2])/temp;
else
cosi=-(U2[2]*costheta-U[2])/temp;
```

```
if (cosi<-1) cosi=-1;
if (cosi>1) cosi=1;
}

sini = sqrt(1-cosi*cosi);
cos22=2*cosi*cosi-1;
sin22=2*sini*cosi;

//Update Meridian Stokes Vector after Scatter
S2[0]=S[0];
S2[1]=(S[1]*cos22-S[2]*sin22);
S2[2]=(S[1]*sin22+S[2]*cos22);
S2[3]=S[3];

//Update Incident Normalized Stokes Vector
S[1]= S2[1]/S2[0];
S[2]= S2[2]/S2[0];
S[3]= S2[3]/S2[0];
S[0]= 1.0;

/* update U - direction Cosines */
for (i=0; i<3; i++) U[i] = U2[i];

/*ROULETTE*/
rnd=0; while(rnd==0) rnd=RandomNum;

if (W<THRESHOLD){
if (rnd<=CHANCE)
W/=CHANCE;
else photon_status=DEAD;
}

} /* end of single photon launching */

}/* slab size*/

//Print Cumulative Stokes Values
printf("R= %5.8f\t %5.8f\t %5.8f\t %5.8f\n ",
IR_1/(Nphotons),QR_1/(Nphotons),UR_1/(Nphotons),VR_1/(Nphotons));
printf("T= %5.8f\t %5.8f\t %5.8f\t %5.8f\n ",
IT/(Nphotons),QT/(Nphotons),UT/(Nphotons),VT/(Nphotons));
```

```
IT=0;
QT=0;
UT=0;
VT=0;

IR_1=0;
QR_1=0;
UR_1=0;
VR_1=0;

}/* end of 4 photon launchings */

finish_time = clock();
printf("Elapsed Time = %15.2f seconds\n",
 (double)(finish_time-start_time)/CLOCKS_PER_SEC);

fflush(NULL);
return 0;
} /* End main routine*/

/*************** end MAIN *****************************/

/*********************************************************/
/* SUBROUTINES */
/*********************************************************
* RandomGen
*      A random number generator that generates uniformly
*      distributed random numbers between 0 and 1 inclusive.
*      The algorithm is based on:
*      W.H. Press, S.A. Teukolsky, W.T. Vetterling, and B.P.
*      Flannery, "Numerical Recipes in C," Cambridge University
*      Press, 2nd edition, (1992).
*      and
*      D.E. Knuth, "Seminumerical Algorithms," 2nd edition, vol. 2
*      of "The Art of Computer Programming", Addison-Wesley, (1981).
*
*      When Type is 0, sets Seed as the seed. Make sure 0<Seed<32000.
*      When Type is 1, returns a random number.
*      When Type is 2, gets the status of the generator.
*      When Type is 3, restores the status of the generator.
*
*      The status of the generator is represented by Status[0..56].
```

```
*
*      Make sure you initialize the seed before you get random
*      numbers.
****/
#define MBIG 1000000000
#define MSEED 161803398
#define MZ 0
#define FAC 1.0E-9

double
RandomGen(char Type, long Seed, long *Status){
static long i1, i2, ma[56];   /* ma[0] is not used. */
long        mj, mk;
short       i, ii;

if (Type == 0) {              /* set seed. */
mj = MSEED - (Seed < 0 ? -Seed : Seed);
mj %= MBIG;
ma[55] = mj;
mk = 1;
for (i = 1; i <= 54; i++) {
ii = (21 * i) % 55;
ma[ii] = mk;
mk = mj - mk;
if (mk < MZ)
mk += MBIG;
mj = ma[ii];
}
for (ii = 1; ii <= 4; ii++)
for (i = 1; i <= 55; i++) {
ma[i] -= ma[1 + (i + 30) % 55];
if (ma[i] < MZ)
ma[i] += MBIG;
}
i1 = 0;
i2 = 31;
} else if (Type == 1) {       /* get a number. */
if (++i1 == 56)
i1 = 1;
if (++i2 == 56)
i2 = 1;
mj = ma[i1] - ma[i2];
```

```
if (mj < MZ)
mj += MBIG;
ma[i1] = mj;
return (mj * FAC);
} else if (Type == 2) {       /* get status. */
for (i = 0; i < 55; i++)
Status[i] = ma[i + 1];
Status[55] = i1;
Status[56] = i2;
} else if (Type == 3) {       /* restore status. */
for (i = 0; i < 55; i++)
ma[i + 1] = Status[i];
i1 = Status[55];
i2 = Status[56];
} else
puts("Wrong parameter to RandomGen().");
return (0);
}
#undef MBIG
#undef MSEED
#undef MZ
#undef FAC

/*****************************************************
* rotSphi(S,phi,S)
* Rotate S by phi [radians] and return as S
*      multiply S for the rotational matrix of
Chandrasekar or Boheren and Hoffman
* Uses invtan()
****/
void  rotSphi(double* S, double phi, double* S2) {
double cos2phi, sin2phi;

cos2phi = cos(2*phi);
sin2phi = sin(2*phi);

S2[0] = S[0];
S2[1] = S[1]*cos2phi+S[2]*sin2phi;
S2[2] = -S[1]*sin2phi+S[2]*cos2phi;
S2[3] = S[3];

}
```

```
/*****************************************************
* updateU(U,U2)
****/
void  updateU(double* U, double phi, double theta, double* U2) {
double ux, uy, uz, uxx, uyy, uzz, temp,
 sintheta, costheta, sinphi, cosphi;
double  pi = 3.14159265358979;

ux = U[0];
uy = U[1];
uz = U[2];

costheta = cos(theta);
sintheta = sqrt(1.0 - costheta*costheta);
cosphi   = cos(phi);
if (phi < pi)
sinphi = sqrt(1.0 - cosphi*cosphi);
else
sinphi = -sqrt(1.0 - cosphi*cosphi);

/* New directional cosines. */
if (1 - fabs(uz) <= 1.0E-12) { /* close to perpendicular. */
uxx = sintheta * cosphi;
uyy = sintheta * sinphi;
uzz = costheta * SIGN(uz); /*  SIGN(x) is faster than division. */
}
else { /* usually use this option */
temp = sqrt(1.0 - uz * uz);
uxx = sintheta *
(ux * uz * cosphi - uy * sinphi) / temp + ux * costheta;
uyy = sintheta *
(uy * uz * cosphi + ux * sinphi) / temp + uy * costheta;
uzz = -sintheta * cosphi * temp + uz * costheta;
}
/* Update directional cosines */
U2[0] = uxx;
U2[1] = uyy;
U2[2] = uzz;
}
```

APPENDIX B

Sandia National Laboratories Fog Chamber Experiments

B.1 Fog Chamber Experimental Setup

A set of polarization persistence experiments were performed in controllable fog chambers at Sandia National Laboratories in January of 2014. This appendix presents those initial fog chamber measurement results. The experimental fog chamber setup was similar to that described in Chapter 4 of the dissertation, where the scattering environment was microspheres suspended in water. However, the fog chamber setup differed from the dissertation experiment in that the fog-chamber setup utilized an f/22 lens with focal length of 150 mm for collection, whereas the dissertation experiment utilized an f/1.19 Mitutoyo objective. The experimental setup used in the fog chamber is shown in Figure B.1. In order to protect the optical setup from the fog environment, the optics were enclosed and sealed in plastic weather proofing, as shown in Figure B.2. In addition to the weather sealing, forced air curtains were used to keep the windows to the optics clear of condensation. The path length between the optical windows was set to 30 cm.

Fog was generated in the chamber by forcing water through calibrated nozzles. Fog's particle size distribution is dependent on the water mixture used and how much of a chosen seed particle is present. Four sets of fog were generated and data was collected on the polarization persistence of linear and circular polarization

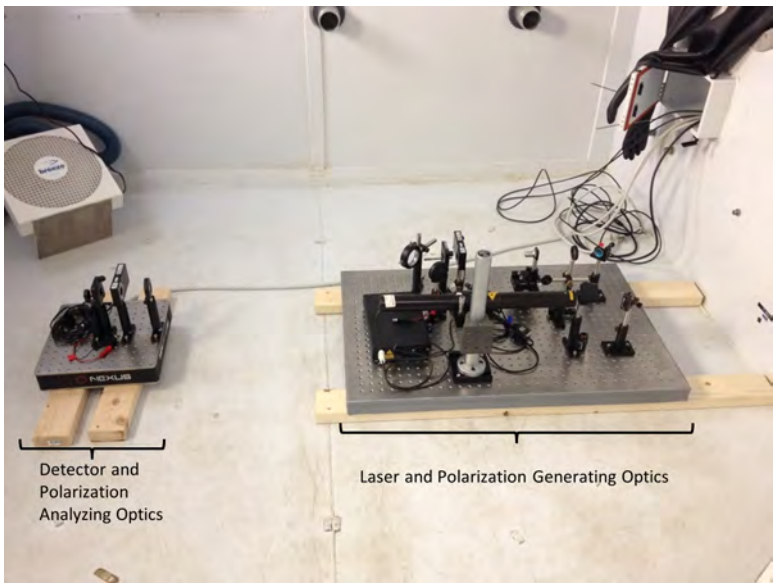

Figure B.1: Fog chamber experimental setup.

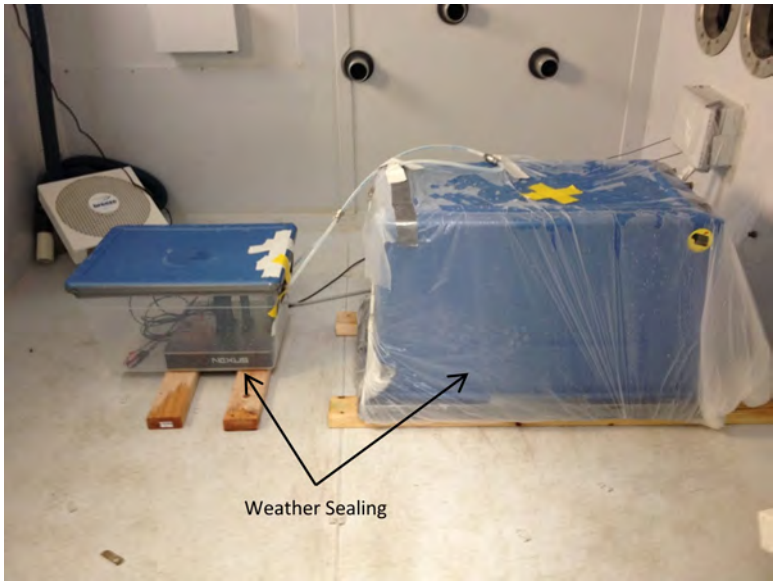

Figure B.2: Fog chamber experimental setup with addition of weather sealing.

states. The fog's characteristics were not calibrated and thus no corresponding particle distribution information was available. At the time of the experiment, there was no capability to measure the temporal variation of the fog's density or particle distribution. Due to the lack of data on the controlled environment, there was no attempt to use Monte Carlo simulations for comparison to the fog chamber results. This work solely presents the resulting DoP measurements for the different fogs generated. Similar to the dissertation work, measured DoP provides a measure of polarization persistence, where greater DoP for circular polarization compared to linear polarization shows greater persistence in the scattering environment. As stated in Chapter 6, this area is readily available as future work.

B.2 **Results**

Four types of marine fog were tested. The marine fog uses salt (NaCl) as seed particles. The fog is generated by first spraying pure water through the nozzles for a set time duration. After this interval, a second spray is performed with salt water for a set time duration. Varying the salt concentration and the spray durations for both the pure water and salt water spray changes the properties of the fog generated. Experimental results show measured DoP increases, for both linear and circular polarizations, with time (plotted as increasing sample number) for all four types of fog.

There are three components of the measurements taken that led to few valuable data points. The measured DoP for all the following plots quickly rises to 1 (purely polarized). This is attributed to the very small collection angle of the collection lens,

the short path length, and the quick temporal degradation of the fog. These factors contributed to insufficient scattering over too short of a time frame for the light to depolarize. The difference between the measured DoP for circular and linear polarization was not significant. Though in the first few measurement samples for each fog environment, there were glimpses of circular polarization's increased persistence compared to linear polarization, the number of data points is insufficient to draw defensible conclusions.

B.2.1 **Marine Fog 1**

The first fog investigated was generated by a five minute spray of pure water followed by a two minute spray of salt water with a concentration of 10 grams per liter. Figure B.3 shows the results for the first fog generated. The fog dissipated very quickly so only the first measured value resulted in valuable data. The single data point shows circular polarization persists superiorly, but both polarization states are highly polarized. The small collection angle only collects photons that scatter few times at very small angles, which leads to high DoP, even for the first measurements.

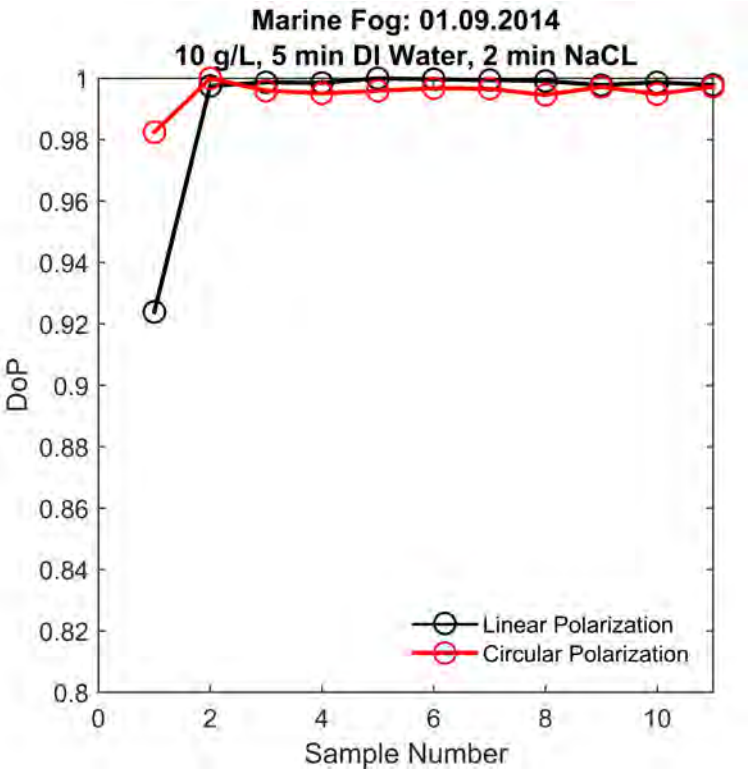

Figure B.3: Experimental results for marine fog: 5 minute pure water spray followed by a 2 minute salt water (10 g/L) spray.

B.2.2 **Marine Fog 2**

The second fog investigated was generated by a five minute spray of pure water followed by a five minute spray of salt water with a concentration of 10 grams per liter. The results are shown in Figure B.4. Circular polarization persists superiorly for the first three samples. The fog was thicker than the first fog and dissipated at a slower rate.

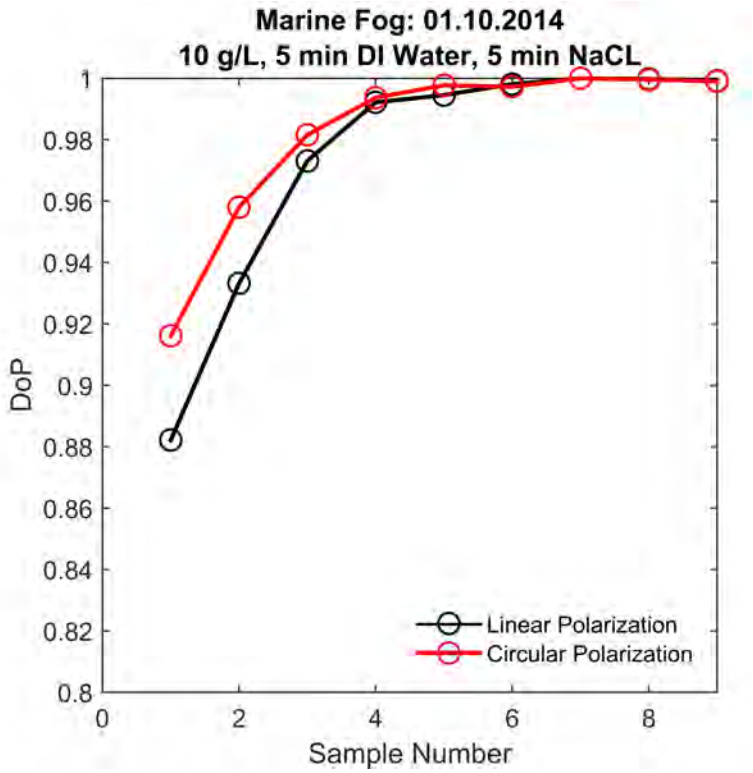

Figure B.4: Experimental results for marine fog: 5 minute pure water spray followed by a 5 minute salt water (10 g/L) spray.

B.2.3 **Marine Fog 3**

The third fog investigated was generated by a five minute spray of pure water followed by a two min spray of salt water with a concentration of 30 grams per liter. The results are shown in Figure B.5. For this fog, circular polarization is marginally better than linear polarization for the first three samples. This fog was thicker and dissipated slower than the second fog.

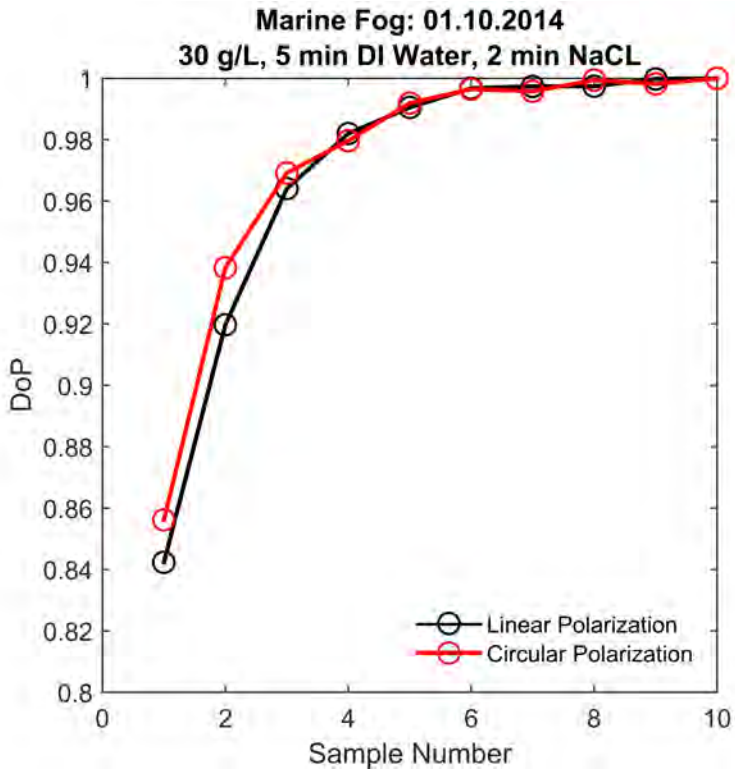

Figure B.5: Experimental results for marine fog: 5 minute pure water spray followed by a 2 minute salt water (30 g/L) spray.

B.2.4 **Marine Fog 4**

The fourth fog investigated was generated by a five minute spray of pure water followed by a five minute spray of salt water with a concentration of 30 grams per liter. The results are shown in Figure B.6. Circularly polarized light persists better than linear for the first two samples of this fog. This fog was the thickest of the samples and dissipated faster than the third fog but slower than the second.

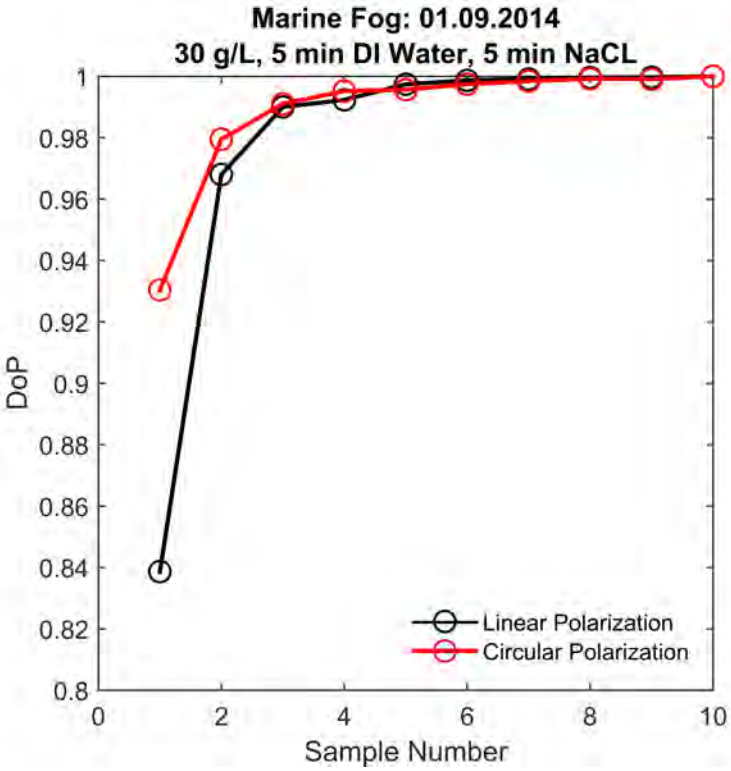

Figure B.6: Experimental results for marine fog: 5 minute pure water spray followed by a 5 minute salt water (30 g/L) spray.

B.3 **Summary**

Measurement results were presented here for experiments conducted in Sandia National Laboratories' fog chamber. Measurements were made in four different types of marine fog with varying amounts and concentrations of salt water. Overall, for the first few measurements in each type of fog, circular polarization persisted better than linear polarization. These results are limited to very small collection angles from an f/22 collection lens and a small path length of 30 cm. The fog density and particle distributions varied quickly in time and were not calibrated or known. Due to these limitations, the measured DoP is large for all samples and the difference

between linear and circular polarization are quite small. These measurements are a starting point for future work investigating polarization persistence in real world scattering environments. With the addition of larger collection angles, longer path lengths, and calibrated fog generation, future experiments have great potential for valuable results.

REFERENCES

[1] E. Bartholin, *Experimenta crystalli islandici disdiaclastici quibus mira & insolita refractio detegitur*. 1669.

[2] E. T. Whittaker, *A History of the Theories of Aether and Electricity from the Age of Descartes to the Close of the Nineteenth Century*. Longmans, Green and Company, 1910.

[3] "http://upload.wikimedia.org/wikipedia/commons/3/39/ odontodactylus-scyllarus2.jpg."

[4] N. Marshall, "A unique colour and polarization vision system in mantis shrimps," *Nature*, vol. 333, no. 9, pp. 557–560, 1988.

[5] T. Cronin and N. Marshall, "A retina with at least ten spectral types of photoreceptors in a mantis shrimp," *Nature*, vol. 339, pp. 137–140, 1989.

[6] T. Cronin, N. Marshall, and M. Land, "The unique visual system of the mantis shrimp," *Am. Sci.*, vol. 82, no. 4, pp. 356–365, 1994.

[7] J. Marshall and J. Oberwinkler, "The colourful world of the mantis shrimp.," *Nature*, vol. 401, pp. 873–4, Oct. 1999.

[8] T. W. Cronin, R. L. Caldwell, and J. Marshall, "Sensory adaptation. Tunable colour vision in a mantis shrimp.," *Nature*, vol. 411, no. 6837, pp. 547–548, 2001.

[9] C. W. Hawryshyn, "Polarization Vision in Fish," *Am. Sci.*, vol. 80, pp. 164–175, Mar. 1992.

[10] R. Wehner, "Polarization vision–a uniform sensory capacity?," *J. Exp. Biol.*, vol. 204, pp. 2589–96, July 2001.

[11] N. Shashar, R. Hagan, J. G. Boal, and R. T. Hanlon, "Cuttlefish use polarization sensitivity in predation on silvery fish," *Vision Res.*, vol. 40, pp. 71–75, Jan. 2000.

[12] T.-H. Chiou, S. Kleinlogel, T. Cronin, R. Caldwell, B. Loeffler, A. Siddiqi, A. Goldizen, and J. Marshall, "Circular polarization vision in a stomatopod crustacean.," *Curr. Biol.*, vol. 18, pp. 429–34, Mar. 2008.

[13] S. Kleinlogel and A. G. White, "The secret world of shrimps: polarisation vision at its best.," *PLoS One*, vol. 3, p. e2190, Jan. 2008.

[14] "http://mission-blue.org/wp-content/uploads/2013/07/peacock-mantis-shrimp_18428_990x742.jpg."

[15] "https://student.societyforscience.org/sites/student.societyforscience.org/files/main/articles/oscyllarus-eye-rlc.jpg."

[16] G. D. Gilbert and J. C. Pernicka, "Improvement Of Underwater Visibility By Reduction Of Backscatter With A Circular Polarization Technique," *Proc. SPIE*, vol. 0007, pp. 15–25, 1966.

[17] G. D. Gilbert and J. C. Pernicka, "Improvement of underwater visibility by reduction of backscatter with a circular polarization technique.," *Appl. Opt.*, vol. 6, pp. 741–6, Apr. 1967.

[18] G. D. Gilbert, "The effects of particle size on contrast improvement by polarization discrimination for underwater targets.," *Appl. Opt.*, vol. 9, pp. 421–8, Feb. 1970.

[19] X. Ma, J. Q. Lu, R. S. Brock, K. M. Jacobs, P. Yang, and X.-H. Hu, "Determination of complex refractive index of polystyrene microspheres from 370 to 1610 nm.," *Phys. Med. Biol.*, vol. 48, pp. 4165–72, Dec. 2003.

[20] D. Bicout, C. Brosseau, A. Martinez, and J. Schmitt, "Depolarization of multiply scattered waves by spherical diffusers: Influence of the size parameter," *Phys. Rev. E*, vol. 49, no. 2, pp. 1767–70, 1994.

[21] M. P. Silverman and W. Strange, "Object delineation within turbid media by backscattering of phase-modulated light," *Opt. Commun.*, vol. 144, pp. 7–11, Dec. 1997.

[22] B. D. Cameron, M. J. Rakovic, M. Mehrübeoglu, G. W. Kattawar, S. Rastegar, L. V. Wang, and G. L. Coté, "Measurement and calculation of the two-dimensional backscattering Mueller matrix of a turbid medium," *Opt. Lett.*, vol. 23, p. 485, Apr. 1998.

[23] M. J. Raković, G. W. Kattawar, M. B. Mehrubeolu, B. D. Cameron, L. V. Wang, S. Rastegar, and G. L. Coté, "Light backscattering polarization patterns from turbid media: theory and experiment.," *Appl. Opt.*, vol. 38, pp. 3399–408, May 1999.

[24] G. D. Lewis, D. L. Jordan, and P. J. Roberts, "Backscattering target detection in a turbid medium by polarization discrimination.," *Appl. Opt.*, vol. 38, pp. 3937–44, June 1999.

[25] V. Sankaran, K. Schönenberger, J. T. Walsh, and D. J. Maitland, "Polarization discrimination of coherently propagating light in turbid media.," *Appl. Opt.*, vol. 38, pp. 4252–61, July 1999.

[26] V. Sankaran, J. T. Walsh, Jr., and D. J. Maitland, "Polarized light propagation through tissue phantoms containing densely packed scatterers," *Opt. Lett.*, vol. 25, p. 239, Feb. 2000.

[27] S. Bartel and A. H. Hielscher, "Monte Carlo simulations of the diffuse backscattering mueller matrix for highly scattering media.," *Appl. Opt.*, vol. 39, pp. 1580–8, Apr. 2000.

[28] J. G. Walker, P. C. Chang, and K. I. Hopcraft, "Visibility depth improvement in active polarization imaging in scattering media.," *Appl. Opt.*, vol. 39, pp. 4933–41, Sept. 2000.

[29] K. Turpin, J. Walker, P. Chang, K. Hopcraft, B. Ablitt, and E. Jakeman, "The influence of particle size in active polarization imaging in scattering media," *Opt. Commun.*, vol. 168, pp. 325–335, Sept. 1999.

[30] A. Ishimaru, S. Jaruwatanadilok, and Y. Kuga, "Polarized pulse waves in random discrete scatterers.," *Appl. Opt.*, vol. 40, pp. 5495–502, Oct. 2001.

[31] U. Ketprom, Y. Kuga, S. Jaruwatanadilok, and A. Ishimaru, "Experimental and numerical analysis of polarized light through random distributed spherical particles," *Proc. SPIE*, vol. 4819, pp. 35–45, 2002.

[32] A. D. Kim and M. Moscoso, "Backscattering of circularly polarized pulses.," *Opt. Lett.*, vol. 27, pp. 1589–91, Sept. 2002.

[33] S. Kartazayeva, X. Ni, and R. Alfano, "Backscattering target detection in a turbid medium by use of circularly and linearly polarized light.," *Opt. Lett.*, vol. 30, pp. 1168–70, May 2005.

[34] R. E. Nothdurft and G. Yao, "Effects of turbid media optical properties on object visibility in subsurface polarization imaging.," *Appl. Opt.*, vol. 45, pp. 5532–41, Aug. 2006.

[35] W. Cai, X. Ni, S. Gayen, and R. Alfano, "Analytical cumulant solution of the vector radiative transfer equation investigates backscattering of circularly polarized light from turbid media," *Phys. Rev. E*, vol. 74, p. 056605, Nov. 2006.

[36] P. Shukla, R. Sumathi, S. Gupta, and A. Pradhan, "Influence of size parameter and refractive index of the scatterer on polarization-gated optical imaging through turbid media.," *J. Opt. Soc. Am. A*, vol. 24, pp. 1704–13, June 2007.

[37] P. Shukla and A. Pradhan, "Polarization-gated imaging in tissue phantoms: effect of size distribution.," *Appl. Opt.*, vol. 48, pp. 6099–104, Nov. 2009.

[38] M. Dubreuil, P. Delrot, I. Leonard, A. Alfalou, C. Brosseau, and A. Dogariu, "Exploring underwater target detection by imaging polarimetry and correlation techniques.," *Appl. Opt.*, vol. 52, pp. 997–1005, Feb. 2013.

[39] C. Henrist, J.-P. Mathieu, C. Vogels, A. Rulmont, and R. Cloots, "Morphological study of magnesium hydroxide nanoparticles precipitated in dilute aqueous solution," *J. Cryst. Growth*, vol. 249, no. 12, pp. 321–330, 2003.

[40] B. A. Swartz and J. D. Cummings, "Laser range-gated underwater imaging including polarization discrimination," *Proc. SPIE*, vol. 1537, pp. 42–56, Dec. 1991.

[41] M. P. Rowe, E. N. Pugh, J. S. Tyo, and N. Engheta, "Polarization-difference imaging: a biologically inspired technique for observation through scattering media.," *Opt. Lett.*, vol. 20, pp. 608–10, Mar. 1995.

[42] J. S. Tyo, M. P. Rowe, E. N. Pugh, and N. Engheta, "Target detection in optically scattering media by polarization-difference imaging.," *Appl. Opt.*, vol. 35, pp. 1855–70, Apr. 1996.

[43] D. B. Chenault and J. L. Pezzaniti, "Polarization imaging through scattering media," *Proc. SPIE*, vol. 4133, pp. 124–133, Nov. 2000.

[44] N. Ghosh and I. A. Vitkin, "Tissue polarimetry: concepts, challenges, applications, and outlook.," *J. Biomed. Opt.*, vol. 16, p. 110801, Nov. 2011.

[45] S. G. Demos and R. R. Alfano, "Optical polarization imaging," *Appl. Opt.*, vol. 36, p. 150, Jan. 1997.

[46] S. Demos, H. Radousky, and R. Alfano, "Deep subsurface imaging in tissues using spectral and polarization filtering," *Opt. Express*, vol. 7, p. 23, July 2000.

[47] V. Sankaran, J. T. Walsh, and D. J. Maitland, "Comparative study of polarized light propagation in biologic tissues.," *J. Biomed. Opt.*, vol. 7, pp. 300–6, July 2002.

[48] S. L. Jacques, J. C. Ramella-Roman, and K. Lee, "Imaging skin pathology with polarized light.," *J. Biomed. Opt.*, vol. 7, pp. 329–40, July 2002.

[49] J. C. Ramella-Roman, K. Lee, S. A. Prahl, and S. L. Jacques, "Design, testing, and clinical studies of a handheld polarized light camera.," *J. Biomed. Opt.*, vol. 9, pp. 1305–10, Jan. 2004.

[50] H. Shao, Y. He, W. Li, and H. Ma, "Polarization-degree imaging contrast in turbid media: a quantitative study.," *Appl. Opt.*, vol. 45, pp. 4491–6, June 2006.

[51] Z. Nan, J. Xiaoyu, G. Qiang, H. Yonghong, and M. Hui, "Linear polarization difference imaging and its potential applications.," *Appl. Opt.*, vol. 48, pp. 6734–9, Dec. 2009.

[52] A. Da Silva, C. Deumié, and I. Vanzetta, "Elliptically polarized light for depth resolved optical imaging.," *Biomed. Opt. Express*, vol. 3, pp. 2907–15, Nov. 2012.

[53] D. Deirmendjian, "Scattering and polarization properties of water clouds and hazes in the visible and infrared," *Appl. Opt.*, vol. 3, no. 2, p. 187, 1964.

[54] J. S. Ryan and a. I. Carswell, "Laser beam broadening and depolarization in dense fogs," *J. Opt. Soc. Am.*, vol. 68, p. 900, July 1978.

[55] R. Cheung and A. Ishimaru, "Transmission, backscattering, and depolarization of waves in randomly distributed spherical particles," *Appl. Opt.*, vol. 21, no. 20, pp. 3792–8, 1982.

[56] S. Jaruwatanadilok, A. Ishimaru, and Y. Kuga, "Imaging techniques through discrete scattering media by polarized pulse waves," *Proc. SPIE*, vol. 4819, no. 206, p. 87, 2002.

[57] S. Jaruwatanadilok and A. Ishimaru, "Optical imaging through clouds and fog," *Geosci. Remote Sensing, IEEE Trans.*, vol. 41, no. 8, pp. 1834–1843, 2003.

[58] D. Miller and E. L. Dereniak, "Selective polarization imager for contrast enhancements in remote scattering media.," *Appl. Opt.*, vol. 51, pp. 4092–102, June 2012.

[59] J. Fade, S. Panigrahi, A. Carré, L. Frein, C. Hamel, F. Bretenaker, H. Ramachandran, and M. Alouini, "Long-range polarimetric imaging through fog.," *Appl. Opt.*, vol. 53, pp. 3854–65, June 2014.

[60] J. S. Tyo, D. L. Goldstein, D. B. Chenault, and J. A. Shaw, "Review of passive imaging polarimetry for remote sensing applications.," *Appl. Opt.*, vol. 45, pp. 5453–69, Aug. 2006.

[61] F. MacKintosh, J. Zhu, D. Pine, and D. Weitz, "Polarization memory of multiply scattered light," *Phys. Rev. B*, vol. 40, no. 13, pp. 9342–9345, 1989.

[62] M. Xu and R. Alfano, "Circular polarization memory of light," *Phys. Rev. E*, vol. 72, p. 065601, Dec. 2005.

[63] C. M. Macdonald, S. L. Jacques, and I. V. Meglinski, "Circular polarization memory in polydisperse scattering media," *Phys. Rev. E*, vol. 91, p. 33204, Mar. 2015.

[64] T. Young, "An Account of Some Cases of the Production of Colours, not Hitherto Described," *Philos. Trans. R. Soc. London*, vol. 92, pp. 387–397, Jan. 1802.

[65] E. L. Malus, "Mem. presentes a l'Inst. par divers Savans, ii," tech. rep., 1811.

[66] D. F. J. Arago and A. J. Fresnel, "On the action of rays of polarized light upon each other," *Ann. Chim. Phys.*, vol. 3, p. 288, 1819.

[67] D. F. J. Arago *Ann. Chim. Phys.*, vol. 1, p. 89, 1824.

[68] R. A. Millikan, "A Study of the Polarization of the Light emitted by Incandescent Solid and Liquid Surfaces," *Phys. Rev. (Series I)*, vol. 3, pp. 81–99, Sept. 1895.

[69] D. Goldstein, *Polarized Light, Revised and Expanded*. CRC Press, 2003.

[70] R. C. Jones, "A New Calculus for the Treatment of Optical Systems," *J. Opt. Soc. Am.*, vol. 31, p. 488, July 1941.

[71] H. Hurwitz Jr. and R. C. Jones, "A New Calculus for the Treatment of Optical Systems," *J. Opt. Soc. Am.*, vol. 31, p. 493, July 1941.

[72] R. C. Jones, "A New Calculus for the Treatment of Optical Systems," *J. Opt. Soc. Am.*, vol. 31, p. 500, July 1941.

[73] G. G. Stokes *Trans. Camb. Phil. Soc.*, vol. 1, no. 9, p. 399, 1852.

[74] W. A. Shurcliff, *Polarized Light*. Cambridge, MA: Harvard University Press, 1962.

[75] M. Born and E. Wolf, *Principles of Optics*. New York, New York, USA: Pergamon Press, 4th ed., 1970.

[76] R. A. Chipman, "Polarized Light and Polarimetry," in *Univ. Arizona Course Notes*, 2013.

[77] A. Ishimaru, *Wave Propagation and Scattering in Random Media: Single scattering and transport theory*. Academic Press, 1978.

[78] G. Mie, "Beiträge zur Optik trüber Medien, speziell kolloidaler Metallösungen," *Ann. Phys.*, vol. 330, no. 3, pp. 377–445, 1908.

[79] C. Bohren and D. Huffman, *Absorption and scattering of light by small particles*. New York, New York, USA: John Wiley & Sons, Inc., 1983.

[80] H. C. van de Hulst, *Light Scattering by Small Particles*. Courier Dover Publications, 1957.

[81] N. Metropolis and S. Ulam, "The Monte Carlo Method," *J. Am. Stat. Assoc.*, vol. 44, no. 247, pp. 335–341, 1949.

[82] J. C. Ramella-Roman, S. A. Prahl, and S. L. Jacques, "Three Monte Carlo programs of polarized light transport into scattering media: part I.," *Opt. Express*, vol. 13, pp. 10392–405, Dec. 2005.

[83] S. Chandrasekhar, *Radiative Transfer*. Dover Publications, 1960.

[84] M. Kerker, *The scattering of light, and other electromagnetic radiation*. Academic Press, 1969.

[85] A. N. Witt, "Multiple Scattering in reflection Nebulae. I. A Monte Carlo Approach," *Astrophys. J. Suppl. Ser.*, vol. 35, pp. 1–6, 1977.

[86] J. W. Hovenier, "Symmetry Relationships for Scattering of Polarized Light in a Slab of Randomly Oriented Particles," *J. Atmos. Sci.*, vol. 26, pp. 488–499, May 1969.

[87] J. D. van der Laan, D. A. Scrymgeour, S. A. Kemme, and E. L. Dereniak, "Range and contrast imaging improvements using circularly polarized light in scattering environments," *Proc. SPIE*, vol. 8706, p. 87060R, 2013.

[88] J. D. van der Laan, D. A. Scrymgeour, S. A. Kemme, and E. L. Dereniak, "Detection range enhancement using circularly polarized light in scattering environments for infrared wavelengths," *Appl. Opt.*, vol. 54, pp. 2266–2274, Mar. 2015.

[89] K. Beier and H. Gemperlein, "Simulation of infrared detection range at fog conditions for Enhanced Vision Systems in civil aviation," *Aerosp. Sci. Technol.*, vol. 8, pp. 63–71, Jan. 2004.

[90] M. Al Naboulsi, H. Sizun, and F. de Fornel, "Fog attenuation prediction for optical and infrared waves," *Opt. Eng.*, vol. 43, p. 319, Feb. 2004.

[91] D. L. Hutt, "Estimation of aerosol microphysical parameters from visible and infrared extinction measurements," *Proc. SPIE*, vol. 2828, pp. 503–514, 1996.

[92] D. Segelstein, *The complex refractive index of water*. M.s. thesis, University of Missouri, 1981.

[93] B. Weinzierl, A. Petzold, M. Esselborn, M. Wirth, K. Rasp, K. Kandler, L. Schütz, P. Koepke, and M. Fiebig, "Airborne measurements of dust layer properties, particle size distribution and mixing state of Saharan dust during SAMUM 2006," *Tellus B*, vol. 61, pp. 96–117, Feb. 2009.

[94] A. Ivanov, "Polarization of light and its use in various problems of optics of scattering media," *Opt. Spectrosc.*, vol. 107, pp. 171–183, Sept. 2009.

[95] F. E. Volz, "Infrared optical constants of ammonium sulfate, sahara dust, volcanic pumice, and flyash.," *Appl. Opt.*, vol. 12, pp. 564–8, Mar. 1973.

[96] L. S. Rothman, I. E. Gordon, Y. Babikov, A. Barbe, D. C. Benner, P. F. Bernath, M. Birk, L. Bizzocchi, V. Boudon, L. R. Brown, A. Campargue, K. Chance, E. A. Cohen, L. H. Coudert, V. M. Devi, B. J. Drouin, A. Fayt, J.-M. Flaud, R. R. Gamache, J. J. Harrison, J.-M. Hartmann, C. Hill, J. T. Hodges, D. Jacquemart, A. Jolly, J. Lamouroux, R. J. L. Roy, G. Li, D. A. Long, O. M. Lyulin, C. J. Mackie, S. T. Massie, S. Mikhailenko, H. S. P. Müller, O. V. Naumenko, A. V. Nikitin, J. Orphal, V. Perevalov, A. Perrin, E. R. Polovtseva, C. Richard, M. A. H. Smith, E. Starikova, K. Sung, S. Tashkun, J. Tennyson, G. C. Toon, V. Tyuterev, and G. Wagner, "The HITRAN2012 molecular spectroscopic database," *J. Quant. Spectrosc. Radiat. Transf.*, vol. 130, no. 0, pp. 4–50, 2013.

[97] J. D. van der Laan, D. A. Scrymgeour, S. A. Kemme, and E. L. Dereniak, "Increasing detection range and minimizing polarization mixing with circularly polarized light through scattering environments," *Proc. SPIE*, vol. 9099, p. 909908, 2014.

[98] C. Flueraru, S. Latoui, J. Besse, and P. Legendre, "Error Analysis of a Rotating Quarter-Wave Plate Stokes' Polarimeter," *Instrum. Meas. IEEE Trans.*, vol. 57, no. 4, pp. 731–735, 2008.

[99] R. A. Chipman, "Polarimetry," in *Handb. Opt.*, pp. Vol. 2, Chap. 22, 1995.

[100] I. Freund and M. Kaveh, "Comment on "Polarization memory of multiply scattered light"," *Phys. Rev. B*, vol. 45, pp. 8162–8164, Apr. 1992.

[101] N. Ghosh, P. K. Gupta, H. S. Patel, B. Jain, and B. N. Singh, "Depolarization of light in tissue phantoms effect of collection geometry," *Opt. Commun.*, vol. 222, no. 16, pp. 93–100, 2003.

[102] J. D. van der Laan, J. B. Wright, D. A. Scrymgeour, S. A. Kemme, and E. L. Dereniak, "Evolution of circular and linear polarization in scattering environments," *Opt. Express*, vol. Manuscript ID: 242453, p. In Review, 2015.

[103] J. D. van der Laan, D. A. Scrymgeour, J. B. Wright, S. A. Kemme, and E. L. Dereniak, "Increasing persistence through scattering environments by using circularly polarized light," *Proc. SPIE*, vol. 9465, p. 94650U, 2015.